VLBI Observations of Two Prototypical AGN:

The BL Lac Object S5 0716+714 and the FR II Radio Galaxy Cygnus A

Dissertation

zur

Erlangung des Doktorgrades (Dr. rer. nat.)

der

Mathematisch-Naturwissenschaftlichen Fakultät

der

Rheinischen Friedrich-Wilhelms-Universität Bonn

vorgelegt von

Uwe Bach

aus

Köln

Bonn, Juni 2004

Angefertigt mit Genehmigung der Mathematisch-Naturwissenschaftlichen
Fakultät der Rheinischen Friedrich-Wilhelms-Universität Bonn

1. Referent: Prof. Dr. Ulrich Klein
2. Referent: Priv. Doz. Dr. Walter Huchtmeier

Tag der Promotion:

CONTENTS

LIST OF FIGURES

III

LIST OF TABLES

Chapter 1

Introduction

The luminosity of most of the known galaxies is dominated by their stellar emission, but there exist some galaxies where a significant fraction of the energy output has a non-thermal origin. These are called active galaxies or active galactic nuclei (AGN), if the non-thermal emission originates mainly from the core. Although AGN represent only a small fraction of all galaxies they have been studied intensively over the last 40 years at all accessible wavelengths. This is partly because their high luminosities made them the only objects that could be studied at cosmologically important distances for a long time. Their extreme properties caused controversy about their nature. At radio wavelength some active galaxies are the most luminous sources in the sky and were the first sources detected in the early stages of radio astronomy (e.g., Baade & Minkowski 1954). At some level, all galaxies appear to be sources of radio emission. Normal spiral galaxies such as our own Galactic system have only very low radio luminosities. Some Seyfert galaxies, starburst galaxies, and elliptical galaxies are 100 to 1000 times more luminous. However, some of the galaxies and quasars are powerful radio sources with high radio luminosities.

For the more powerful sources, the radio emission often comes from regions of several hundreds of kiloparsecs away from the associated optical object and these regions are called radio lobes. In other cases, however, particularly in AGN, much of the radio emission comes from a very small region, when compared to normal galaxies, with dimensions of only a few parsecs. Based on the last decades of detailed observations of active galaxies it is believed that the high luminosities of AGN are due to accretion on to a supermassive black hole (e.g., Begelman et al. 1984). In this picture the radio emission of the compact sources originates from jets connecting the compact central region with the extended radio lobes. The jet emission is due to synchrotron radiation of relativistic electrons moving in a magnetic field along the jet.

Since single-dish radio telescopes have a low resolution, much of the early research was based on radio spectra and variability studies (e.g., Kellermann & Pauliny-Toth 1968, 1969). Only with the development of radio interferometers

in the early 1960's (Ryle & Hewish 1960) and in particular the development of Very Long Baseline Interferometry (VLBI) made it possible to image the inner regions of AGN. The direct imaging of parsec-scale jets and the complementary study of activity in the associated AGN in all spectral regimes has broadly enhanced our understanding of these objects. In particular, they have inspired and constrained the development of realistic physical models, helped to establish the relativistic jet paradigm, and influenced the thinking about general AGN unification.

This work intends to summarize the recent results of multi-epoch and multi-frequency VLBI observations of the blazar S5 0716+714 and the radio galaxy Cygnus A. I will discuss their implication for our knowledge of the formation and evolution of parsec-scale jets and their placement in terms of the unified scheme of AGN. In this work I use the cosmological parameters measured by the Wilkinson Microwave Anisotropy Probe (WMAP) of $H_0 = 71 \, \mathrm{km \, s^{-1} \, Mpc^{-1}}$, a pressureless matter content of $\Omega_\mathrm{m} = 0.3$ and a cosmological constant of $\Omega_\lambda = 0.7$ (Bennett et al. 2003). I use the equation given in Pen (1999) to compute the luminosity distance for a flat cosmology with a cosmological constant. When results from other papers are quoted, these results have been converted to the set of cosmological parameters given above. Table 1.1 shows a list of often used abbreviations.

Table 1.1: List of often used abbreviations.

Abb.	Meaning
AGN	active galactic nuclei
BLR	broad line region
FR	Fanaroff & Riley
IDV	intraday variability
ISM	interstellar medium
ISS	interstellar scattering
NLR	narrow line region
RISS	refractive interstellar scattering
SED	spectral energy distribution

In the first chapter, the different types and models of active galaxies, the observational phenomena that come along with relativistic jets, and the properties that can be derived from variability studies will be explained. In the second chapter, a short description of VLBI and the reduction of VLBI data will be given. In the third chapter I will introduce the two sources that we intensively studied in the last years and show their importance. In the fourth chapter a study of the annual evolution of the VLBI structure and the flux density of 0716+714 will be presented. In the fifth chapter, I will discuss the short term, day to day, variability and the linear polarization properties of 0716+714. In the sixth chapter, the analysis and discussion of the VLBI observations of Cygnus A are presented and in the seventh chapter a final summary will be given.

1.1   Active Galactic Nuclei

An early advance in AGN research was the redshift measurement of the first quasi-stellar object (quasar), 3C 273, which turned up as a result of optical identification for the early radio surveys (Schmidt 1963). These are the most powerful astronomical sources of radiation known, and sensitive high-resolution optical imaging is now capable of proving that a quasar is in fact a galaxy being out-shone by an active nucleus. In the last decades a variety of species of AGN was found and were divided in several "classes" of AGN. In the following the observational characteristics of these classes will be given.

Seyfert Galaxies   named after their discoverer (1943), Carl Seyfert, are gas and dust rich spiral galaxies with bright optical cores. As AGN in general they are divided in two types: Galaxies of type 1 (Seyfert 1) have broad emission lines; galaxies of type 2 (Seyfert 2) show only narrow emission lines. In some Seyfert 2 galaxies broad emission lines could be detected in polarized emission, which led to the idea that the different types might be due their orientation to the observer (Antonucci & Miller 1985). If all Seyferts exhibit a broad line region (BLR) in the centre, but this is surrounded by an asymmetric absorber, then it depends on the orientation whether we can see the BLR or not (see also Section 1.1.1). Usually Seyferts are only weak radio emitters.

Radio Galaxies   are elliptical galaxies that show a double-sided radio structure, the so called radio lobes, around the central optical galaxy. The radio lobes form some of the largest known structures in the universe, and often extend hundreds of kiloparsec or even megaparsec. They are fed by jets that originate from the central AGN. High-resolution VLBI images generally show a very compact component in the middle that is coincident with the AGN, and only the approaching jet. On these scales, the receding counter-jet is mainly weak due to relativistic beaming (see Section 1.2). Fanaroff & Riley (1974) divided radio galaxies by their morphology: objects with well-collimated jets forming huge radio lobes with hot-spots, which are very luminous spots at the end of the jet, are called FR II; objects showing a slowly fading jet that is often distorted and/or widened further out are called FR I radio galaxies. The two classes can also be divided at an absolute luminosity of $P(1.4\,\mathrm{GHz}) \sim 10^{25}\,\mathrm{W\,Hz^{-1}}$. Sources weaker than these level appear as FR I while the brighter sources are FR II, however, the luminosity boundary between them is not very sharp. In addition, radio galaxies are again divided into objects showing narrow and broad emission lines, which is also most likely due to orientation effects.

Quasars   are the most distant and powerful AGN and most of them have broad emission lines. The radio structure is often similar to FR II radio galaxies, but quasar cores and jets are much more luminous and the ratio of core and jet luminosity to the lobe luminosity is higher compared to radio galaxies. There are radio quiet and radio loud quasars and it was a popular idea that radio loud quasars lie in bright elliptical galaxies while the radio quiet quasars, like

Seyfert nuclei, lie in spiral galaxies. High-resolution HST images showed that quasars exist in nearly all types of galaxies (Bahcall et al. 1997) and the authors concluded from this that it is not the obvious shape of the galaxy that determines the characteristics of the quasar.

Blazars represent a small number of AGN that are extremely variable and have very unusual spectral characteristics. It seems that they have in common a small angle to the line of sight (probably near 0 degrees). This class includes the BL Lacertae (BL Lac) objects, which are radio-loud AGN that lack strong emission or absorption features, and flat-spectrum radio quasars that show rapid variability and/or a high degrees of polarization. Their radio structures are mostly dominated by a compact radio core component.

A nice image collection of the different morphologies of radio galaxies and quasar can be viewed at `http://www.cv.nrao.edu/~abridle/images.htm`. The types described above are the most common classes and many of them are again divided into subclasses based on their empirical radio, optical and X-ray properties. In general, it has proven to be more physical useful to divide AGN into type 1 and type 2, based on the presents or absence of broad emission lines, or type 0 (for $0°$ inclination), which show no emission lines at all, and into radio quiet and radio loud objects[1]. Thus, the different classifications all arise more or less the same phenomenon, depending on the orientation, amount of obscuration, and efficiency and physics at the central engine. which type of AGN we observe. In the following section we will present the current status of the attempts to unify the "AGN zoo".

1.1.1   Unified Scheme

The summary presented here is mainly based on the detailed reviews about the history and present status of the unification given by Antonucci (1993), Urry & Padovani (1995) and Urry (2004). Based on nearly 20 years of detailed investigations of active galaxies, a unification paradigm has emerged in which active galactic nuclei share certain fundamental ingredients (illustrated in Fig. 1.1):

- a supermassive black hole, $10^{6-10} M_\odot$

- an accretion disk and corona, heated by magnetic and/or viscous processes so that it radiates at optical through soft X-ray energies,

- high velocity gas, usually referred to as the broad-line region,

- lower velocity gas in the narrow line region,

- an obscuring torus (or other geometrical form) of gas and dust, hiding the broad-line region in some directions,

---

[1]Radio-loud AGN are those with a high ratio of radio to optical emission, usually defined as $\log F_{5\,\mathrm{GHz}}/F_{500\,\mathrm{nm}}$

- and a relativistic jet, formed within < 100 Schwarzschild radii of the black hole, and extending outward for tens of kpc, and, in some cases, as far as Mpc.
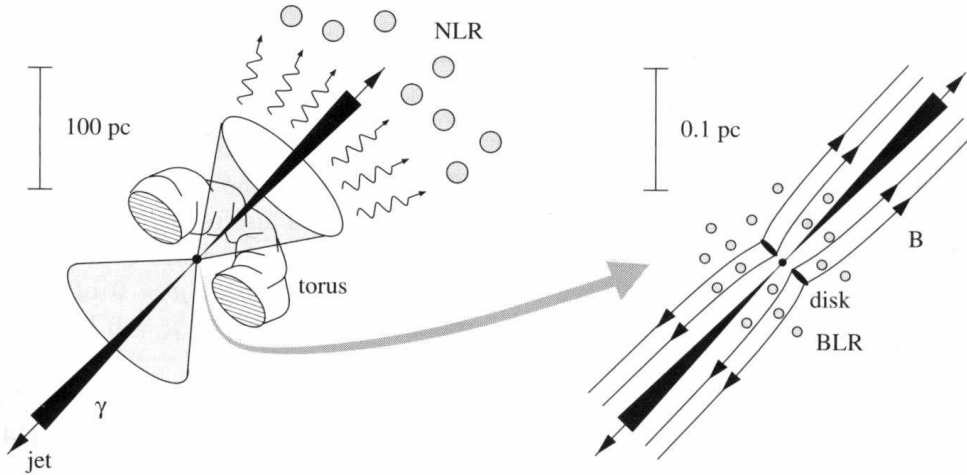
Figure 1.1: Schematic illustration of the unified scheme, see text for details (reproduced from Peacock (1999)).

The first four items are widely accepted, and it remains to see how large the intrinsic differences in the black hole mass, accretion rate, and black hole spin are, and how the BLR and NLR are structured. Less certain is the nature of the obscuring absorber and whether its appearance depends on the evolutionary stage and/or luminosity of the AGN. Local obscuration has been well studied, starting with spectropolarimetric observations by Antonucci & Miller (1985), which suggested that obscuration blocks our view of the broad line region for large viewing angles, and therefore that the viewing angle determines whether we observe type 1 or type 2 AGN. The local fraction of type2 to type 1 AGN is about 4:1. Curiously, only a few type 2 AGN have been found at redshifts higher than about 3 (e.g., Stern et al. 2002), and it seems that at these epochs much more type 1 AGN exist. In the near future deep surveys like GOODS[2], SWIRE[3] and others will help to answer if obscured AGN exist everywhere or if they are a "local" phenomena.

Relativistic jets seem to be present in all radio-loud AGN, though with a range of kinetic powers. It is not known why only 10 % of the AGN are radio-loud, but the formation of powerful jets might be related to the near black hole environment, the magnetic field strength, or the black hole spin (e.g., Blandford et al. 1990; Wilson & Colbert 1995). Beside the orientation effect determining the optical appearance of type 1 and type 2 AGN, there is also an orientation effect in the radio appearance of radio-loud AGN. The viewing angle determines whether an AGN appears as a core-dominated flat-spectrum object or a lobe-

---

[2]The Great Observatories Origins Deep Survey http://www.stsci.edu/science/goods/
[3]The SIRTF Wide-area InfraRed Extragalactic Survey http://www.ipac.caltech.edu/SWIRE/

dominated steep-spectrum object. Although the symmetry axis is the same, the viewing angle dependences are different. The first is dominated by optical depth effects and by the structure of the obscuring material and the second by the beaming pattern that depends on the Doppler factor (see next Section). The effects of relativistic beaming are well understood and Lorentz factors of about 10 explain well the relative number of steep-spectrum and flat-spectrum AGN, and also fit the observed superluminal motions in most cases.

This simple model already describes many of the observed properties, like the division of FR I and BL Lacs and FR II and quasars, which means that we have some insights into the nature of AGN. However, there are still a number of problems. The models become quite complicated especially when considering cosmic evolution. The increasing number of large complete samples will help refine the models.

1.2 Relativistic Jets

The regions of an AGN that are observable with VLBI are dominated by the relativistic jets and therefore some of the phenomena related to relativistic sources will be described. These phenomena include synchrotron radiation, apparent superluminal motion, relativistic beaming, and Doppler boosting.

1.2.1 Synchrotron Radiation

Synchrotron radiation is electro magnetic radiation that was first observed in particle accelerators called synchrotrons. It occurs when a charged particle is accelerated in a magnetic field. Synchrotron radiation is alway linearly polarized and this presented the main evidence for the radio emission of AGN to be synchrotron radiation (Ginzburg & Syrovatskii (1965) and ref. therein). Since an electron is 2000 times lighter than a proton, and therefore can more easily reach relativistic velocities, the dominant part of the observed synchrotron emission comes from electrons.

As the energetic electrons encounter a magnetic field, they gyrate around it. Since the helical motion continuously changes the direction of motion of the electron, the electron is accelerated and emits synchrotron radiation (Figure 1.2). The frequency of the emission is directly related to how fast the electron is travelling. This can be related to the initial velocity of the electron, or it can be due to the strength of the magnetic field, B. A stronger field creates a tighter spiral and therefore greater acceleration. Hence, it is:

$$\nu = \Gamma^2 \, \frac{Be}{2\pi m_{\mathrm{e}}} \qquad\qquad (1.1)$$

where e is the electron charge, m_{e} is the electron mass, and $\Gamma = \frac{1}{\sqrt{1-\beta_{\mathrm{e}}^2}}$ the Lorentz factor of the electron with speed $\beta_{\mathrm{e}}\, c$. For an observer at rest, the emission of a relativistic electron is no longer that of a dipole, but is beamed into a cone with opening angle $1/\gamma$.
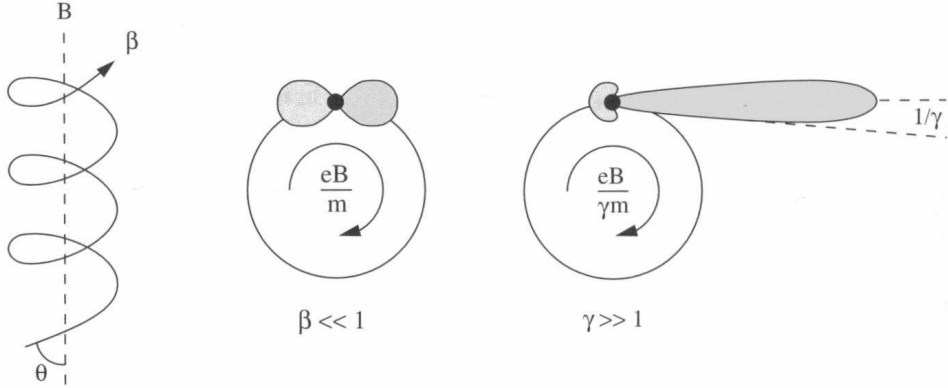
Figure 1.2: Sketch of an electron moving in a magnetic field (reproduced from Peacock (1999)).

The energy distribution $N(E)dE$ of an ensemble of electrons is described by a power law:

$$N(E)dE \propto E^{-s}dE, \tag{1.2}$$

where s corresponds to the spectral index of the electron energy. This results in a continuous synchrotron spectrum of:

$$I(\nu) \propto \nu^{\alpha}, \tag{1.3}$$

with $\alpha = \frac{1-s}{2}$ being the spectral index of the synchrotron emission. Therefore, we can infer the spectral index of the electrons by measuring the index of the synchrotron spectrum and vice versa.

Measurements of the comic background radiation suggest an electron spectral index of about 2.5. This value is consistent with the optically thin synchrotron emission ($\alpha = -0.7$) from our Galaxy, supernovae remnants and the extended structures in radio galaxies. However, at lower frequencies and hence lower energies the electrons start to self absorb the emitted photons via the inverse Compton process and the photon spectral index changes from -0.7 to $\alpha = 2.5$. The corresponding turn-over frequency, ν_{n}, is (Kellermann & Pauliny-Toth 1969):

$$\nu_{\mathrm{n}} = \frac{c}{\Omega}\sqrt{\frac{2S_{\mathrm{n}}}{kT_{\mathrm{b}}\pi(1-z)}}, \tag{1.4}$$

where Ω is the solid angle of the source, T_{b} the brightness temperature in K, k the Boltzmann constant, S_{n} the flux density at the turn-over frequency in $\mathrm{W\,m^{-2}\,Hz{-}1}$, ν_{n}, and z is the redshift. Knowing the size and the spectrum of a source this enables to calculate the strength of the magnetic field:

$$B = 10^{-5}b(\alpha)\frac{\Theta^{4}\nu^{5}\delta}{S_{\nu}^{2}(1+z)} \text{ gauss.} \tag{1.5}$$

Here, δ is the Doppler factor, $b(\alpha)$ is a tabulated value of the spectral index with a typical value for optically thin emission of 3 (Marscher 1983), Θ is the size of the emitting region in mas, ν is the turn-over frequency in GHz, and S_ν is the source flux density in Jy.

1.2.2 Superluminal Motion
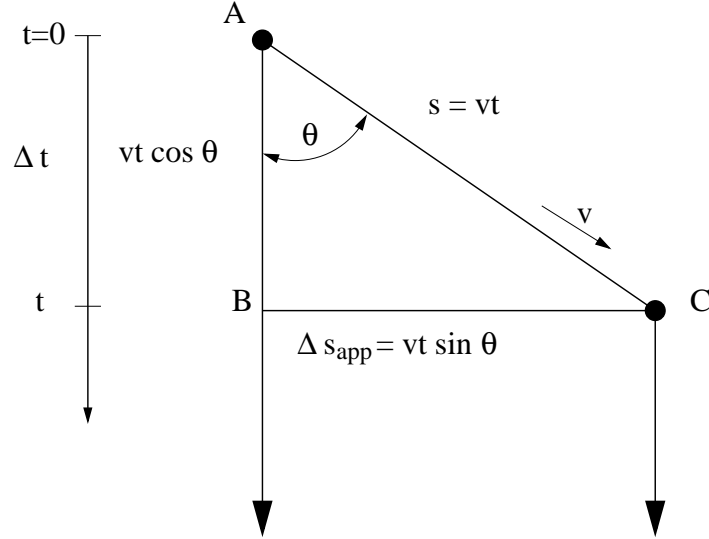
Figure 1.3: Illustration of the geometric arrangement responsible for the apparent superluminal motion. Assuming a jet component that is moving at an intrinsic velocity v in the time interval t from point A to C, an observer from the direction of the arrows will measure its apparent separation from B to C of $\Delta s_{\mathrm{app}} = vt \sin\theta$ in his apparent time interval $\Delta t_{\mathrm{app}} = \Delta t - \beta t \cos\theta$. The result of ds/dt is Equation 1.6.

To explain the high brightness temperatures inferred from variability studies of AGN Rees (1967), theoretically predicted the superluminal motion ten years before the first observational evidence (e.g., Cohen et al. 1977). Since then many superluminal jets were found (e.g., Kellermann et al. 2004; Vermeulen & Cohen 1994; Zensus 1997) Superluminal motion is an apparent effect that appears when relativistic motion is observed under small viewing angles. The observed transverse velocity of an emitting blob, $v_{\mathrm{app}} = \beta_{\mathrm{app}}\, c$, is related to its true velocity, $v = \beta\, c$, and the angle to the line of sight by

$$\beta_{\mathrm{app}} = \frac{\beta \sin\theta}{1 - \beta \cos\theta}, \qquad (1.6)$$

as illustrated in Figure 1.3. It can be shown that if $\beta > 1/\sqrt{2} = 0.7$, for some orientations, then superluminal motion is observed. The maximum value of the apparent velocity, $\beta_{\mathrm{app,max}} = \sqrt{\gamma^2 - 1}$, occurs when $\cos\theta = \beta$ or $\sin\theta = \gamma^{-1}$; for this angle, $\delta = \gamma$. This implies a minimum value for the Lorentz factor $\gamma_{\mathrm{min}} = \sqrt{\beta_{\mathrm{app}}^2 + 1}$ (see Figure 1.4). For example, if one detects superluminal motion in a source with $\beta_{\mathrm{app}} \sim 5$, the Lorentz factor must be at least 5.1. It is also apparent from Figure 1.4 that superluminal speeds are possible even for

large angles to the line of sight; sources oriented at $\theta \sim 50\,°$, have $\beta_{\mathrm{app}} \geq 2$ if $\gamma \geq 5$, and sources in the plane of the sky ($\theta = 90\,°$) have $\beta_{\mathrm{app}} \sim 1$ for $\gamma \geq 3$.
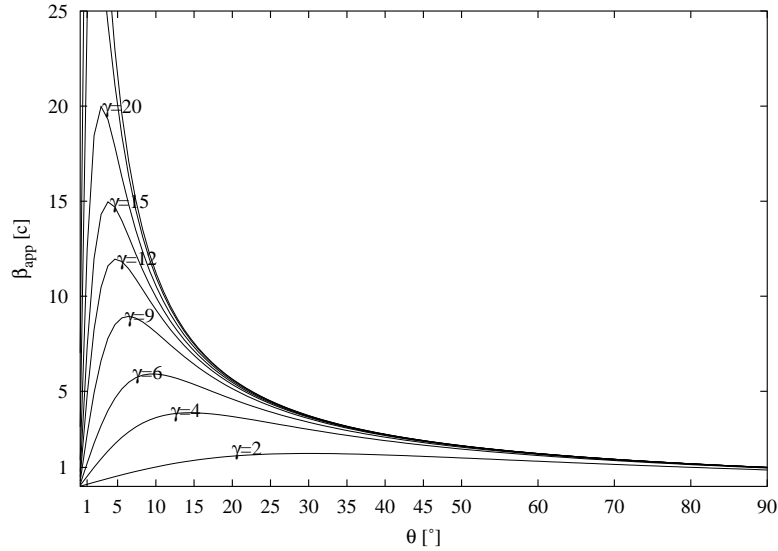
Figure 1.4: The graph illustrates the relation between the apparent velocity against the viewing angle from Equation 1.6.

1.2.3 Relativistic Beaming and Doppler Boosting

For an approaching source, time intervals measured in the observer frame are shorter than in the rest frame, because the emitter "catches up" with its own photons. This leads to an amplification (relativistic beaming) of the the flux density, S, as

$$S = S_0 \delta^{(3-\alpha)}, \tag{1.7}$$

where the α in the index corrects for the Doppler effect, which causes a frequency shift in the spectrum by the Doppler factor, δ. For a continuous jet the exponent changes to $(2 - \alpha)$ due to geometrical considerations (Scheuer & Readhead 1979). From this one can calculate the flux density ratio between the approaching jet and the receding counter-jet as

$$\frac{S_{\mathrm{j}}}{S_{\mathrm{cj}}} = R = \left(\frac{1 + \beta \cos\theta}{1 - \beta \cos\theta} \right)^{(2-\alpha)}. \tag{1.8}$$

For moderate values of $\beta = 0.95$, $\theta = 10°$, and $\alpha = 0.7$ the resulting jet to counter-jet ratio is 10^4. From this, it is obvious why most of the observed sources show only a one sided jet.

1.2.4 Brightness Temperature

The flux density emitted from a black body only depends on its temperature and size and the observed frequency. Hence, if one observes for a source a

certain flux density and size one can calculate a "virtual" temperature of the source which a black body would need to have in order to produce the observed flux density. This "virtual" temperature is called "Brightness Temperature" and for a Gaussian modelfit component T_b is

$$T_b = \frac{I\lambda^2}{2k} = \frac{S\lambda^2}{2\Omega_b k} = 1.22 \cdot 10^{12} \frac{S}{\theta_F^2 \nu^2}, \qquad (1.9)$$

where S (in Jy) is the flux density θ (in mas) the full width half maximum (FWHM), and ν (in GHz) the observing frequency

Brightness temperatures that significantly exceed 10^{10} K are definitively produced by non-thermal processes since $k_B T > m_e c^2$. The brightness temperature has a very strong upper-limit for non-thermal, synchrotron radiation – the Compton limit. One can show (Kellermann & Pauliny-Toth 1969; Rybicki & Lightman 1979, chap. 7.2) that the radiation from synchrotron emission, P_{syn}, and from inverse-Compton scattering, P_{compt}, is

$$\frac{P_{syn}}{P_{compt}} = \frac{U_B}{U_{ph}}. \qquad (1.10)$$

Where U_{ph} is the photon energy density and U_B the magnetic field energy density. Increasing the brightness temperature of a source means also increasing the photon energy density (more flux density in the same volume). When $U_{ph} > U_B$ the relativistic electrons will scatter their own synchrotron-photons, thus increasing the photon energy density further. This is a run-away process, called the Compton catastrophe. The process will very quickly cool the plasma to a situation where $U_{ph} \leq U_B$ and hence will also limit the maximum brightness temperature of a system to

$$T_b < 10^{12} \text{ K}. \qquad (1.11)$$

Readhead (1994) found an even lower limit to the brightness temperature from equipartition arguments. The author states that if there is no large departure between minimum energy and equipartition, then the limiting brightness temperature is 5×10^{10} K to 10^{11} K. Recent space-VLBI observations (see Chapter 5 for details on VSOP), however, have shown that in some blazar cores $T_b > 10^{12}$ K (Tingay et al. 2001). This was actually expected since relativistic boosting will increase the flux density without changing the size of the jet, hence it will lead to an apparent increase of T_b beyond the allowed value, proportional to the Doppler factor ($T_b' \propto T_b \cdot \delta$). Depending on the choice of the T_b-limit, Doppler factors of 3 to 30 are required to reduce the observed T_b' to the maximum intrinsic brightness temperature in 0133+476, the source with the highest brightness temperature of 1.8×10^{12} K (Tingay et al. 2001).

1.3 Variability in AGN

AGN have been found to be variable at all wavelengths at which they have been observed. The variations appear to be aperiodic and have variable amplitude.

As mentioned earlier, the variability in AGN at radio wavelengths has served as
a tool to investigate the emission processes in these objects since the discovery
of quasars (e.g., Kellermann & Pauliny-Toth 1968, 1969). Causality arguments
limit the radius of the emitting region to $r < c \cdot \Delta t$, with the light travel time Δt
corresponding to the time-scale of the variation. Observed time-scales of a day
or a few hours thus provide constraints on the source structure on linear scales
smaller than the solar system. A review on the broad-band variability in AGN
was recently given by Ulrich et al. (1997) and with the emphasis on intraday
variability (IDV) by Wagner & Witzel (1995). In this section I will concentrate
on the short term variability, since it will be more relevant in the context of
this thesis. As an example of an IDV light curve a three week spanning light
curve of 0716+714 is shown in Figure 1.5.
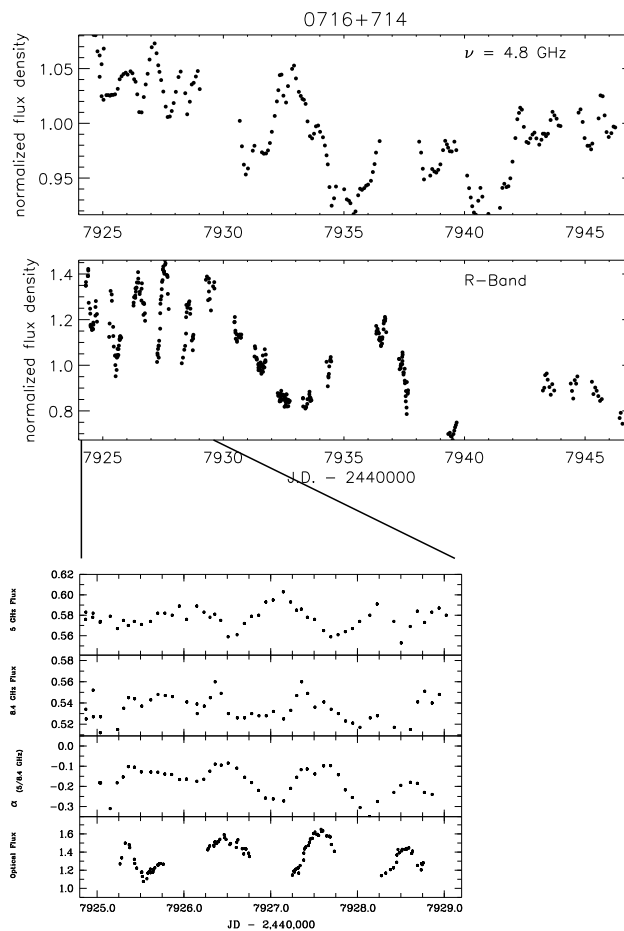
Figure 1.5: Top: An example of fast and slow IDV in 0716+714 at 5 GHz and optical R-
band (Quirrenbach et al. 1991). **Bottom:** Zoom into the time range of fast IDV showing the
correlation between the radio light curves, the radio spectral index and the optical R-band
light curve that suggests a partly intrinsic origin of the variability. (Qian et al. 1996; Wagner
et al. 1996).

To compare the variability measurements it is most common to use the
variability time-scales t, which weights the fluctuations by their amplitude and

is defined as $t = \frac{S}{\Delta S} \frac{\Delta t}{(1=z)}$ (e.g., Burbidge et al. 1974). Using the time-scale as a measure of the size of the source, the observed flux density can be converted into a photon density or a brightness temperature.

$$T_{\mathrm{b}} = 1.86 \times 10^4 \ S \ \left(\frac{d_{\mathrm{L}}}{\nu \ t \ (1+z)^2} \right)^2 \ \mathrm{K}, \qquad (1.12)$$

where S (in Jy) is the flux density, d_{L} (in Mpc) the luminosity distance, ν (in GHz) is the observing frequency, z is the redshift, and t (in yr) the variability time-scale. The rapid intra-day variability (IDV) in some sources implies apparent brightness temperatures, T_{b}', in the radio regime which exceed $10^{17}\,\mathrm{K}$. Such high brightness temperatures would be well above the Compton catastrophe limit $T_{\mathrm{b}} < 10^{12}\,\mathrm{K}$ (Kellermann & Pauliny-Toth 1969 and Section 1.2.4). Mechanisms that can reduce T_{b}' to intrinsic brightness temperature values lower than $10^{12}\,\mathrm{K}$ are relativistic beaming with extremely high Doppler factors ($T_{\mathrm{b}}' \propto T_{\mathrm{b}} \cdot \delta^3$), coherent radiation mechanisms, or special geometric effects (Wagner & Witzel 1995). Here, the apparent brightness temperature is proportional to δ^3 and not to δ as in Section 1.2.4, because we measure an equivalent source size which is affected by the Doppler boosting. For example, to reduce $T_{\mathrm{b}}' = 10^{17}\,\mathrm{K}$ to $T_{\mathrm{b}} = 10^{12}\,\mathrm{K}$ a Doppler factor of about 45 is needed. A lower limit of $5 \times 10^{10}\,\mathrm{K}$ to $10^{11}\,\mathrm{K}$ to the brightness temperature as it is derived from equipartition arguments (Readhead 1994) would result in even more extreme environments ($\delta \approx 100$ for $T_{\mathrm{b}}' = 10^{17}\,\mathrm{K}$).

However, also extrinsic causes for the IDV have to be considered. In this case the variability could be due to variable absorption along the line of sight as well as deflection of light. The deflection may either be due to a gravitationally distorted metric or to refractive or diffractive effects of the Galactic plasma along the line of sight. Motion of the source, the observer, or the deflecting medium can lead to temporal flux density variations registered by the observer. Variable absorption screens have been discussed by Marscher (1979), but those can not explain variability at high frequencies, especially at optical wavelengths.

Analysing the frequency dependence of the variability is one of the key experiments that can be done to distinguish between different variability effects. Whilst gravitational micro-lensing is achromatic, refractive interstellar scintillation (RISS) only affects observations at lower radio frequencies. The principles of interstellar scintillation have been reviewed recently by Rickett (1990, 2001b). Basically, RISS is not much different from the flickering of stars in our turbulent atmosphere. The radio emission of compact astronomical objects is expected to scatter through the turbulent interstellar plasma. The strength of the scattering thereby depends on the ratio of the angular size of the source and the angular size of the plasma cells in the scattering medium defined as the Fresnel scale:

$$\theta_{\mathrm{F}} = \sqrt{\frac{\lambda}{2\pi \ L}}, \qquad (1.13)$$

where λ is the observed wavelength, and L the distance to the scattering screen.

Although, in many cases the IDV can be now well modelled using ISS (Rick-

ett 2001b), there remain some sources like 0716+714 and 0954+658, where correlated variability between radio and optical wavelength were observed (Quirrenbach et al. 1991; Wagner et al. 1990), which suggests that at least part of the variability has an intrinsic origin. That sources showing intrinsic IDV vary partly due to ISS is almost certain, since the small source sizes derived from the variability and brightness temperature measurements are typically smaller than the Fresnel scale. We will try to further constrain the origin of IDV in blazars using a multi-epoch VSOP observation of 0716+714 that is presented in Chapter 5.

Chapter 2

Very Long Baseline Interferometry

The spatial resolution, δ, of a telescope depends on its diameter, D, and the observed wavelength, λ, $\delta \propto \lambda/D$. Therefore, radio telescopes, though sometimes incredibly large, have only moderate resolutions compared to optical telescopes. Thus, nearly simultaneous with the developments in single-dish radio astronomy astronomers started to investigate radio interferometry to increase the achievable resolution (Ryle & Hewish 1960). This technique is called "aperture synthesis" and was transferred from directly linked, locally distributed antennas to spatially widely separated radio telescopes in the 1970s. Very Long Baseline Interferometry (VLBI) is a combination of single-dish radio astronomy, interferometry and aperture synthesis, and therefore certainly one of the most advanced technical achievements of the 20th century. Consequently, in 1974, Sir Martin Ryle was awarded the Nobel prize in physics for his contribution.

Today VLBI has become a standard observing technique in radio astronomy and there exist several facilities, where astronomers can apply for observing time, e.g., the European VLBI Network (EVN), the US Very Long Base Line Array (VLBA), the Japanese VLBI Exploration of Radio Astrometry (VERA), and soon the Korean VLBI Network (KVN). Future projects like the Atacama Large Millimeter Array (ALMA), the Square Kilometer Array (SKA), and the Low Frequency Array (LOFAR), with much higher sensitivity will again increase the number of observable sources, specially at high redshifts.

The preparation and analysis of VLBI observations has become easier and now the first automated data calibration pipelines exist for the VLBA[1] and the EVN[2]. Since a good description of the VLBI principles and the data calibration steps required has recently been given by Klare (2003), and details can be found in, e.g., Thompson et al. (1986), I will not go into the details here, but would like to show the reader where the appropriate information can be found.

Special observing techniques like polarimetry and phase-referencing that are used in this thesis were also recently discussed by Middelberg (2004) and I

---

[1] http://www.aoc.nrao.edu/~lsjouwer/vlbapipe/
[2] http://www.evlbi.org/pipeline/user_expts.html

refer to his thesis about the technical details and the required data calibration steps. In the data reduction section I will mention that we performed the data reduction in the standard manner in NRAO's Astronomical Image Processing System AIPS. Here, I will briefly summarize the standard procedure:

- FITLD loads the data from tape in to AIPS and is used with the standard inputs.

- MSORT to sort the (u, v) data in time.

- UVCOP to split frequencies into separate files (only multi-frequency data)

- ACCOR corrects the amplitudes in the cross correlations, which might be wrong due to errors in the sampler threshold.

- INDXR creates a the index table (NX) and if necessary also the first calibration table (CL)

- if necessary: load pulse-calibration, gain, and T_{sys} calibration tables using PCLOD and ANTAB

- MERGCAL merges redundant calibration entries

- CLCOR (PANG) to remove the rotation of the parallactic angle.

- APCAL performs an amplitude calibration using provided T_{sys} and gain curve measurements. For higher frequencies it is recommended to include an opacity correction.

- PCCOR or FRING: PCCOR if pulse-calibration information is available. A manual phase calibration in FRINGE has to be done for every antenna without proper PC table entries.

- FRING to correct for the unknown atmospheric and ionospheric phase noise.

- CROSSPOL corrects the possible offsets between the IF's of the cross polarizations.

At this point the data are usually split (SPLIT) into separate files for each source and exported as (u, v)-FITS files (FITTP) for further imaging and phase and amplitude self-calibration in DIFMAP. Further information about VLBI data reduction in AIPS is available at `http://www.aoc.nrao.edu/aips/cook.html` and `http://www.aoc.nrao.edu/aips/aipsmemo.html` and a cookbook for DIFMAP can be found at `ftp://ftp.astro.caltech.edu/pub/difmap/difmap.html`.

Chapter 3

The Sources

We observed two radio sources that are the archetypes of their class of AGN: the BL Lac object 0716+714 and the FR II radio galaxy Cygnus A. Both are important test objects and they offer the opportunity to study the physics of jets from two different perspectives. A nearly face-on view is offered by the blazar 0716+714 and an edge-on view by Cygnus A. In the following chapter we will introduce these sources in detail.

3.1 0716+714

The S5 blazar 0716+714 is one of the most active BL Lac objects. It is extremely variable on time-scales from hours to months at all observed wavelengths from radio to X-rays. The redshift of 0716+714 is not yet known. However, optical imaging of the underlying galaxy provides a redshift estimate of $z \geq 0.3$ (Wagner et al. 1996). A recent X-ray study by Kadler et al. (2004) suggests a much lower redshift of 0.1, but this needs further confirmation and a redshift of 0.3 is used throughout this thesis. In the radio bands 0716+714 is an intraday variable (IDV) source (Witzel et al. 1986; Heeschen et al. 1987). It exhibits a flat radio spectrum at frequencies up to at least $350\,\mathrm{GHz}$. Quirrenbach et al. (1991) found strongly correlated IDV between radio and optical bands. Together with the correlated variations between X-ray and optical and the simultaneous variations between optical and radio, this strongly suggests an intrinsic origin for the intraday variability (Wagner & Witzel 1995; Wagner et al. 1996). From the observed IDV at cm-wavelengths a typical brightness temperature of $T_{\mathrm{b}} = 10^{15.5}\,\mathrm{K}$ to $10^{17}\,\mathrm{K}$ is derived (Kraus et al. 2003; Wagner et al. 1993). A Doppler factor of 15 to 50 would be needed to bring these brightness temperatures down to the inverse-Compton limit of $10^{12}\,\mathrm{K}$.

Very Long Baseline Interferometry (VLBI) studies spanning more than 20 years at cm-wavelengths show a core-dominated evolving jet extending several 10 milliarcseconds to the north (Eckart et al. 1986, 1987; Witzel et al. 1988). The VLBI jet is misaligned with respect to the VLA jet by $\sim 90°$ (e.g., Saikia

et al. 1987). In the literature the jet kinematics in 0716+714 are discussed
controversially. There exist several kinematic scenarios with motions ranging
from $0.05\,\mathrm{mas\,yr^{-1}}$ to $1.1\,\mathrm{mas\,yr^{-1}}$, corresponding to jet speeds of $0.9\,c$ to $21\,c$
at a redshift of 0.3 (Eckart et al. 1986, 1987; Gabuzda et al. 1998; Jorstad et al.
2001; Schalinski et al. 1992; Tian et al. 2001; Witzel et al. 1988). However,
some of these earlier kinematic models are based on infrequently sampled data.
Thus, it is at present not clear if 0716+714 is a superluminal source and and
how fast the motion in the VLBI jet is.

To investigate how fast the motion in the jets of blazars and especially
in IDV sources can be, a reanalysis of 10 years of VLBI data on 0716+714,
obtained at frequencies between $5\,\mathrm{GHz}$ and $22\,\mathrm{GHz}$ was done (Chapter 4). We
chose 0716+714, since the possible intrinsic origin of the IDV and the high
long-term activity, suggest higher than average speeds in the jet. To reveal the
origin of the short term variablity in 0716+714 a multi-epoch VSOP experiment
was performed in autumn 2000 and the results are presented in Chapter 5.
Figure 3.1 shows a collection of images of 0716+714 at different wavelengths
and scales.
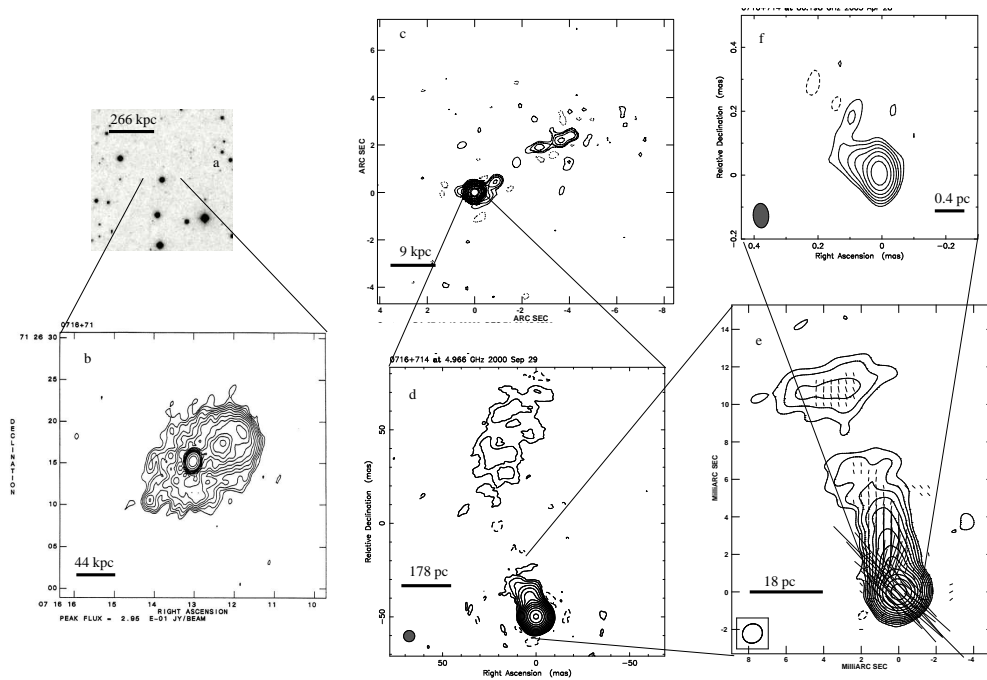
Figure 3.1: 0716+714 at several wavelengths showing the dramatical changes in the structure
between kpc-scales and pc-scales ($z = 0.3$). (a) Optical R-band image taken from the DSS
(http://arch-http.hq.eso.org/dss/dss). (b) $20\,\mathrm{cm}$ VLA image (Antonucci et al. 1986).
(c) $6\,\mathrm{cm}$ VLA image (Gabuzda et al. 2000a). (d) Strongly tapered ($6 \times 6\,\mathrm{mas^2}$ beam size)
VLBI image of the $6\,\mathrm{cm}$ ground array data presented in Section 5.2.1). (e) Same data using
uniform weighting ($1 \times 1\,\mathrm{mas^2}$ beam size) and with overlaid linear polarisation vectors. (f)
$3\,\mathrm{mm}$ global VLBI image; the highest resolution image of 0716+714 obtained so far (beam
size: $76 \times 49\,\mu\mathrm{as}$ at $3.5°$).

3.2   Cygnus A

Cygnus A is one of the first and strongest of the radio sources that were detected at the beginning of radio astronomy (Bolton & Stanley 1948). It turned out that Cygnus A belongs to a class of powerful extragalactic objects (Baade & Minkowski 1954), which were named radio galaxies and now belong to the group of active galaxies. With a redshift of 0.0561, it is the closest strong FR II radio galaxy and therefore a key object for detailed studies of AGN.

Its kiloparsec-scale structure in the radio bands is dominated by two huge radio lobes that are separated by about 2 arc-minutes and contain bright hot-spots. The radio core lies in the centre of an elliptical galaxy (Hargrave & Ryle 1974) and is connected by two thin jets to the radio lobes (e.g., Perley et al. 1984). VLBI images from 1.6 GHz to 43 GHz obtained during the last 20 years (Bach 2001; Bach et al. 2004, 2002; Carilli et al. 1994, 1991; Krichbaum et al. 1998, 1993) revealed a pronounced two-sided core-jet structure on parsec scales. An illustration of the appearance of Cygnus A at different scales is given in Figure 3.2. From the VLBI observations, increasing apparent jet speeds from $\beta_{\mathrm{app}} \approx 0.1$ to 0.2 (Krichbaum et al. 1998) near the core (1 mas) to $\beta_{\mathrm{app}} \approx 0.3$ to 0.7 at $r \geq 4$ mas (Bach 2001; Bach et al. 2002; Carilli et al. 1994) were measured. More recent observations at 5 GHz for the first time revealed significant structural variability on the counter-jet side, where we derive motion of $\beta_{\mathrm{app}} \approx 0.3 \pm 0.2$ at $r \approx 7$ mas (Bach et al. 2002).

Due to the large inclination of the jet with respect to the observer, and correspondingly reduced relativistic effects, Cygnus A is an ideal candidate for detailed studies of its internal jet physics, which are thought to be similar to those in the more luminous quasars (e.g. Barthel 1989). According to the unified scheme, narrow line radio galaxies, like Cygnus A, should contain an obscuring torus around the central engine that blocks the emission from the broad line region. To further constrain the velocity structure of the inner jet we studied the evolution of the parsec scale jet at 15 GHz over the last eight years and several multi-frequency observations between 5 GHz, 15 GHz, 22 GHz, 43 GHz and 86 GHz were made to probe the existence and structure of an circum-nuclear absorber (Chapter 6).
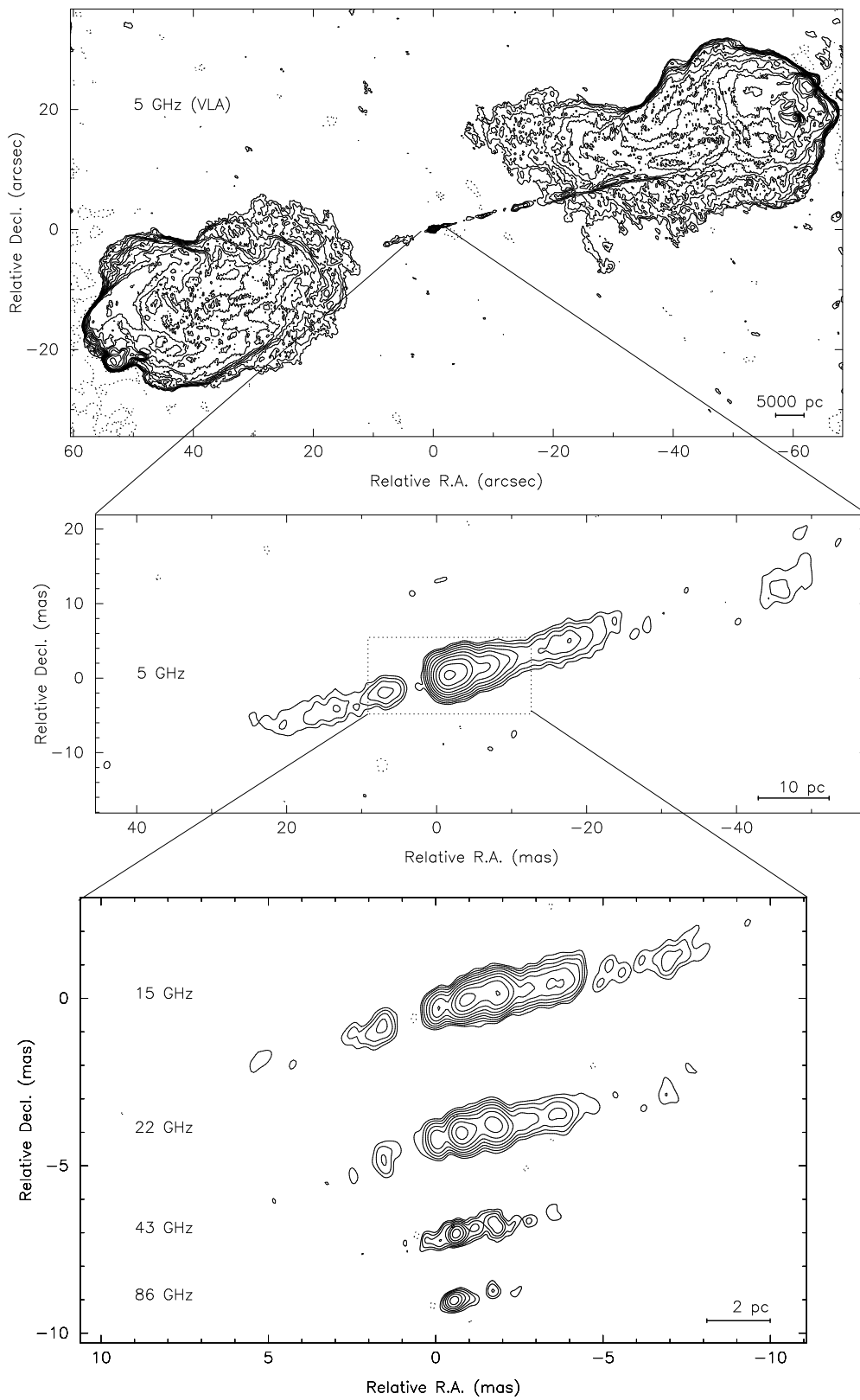
Figure 3.2: Images of Cygnus A at different scales. From top to bottom: a VLA image at 6 cm showing the whole radio source (Perley et al. 1984), VLBI image at 6 cm, and VLBI images at successively shorter wavelengths showing the core region with the jet and the counter-jet.

Chapter 4

Kinematic Study of the Blazar 0716+714

This chapter discusses the kinematic and geometric properties of the jet in 0716+714. VLBI studies over more than 20 years at cm-wavelengths show a core-dominated evolving jet extending several tens of milliarcseconds to the north. In the literature the jet kinematics in 0716+714 are discussed controversially. There exist several kinematic scenarios with motions ranging from $0.05\,\mathrm{mas\,yr^{-1}}$ to $1.1\,\mathrm{mas\,yr^{-1}}$. However, some of these earlier kinematic models are based on only two or three epochs separated by several years, which likely leads to ambiguities in the identification of fast components (Eckart et al. 1987; Gabuzda et al. 1998; Schalinski et al. 1992; Witzel et al. 1988). More recent studies based on more data measured higher jet speeds (Jorstad et al. 2001; Tian et al. 2001), but the results were still inconsistent between the two studies. Thus, it is at present not clear if 0716+714 is a superluminal source and and how fast the motion of the VLBI jet components is.

To test how fast the motion of the jet is a reanalysis of 10 years of VLBI data on 0716+714, obtained at $5\,\mathrm{GHz}$, $8\,\mathrm{GHz}$, $15\,\mathrm{GHz}$ and $22\,\mathrm{GHz}$ was made. The analysis includes 26 observing epochs, which are listed in Table 4.1.

In Section 4.1 a brief description of the observations, the data reduction and the model fitting process are given and the final maps are presented. The cross-identification of the individual jet components and a new kinematic model for the jet in 0716+714 are presented in Section 4.2. From this the jet speed and orientation are derived. We summarize our results in Section 4.3.

4.1 Observation and Data Analysis

All data were correlated in the standard manner using the MK III correlator in Bonn and the VLBA correlator in Socorro. Part of the post-correlation analysis was done using NRAO's Astronomical Image Processing System (Aips) and the Caltech VLBI Analysis Programs (Pearson & Readhead 1984). Data

Table 4.1: Observation log. Listed are the observing epoch, frequency ν, total flux density $S_{\mathrm{tot}}(\nu)$, beam size, beam position angle, peak flux density S_{peak} and the lowest contour at $3\,\sigma$ of the map in Figure 4.1 & 4.2.

Epoch	ν [GHz]	S_{tot} [Jy]	Beam [mas $\times$ mas]	P.A. [°]	S_{peak} $[\frac{Jy}{beam}]$	$3\,\sigma$ $[\frac{mJy}{beam}]$
1992.73 [a,(1)]	5.0	0.67	0.8 × 1.0	0	0.61	1.5
1992.85 [a]	22.2	0.75	0.9 × 2.7	−55	0.64	3.0
1993.71 [a]	22.2	0.40	0.2 × 0.2	35	0.31	2.0
1994.21	8.4	0.32	0.8 × 1.4	80	0.26	0.7
1994.21	22.2	0.34	0.3 × 0.5	79	0.30	1.8
1994.67 [(2)]	15.3	0.46	0.5 × 0.7	−29	0.40	1.8
1994.70 [a,(1)]	5.0	0.36	0.8 × 1.2	−15	0.29	2.7
1995.15 [(3)]	22.2	0.75	0.3 × 0.5	−3	0.71	4.0
1995.31 [(3)]	22.2	0.43	0.3 × 0.4	39	0.40	4.2
1995.47 [(3)]	22.2	0.20	0.3 × 0.6	7	0.18	3.0
1995.65	8.4	0.31	0.9 × 1.0	54	0.26	0.4
1995.65	22.2	0.34	0.3 × 0.4	−40	0.28	1.8
1996.34 [(3)]	22.2	0.27	0.3 × 0.9	48	0.22	3.2
1996.53 [(2)]	15.3	0.26	0.5 × 0.7	−15	0.22	0.7
1996.60 [(3)]	22.2	0.25	0.4 × 0.4	9	0.21	3.0
1996.63 [a,(1)]	5.0	0.22	1.4 × 2.2	41	0.18	1.3
1996.82 [(2)]	15.3	0.26	0.4 × 0.7	21	0.25	2.0
1996.90 [(3)]	22.2	0.29	0.4 × 0.5	−35	0.27	2.0
1997.03 [(4)]	8.4	0.21	1.1 × 1.4	7	0.18	0.0
1997.58 [(3)]	22.2	0.98	0.4 × 0.5	−33	0.90	4.0
1997.93 [(5)]	8.4	0.43	0.6 × 1.6	33	0.38	0.5
1999.41 [(5)]	8.4	1.02	0.5 × 1.5	−7	0.92	0.5
1999.55 [(2)]	15.3	1.25	0.5 × 0.8	4	1.14	1.2
1999.89 [a,(1)]	5.0	0.63	1.8 × 2.4	−60	0.54	0.7
2000.82 [b]	5.0	0.55	0.8 × 0.9	−28	0.48	0.1
2001.17 [(2)]	15.3	0.65	0.4 × 0.8	31	0.54	0.9

Note: The array used was the VLBA, unless indicated by a footnote. Epochs in bold face denote own data. a: Global array, b: VLBA+Eb
References: (1): Britzen et al. (1999) & in prep., (2): Kellermann et al. (1998) & Zensus et al. (2002), (3): Jorstad et al. (2001), (4): Fey & Charlot (2000), (5): Ros et al. (2001)

from other observers were provided as amplitude calibrated and fringe fitted
(u, v) fits files. The imaging of the source including phase and amplitude self-
calibration was done using the CLEAN (Högbom 1974) and SELFCAL pro-
cedures in DIFMAP (Shepherd 1994). The self-calibration was done in steps
of several phase-calibrations followed by careful amplitude calibration. During
the iteration process the solution interval of the amplitude self-calibration was
shortened from intervals as long as the whole observational time down to min-
utes. The resulting maps are presented in Figure 4.1 & 4.2. Here, the jet is
clearly visible to the north at P.A. $\sim 15°$, and is slightly bent. At the lower
frequencies we can follow the jet up to a distance of 15 mas (1 mas = 4.4 pc as-
suming a redshift of 0.3) from the core, whereas at the higher frequencies the
jet is visible up to 3 mas. In none of the VLBI maps is a counter-jet visible.

Epochs from surveys can be clearly separated from observations that were
dedicated to 0716+714 and therefore obtain have (u, v)-coverage. For example
most of the 8 GHz epochs in Figure 4.1 (excluding the centre panel (1997.03))
were not obtained in a survey and also the last 5 GHz epoch (2000.82) was
obtained in a 16 h observation with the VLBA and Effelsberg with 0716+714
as the primary target source. The 2000.82 5 GHz epoch is only one out of
three closely separated polarimetric VSOP observations that will be discussed
in Chapter 5.

4.1.1   Model Fits

After imaging in DIFMAP we fitted circular Gaussian components to the self-
calibrated data to parameterize the source structure seen in the VLBI maps.
We used only circular components to reduce the number of free parameters and
to simplify the analysis. During several iterations of model-fitting, we tried
to find models with a consistent number of components in adjacent epochs at
the same frequency. A summary of the Gaussian component parameters from
this model fitting is given in Table 4.2. For all model fits we used the bright-
est component as reference and fixed its position to (0,0). The positions of
the other components were measured relative to this component, which we as-
sumed to be stationary (see Sect. 4.2.1 for details). A maximum uncertainty of
15 % in the flux density was estimated from the uncertainties of the amplitude
calibration and from the formal errors of the model fits. The position error is
given by $\Delta r = \frac{\sigma \cdot \Theta}{2 S_{\mathrm{P}}}$ (Fomalont 1989), where σ is the residual noise of the map
after the subtraction of the model, θ the full width at half maximum (FWHM)
of the component and S_{peak} the peak flux density. This formula tends to un-
derestimate the error if the peak flux density is very high or the width of the
component is small. Therefore we included an additional error estimate arising
from the position variations during the model fitting procedure.
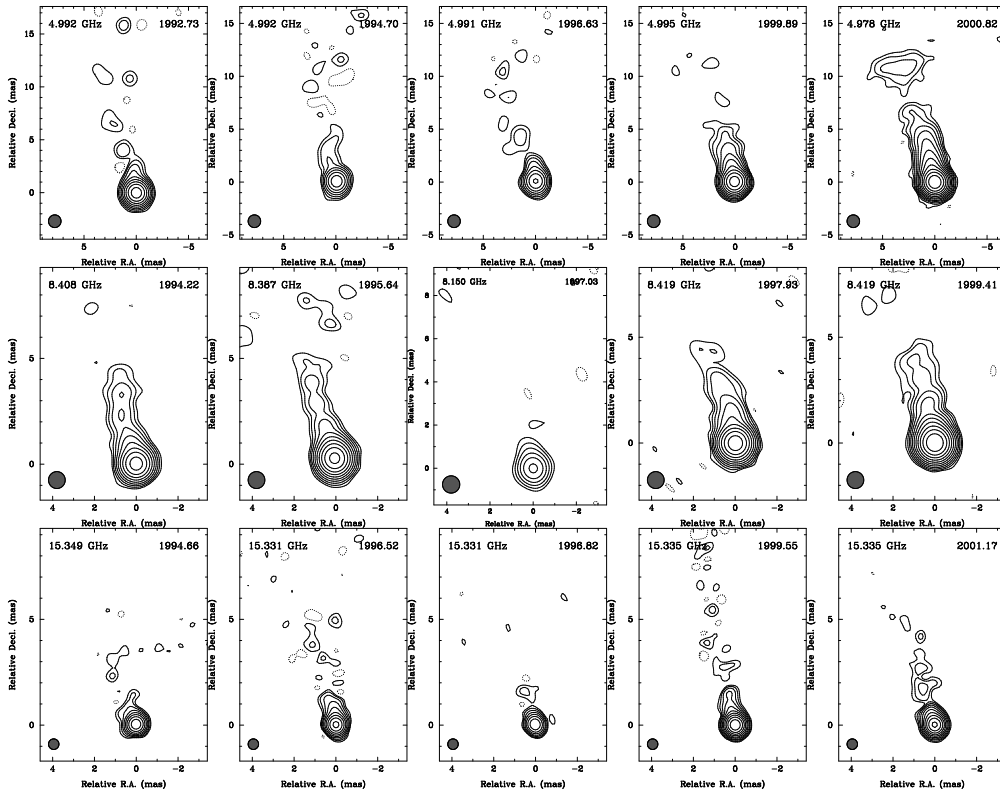
Figure 4.1: All contour maps of 0716+714 at 5 GHz (top row), 8 GHz (middle) and 15 GHz (bottom). The maps are convolved with circular beams of 1.2 mas at 5 GHz, 0.8 mas at 8 GHz and 0.5 mas at 15 GHz. Total flux density, original beam size and the level of the lowest contour at 3σ is given in the observing log (Table 4.1). Contours are increasing by steps of two.
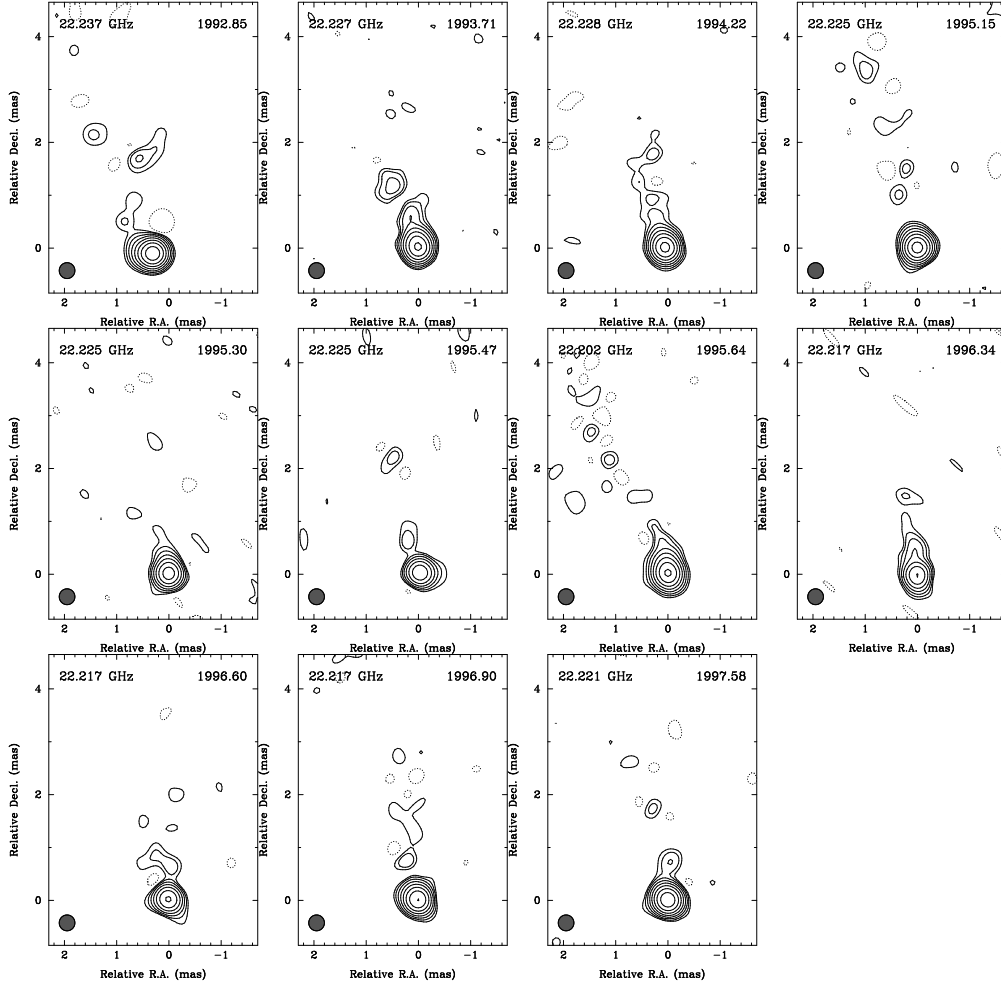
Figure 4.2: All contour maps of 0716+714 at 22 GHz. The maps are convolved with a circular beam of 0.3 mas. Total flux density, original beam size and the level of the lowest contour at 3σ is given in the observing log (Table 4.1). Contours are increasing by steps of two.

Table 4.2: Results from Gaussian Model fitting and component parameters.

Epoch	ν [GHz]	S [mJy]	r [mas]	ϕ [°]	θ [mas]	Id.[a]
1992.73	5.0	596 ± 89.4	–	–	0.10 ± 0.02	Core
		37 ± 5.5	0.83 ± 0.12	17 ± 8	0.14 ± 0.03	C05
		19 ± 2.8	1.92 ± 0.13	8 ± 3	0.60 ± 0.12	C03
		8 ± 1.2	5.02 ± 0.24	17 ± 2	0.93 ± 0.19	C01
		7 ± 1.0	11.46 ± 0.49	13 ± 2	3.35 ± 0.67	X
1992.85	22.2	708 ± 106.2	–	–	0.18 ± 0.04	Core
		12 ± 1.8	1.37 ± 0.06	12 ± 2	0.10 ± 0.02	C04
		16 ± 2.4	2.86 ± 0.22	0 ± 4	1.48 ± 0.30	C02
1993.71	22.2	272 ± 40.8	–	–	0.05 ± 0.01	Core
		79 ± 11.8	0.19 ± 0.02	15 ± 5	0.05 ± 0.01	C07
		14 ± 2.1	0.58 ± 0.07	14 ± 6	0.12 ± 0.02	C06
		14 ± 2.1	1.22 ± 0.09	20 ± 4	0.23 ± 0.05	C05
1994.21	22.2	309 ± 46.3	–	–	0.09 ± 0.02	Core
		15 ± 1.9	0.28 ± 0.09	28 ± 18	0.01 ± 0.00	C07
		13 ± 1.9	0.80 ± 0.13	15 ± 9	0.42 ± 0.08	C06
		7 ± 1.0	1.79 ± 0.16	14 ± 5	0.38 ± 0.08	C04
1994.21	8.4	266 ± 39.9	–	–	0.14 ± 0.03	Core
		25 ± 3.7	0.82 ± 0.09	13 ± 6	0.42 ± 0.08	C06
		10 ± 1.5	1.99 ± 0.19	17 ± 5	0.76 ± 0.15	C04
		9 ± 1.3	3.27 ± 0.22	12 ± 3	0.84 ± 0.17	C02
		4 ± 0.6	4.70 ± 0.43	14 ± 5	1.48 ± 0.30	X
1994.67	15.3	413 ± 61.9	–	–	0.07 ± 0.01	Core
		20 ± 4.0	0.55 ± 0.11	14 ± 11	0.64 ± 0.13	C07
		14 ± 2.1	2.82 ± 0.24	14 ± 5	1.68 ± 0.34	C03
1994.70	5.0	284 ± 42.6	–	–	0.18 ± 0.04	Core
		26 ± 3.9	0.56 ± 0.06	7 ± 6	0.21 ± 0.04	C07
		13 ± 1.9	1.86 ± 0.17	18 ± 5	0.77 ± 0.15	C05
		12 ± 1.8	3.00 ± 0.17	15 ± 3	0.72 ± 0.14	C03
		7 ± 1.0	4.34 ± 0.32	8 ± 4	1.45 ± 0.29	C02
1995.15	22.2	724 ± 108.6	–	–	0.07 ± 0.01	Core
		24 ± 3.6	0.23 ± 0.04	12 ± 9	0.07 ± 0.01	C08
		9 ± 1.3	1.17 ± 0.06	12 ± 3	0.07 ± 0.01	C06
		2 ± 0.3	2.37 ± 0.19	14 ± 4	0.15 ± 0.03	C04
		10 ± 1.5	3.43 ± 0.10	15 ± 1	0.20 ± 0.04	C03
1995.31	22.2	421 ± 63.1	–	–	0.10 ± 0.02	Core
		16 ± 2.4	0.27 ± 0.06	12 ± 11	0.10 ± 0.02	C08
		7 ± 1.0	0.77 ± 0.08	14 ± 6	0.10 ± 0.02	C07
1995.47	22.2	174 ± 26.1	–	–	0.04 ± 0.01	Core
		14 ± 2.1	0.31 ± 0.05	29 ± 9	0.07 ± 0.01	C08
		6 ± 0.9	0.85 ± 0.07	18 ± 4	0.06 ± 0.01	C07
		6 ± 0.9	2.07 ± 0.19	23 ± 5	0.43 ± 0.09	C05
1995.65	22.2	220 ± 33.0	–	–	0.07 ± 0.01	Core
		81 ± 12.1	0.16 ± 0.02	10 ± 6	0.05 ± 0.01	C09
		29 ± 4.3	0.40 ± 0.07	13 ± 10	0.32 ± 0.06	C08
1995.65	8.4	252 ± 37.8	–	–	0.11 ± 0.02	Core
		32 ± 4.8	0.43 ± 0.10	9 ± 12	0.10 ± 0.02	C08
		8 ± 1.2	1.36 ± 0.18	15 ± 7	0.53 ± 0.11	C06

Table 4.2 – continued from previous page

Epoch	ν [GHz]	S [mJy]	r [mas]	ϕ [°]	θ [mas]	Id.[a]
		3 ± 0.4	2.64 ± 0.26	20 ± 5	0.40 ± 0.08	C04
		5 ± 0.8	3.97 ± 0.34	15 ± 5	1.19 ± 0.24	C03
1996.34	22.2	221 ± 33.1	–	–	0.08 ± 0.02	Core
		35 ± 5.3	0.43 ± 0.06	9 ± 7	0.24 ± 0.05	C09
		10 ± 1.5	0.97 ± 0.09	12 ± 5	0.15 ± 0.03	C07
		6 ± 0.9	1.47 ± 0.13	5 ± 5	0.20 ± 0.04	C06
1996.53	15.3	225 ± 33.8	–	–	0.08 ± 0.02	Core
		17 ± 2.6	0.33 ± 0.05	9 ± 8	0.08 ± 0.02	C09
		15 ± 2.2	0.75 ± 0.09	4 ± 6	0.23 ± 0.05	C08
		4 ± 0.6	1.33 ± 0.23	17 ± 9	0.43 ± 0.09	C07
		3 ± 0.4	4.12 ± 0.34	15 ± 4	0.71 ± 0.14	C03
		1 ± 0.1	5.14 ± 0.24	27 ± 2	0.12 ± 0.02	C02
1996.60	22.2	218 ± 32.7	–	–	0.06 ± 0.01	Core
		17 ± 2.6	0.73 ± 0.09	6 ± 6	0.26 ± 0.05	C08
		3 ± 0.4	1.16 ± 0.19	15 ± 9	0.22 ± 0.04	C07
		4 ± 0.6	1.78 ± 0.08	19 ± 2	0.05 ± 0.01	C06
1996.63	5.0	183 ± 27.4	–	–	0.03 ± 0.01	Core
		22 ± 3.3	1.19 ± 0.07	9 ± 3	0.24 ± 0.05	C07
		8 ± 1.2	4.09 ± 0.27	20 ± 3	1.19 ± 0.24	C03
		7 ± 1.0	9.58 ± 0.49	23 ± 2	3.39 ± 0.68	C01
		3 ± 0.4	12.06 ± 0.44	10 ± 2	1.14 ± 0.23	X
1996.82	15.3	251 ± 37.6	–	–	0.01 ± 0.00	Core
		13 ± 1.9	0.40 ± 0.06	19 ± 7	0.08 ± 0.02	C09
		10 ± 1.5	1.49 ± 0.16	12 ± 6	0.51 ± 0.10	C07
1996.90	22.2	260 ± 39.0	–	–	0.04 ± 0.01	Core
		24 ± 3.6	0.22 ± 0.04	22 ± 10	0.08 ± 0.02	C10
		3 ± 0.4	0.76 ± 0.12	16 ± 8	0.08 ± 0.02	C08
		7 ± 1.0	1.54 ± 0.16	7 ± 6	0.38 ± 0.08	C07
		3 ± 0.4	4.69 ± 0.29	13 ± 3	0.50 ± 0.10	C03
1997.03	8.4	194 ± 29.2	–	–	0.09 ± 0.02	Core
		22 ± 3.3	0.77 ± 0.07	12 ± 5	0.23 ± 0.05	C08
1997.58	22.2	929 ± 139.4	–	–	0.07 ± 0.01	Core
		6 ± 0.9	0.24 ± 0.14	43 ± 29	0.01 ± 0.00	C10
		32 ± 4.8	0.51 ± 0.07	7 ± 7	0.32 ± 0.06	C09
		7 ± 1.0	1.69 ± 0.07	11 ± 2	0.06 ± 0.01	C07
1997.93	8.4	385 ± 57.7	–	–	0.10 ± 0.02	Core
		19 ± 2.8	0.72 ± 0.06	14 ± 5	0.16 ± 0.03	C09
		15 ± 2.2	1.54 ± 0.10	7 ± 3	0.30 ± 0.06	C07
		7 ± 1.0	3.18 ± 0.24	15 ± 4	0.84 ± 0.17	C05
1999.41	8.4	922 ± 138.3	–	–	0.10 ± 0.02	Core
		60 ± 9.0	0.68 ± 0.07	10 ± 5	0.10 ± 0.02	C10
		17 ± 2.6	1.58 ± 0.08	13 ± 2	0.20 ± 0.04	C08
		4 ± 0.6	3.16 ± 0.19	6 ± 3	0.28 ± 0.06	C06
		4 ± 0.6	3.78 ± 0.22	15 ± 3	0.40 ± 0.08	C05
1999.55	15.3	1157 ± 173.6	–	–	0.06 ± 0.01	Core
		54 ± 8.1	0.40 ± 0.03	15 ± 3	0.08 ± 0.02	C11
		26 ± 3.9	1.12 ± 0.09	12 ± 4	0.39 ± 0.08	C09
		2 ± 0.3	1.89 ± 0.26	10 ± 8	0.28 ± 0.06	C08
		10 ± 1.5	2.90 ± 0.24	9 ± 4	1.17 ± 0.23	C06
1999.89	5.0	558 ± 83.7	–	–	0.18 ± 0.04	Core

Continued on next page

Table 4.2 – continued from previous page

Epoch	ν [GHz]	S [mJy]	r [mas]	ϕ [°]	θ [mas]	Id.[a]
		39 ± 5.9	1.29 ± 0.11	8 ± 5	0.13 ± 0.03	C09
		19 ± 2.8	2.64 ± 0.15	10 ± 3	0.83 ± 0.17	C07
		6 ± 0.9	4.43 ± 0.29	12 ± 3	1.00 ± 0.20	C04
		1 ± 0.1	6.92 ± 0.98	18 ± 8	1.93 ± 0.39	C02
		7 ± 1.0	11.86 ± 0.58	17 ± 2	4.79 ± 0.96	C01
2000.82	5.0	520 ± 78.1	–	–	0.12 ± 0.02	Core
		35 ± 5.3	0.77 ± 0.12	20 ± 8	0.10 ± 0.02	C11
		25 ± 3.9	1.63 ± 0.09	12 ± 3	0.42 ± 0.08	C09
		11 ± 1.6	2.71 ± 0.18	11 ± 3	0.74 ± 0.15	C07
		9 ± 1.4	4.16 ± 0.26	11 ± 3	1.25 ± 0.25	C05
		8 ± 1.3	11.16 ± 0.51	17 ± 2	4.43 ± 0.89	C01
2001.17	15.3	549 ± 82.4	–	–	0.06 ± 0.01	Core
		72 ± 10.8	0.45 ± 0.04	20 ± 4	0.18 ± 0.04	C12
		14 ± 2.1	1.81 ± 0.16	17 ± 5	0.70 ± 0.14	C09
		5 ± 0.8	3.06 ± 0.22	13 ± 4	0.49 ± 0.10	C07
		3 ± 0.4	5.08 ± 0.29	16 ± 3	0.51 ± 0.10	C04

[a] Identification of the individual components. If a component appeared only in a single epoch it is labelled with X.

4.2 Results and Discussion

4.2.1 Identification of the Components

To investigate the kinematics in the jet of 0716+714, we cross-identified individual model components along the jet using their distance from the VLBI core, flux density and size. Since the observations were not phase-referenced, the absolute position information was lost, and it is impossible to tell which component, if any, is stationary. To register the images and to test the stability of the VLBI-core position, we compared the core separations of the jet components of each epoch with respect to the adjacent observations, but we could not find any systematic position offsets. We also checked for position shifts between the jet components at higher and lower frequencies due to opacity effects (Lobanov 1998). Inspection of close or simultaneously observed frequency pairs does not show a systematic frequency shift between higher and lower frequencies larger than 0.1 mas (position accuracy between 15 GHz and 22 GHz is < 0.1 mas). Therefore, we conclude that the core position is stationary and that all component positions can be measured with respect to this brightest component.

The cross identification of moving VLBI components between different times and frequencies is not unambiguous and depends on the dynamic range of the individual maps and on the time sampling. When we started our analysis we used the following scenarios as working hypothesis:

1. Stationary core with stationary or slow moving jet,

2. stationary core with fast moving jet,

3. non-stationary core with fast or slow moving jet,

   4. non-monotonic motion of the jet.

   As more data become available, we could rule out most of these identifica-
tion schemes, and we were left with a scheme that assumes a stationary core
and relatively fast component motion. The different schemes were tested, first
separately at each frequency and later with all modelfits combined.

   Supported by a graphical analysis, which is presented in Figure 4.3, we could
obtain a satisfactory scenario for the kinematics in the jet of 0716+714. This
scenario consists of 11 identified superluminal components moving away from
the core. To illustrate that the same identification can be obtained using only
a single frequency, although certainly not with the same confidence, the core
distances of individual VLBI components derived from our model fits at 22 GHz
is plotted against time in Figure 4.4. As an example of the procedure we used
for the identification of all components we show the identification scheme for
the separate frequencies for component C5, C7, C8 and C9 in Figure 4.5. Again
the frequency shifts between the trajectories are typically smaller than 0.1 mas
to 0.2 mas and are smaller than the measurement uncertainty Δr.
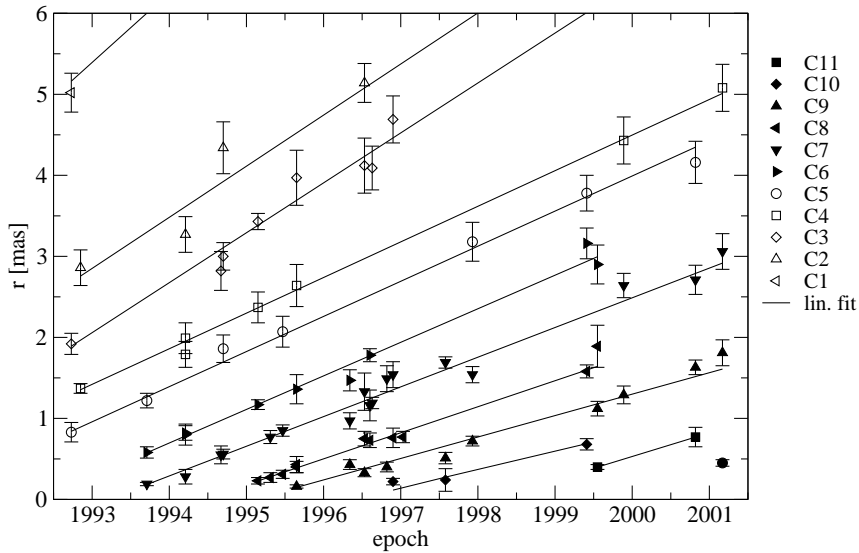
Figure 4.3: Core separation as a function of time for the individual modelfit components.
Data from all frequencies are combined. Possible frequency-dependent position shifts are less
than 0.1 mas and are not corrected. The solid lines show the linear fits to the path for each
component.

   Table 4.3 summarizes the angular separation rate μ of the VLBI components
derived from the linear fits of $r(t)$ and the corresponding apparent speed $\beta_{app} = v_{app}/c$ for an assumed redshift of 0.3.

4.2.2   The Kinematic Model

The components in this scenario move with $0.2\,\mathrm{mas\,yr^{-1}}$ to $0.6\,\mathrm{mas\,yr^{-1}}$ in
the inner part of the VLBI jet ($r \leq 3\,\mathrm{mas}$) and with up to $0.9\,\mathrm{mas\,yr^{-1}}$ in
the outer regions. Due to the inhomogeneous time sampling, it is sometimes
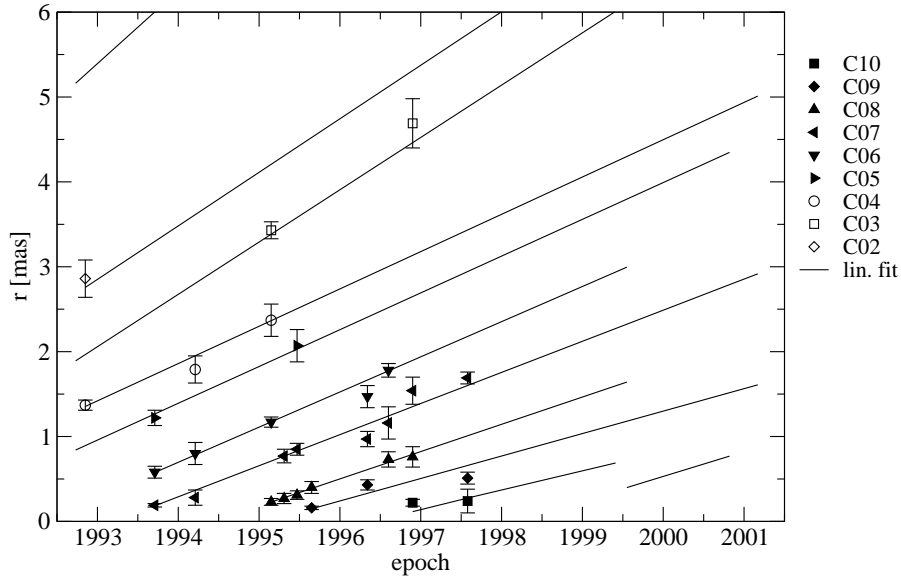
Figure 4.4: Core separation as a function of time for the individual jet components at 22 GHz. The solid lines show the linear fits to the path for each component, when combining the data from all frequencies.
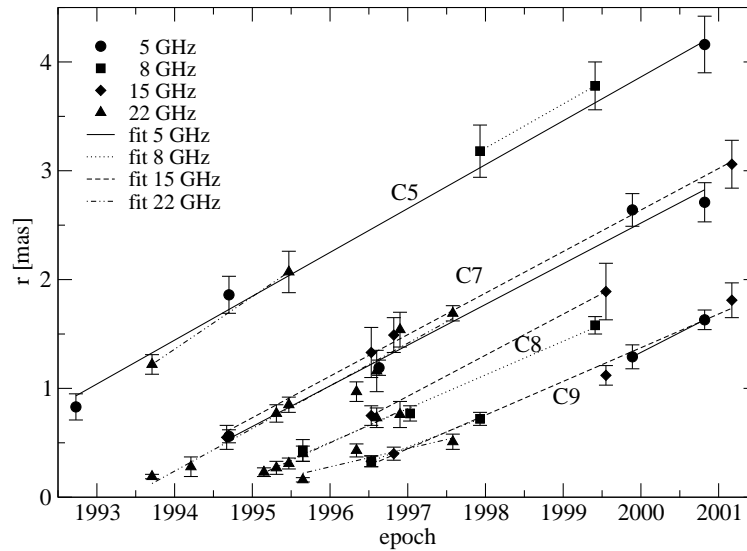
Figure 4.5: Core separation as a function of time for the components C5, C7, C8 and C9 at different frequencies. The solid lines show the linear fits to the path for each component. Shifts between the paths at different frequencies are visible, but are typically smaller than the measured uncertainties.

difficult to identify components over a long time interval. However, especially between 1993 and 1996, when we made many measurements spaced by only a few months, our proposed component identification gives the simplest and most reasonable fit to the data. Since most of our data were obtained at high frequencies, where the outer region of the jet is faint and already partly resolved by the interferometer beam, the parameter of the corresponding jet components (at $r \geq 4\,\text{mas}$) are not so well constrained as the inner jet components and therefore they have larger positional errors. Despite this, there is still a very distinct tendency for the older components (C1 – C3), which now are located at large core separations, to move faster than the components located in the inner jet (C4 – C10). This behaviour is also visible in Table 4.3, which shows a clear trend with systematically decreasing speeds between component C1 ($16\,c$) and component C10 ($4.5\,c$). The coarse time sampling for the individual jet components unfortunately does not allow us to fit acceleration to $r(t)$. Future and more densely sampled VLBI observations have to show whether the inner jet components indeed move linearly.

Table 4.3: Proper motions in the jet of 0716+714. The number of data points which were used for the fit for each component is given in column 2. The last column gives the back-extrapolated ejection dates of the components, which results from the linear fits.

Id.	#	μ [mas/yr]	β_{app} ($z = 0.3$)	Ejection date
C1	4	0.86 ± 0.13	16.13 ± 2.36	1986.7 ± 1.3
C2	5	0.63 ± 0.10	11.87 ± 1.82	1988.5 ± 1.0
C3	8	0.62 ± 0.04	11.59 ± 0.76	1989.7 ± 0.3
C4	7	0.44 ± 0.01	8.27 ± 0.24	1989.8 ± 0.1
C5	7	0.43 ± 0.02	8.16 ± 0.29	1990.8 ± 0.2
C6	9	0.41 ± 0.02	7.80 ± 0.33	1992.3 ± 0.1
C7	17	0.37 ± 0.01	6.89 ± 0.19	1993.2 ± 0.1
C8	11	0.32 ± 0.01	6.04 ± 0.20	1994.4 ± 0.1
C9	10	0.26 ± 0.01	4.98 ± 0.27	1995.1 ± 0.1
C10	3	0.24 ± 0.01	4.52 ± 0.45	1996.5 ± 0.2
C11	2	0.29 ± 0.02	5.48 ± 0.55	1998.2 ± 0.3

We adopt the relation for the luminosity distance, d_{L}:

$$d_{\text{L}} = \frac{c}{H_0}(1+z)\left[\eta(1,\Omega_{\text{m}}) - \eta(\frac{1}{1+z},\Omega_{\text{m}})\right] \qquad (4.1)$$

$$\eta(a,\Omega_{\text{m}}) = 2\sqrt{s^3+1}\left[\frac{1}{a^4} - 0.1540\frac{s}{a^3} + 0.4304\frac{s^2}{a^2}\right.$$

$$\left. +0.19097\frac{s^3}{a} + 0.066941s^4\right]^{-\frac{1}{8}},$$

$$s^3 = \frac{1-\Omega_{\text{m}}}{\Omega_{\text{m}}}.$$

that is an analytical fit to the luminosity distance for flat cosmologies with a

cosmological constant (Pen 1999). For the range of $0.2 \geq q_m \geq 1.0$, the relative error of the distance is less than 0.4% for any given redshift. We use

$$\beta_{app} = \frac{\mu \, d_L}{c \, (1+z)} \tag{4.2}$$

for the transformation of apparent angular separation rates μ into spatial apparent speeds (β_{app}) (Pearson & Zensus 1987). Assuming $z = 0.3$ for 0716+714, one milliarcsecond corresponds to $4.4\,pc$ and the measured angular separation rates correspond to speeds of $4.5\,c$ to $16.1\,c$. A discussion of the consequences of a different redshifts is given in Section 4.2.6. For the components C3 to C9, for which the proper motion determination is the most confident (over seven data points), the average motion is $\mu = (0.41 \pm 0.11)\,mas\,yr^{-1}$ which corresponds to $\beta_{app} = 7.7 \pm 2.1$. A preliminary analysis by Tian et al. (2001), who used only part of the data presented here, gave very similar speeds. A recently published kinematic analysis of the data from the VLBA 2 cm Survey also measured motion of $10\,c$ to $12\,c$ in the jet of 0716+714 (Kellermann et al. 2004). The speeds found in our paper are lower than the $16\,c$ to $21\,c$ found by Jorstad et al. (2001)[1], who observed the source over only a short time interval (3 yr). The difference between their and our results may be explained by slightly different (and unfortunately not unambiguous) map parameterizations using different Gaussian models or by non-linear component motion, with possible acceleration during shorter periods of time.

With an average apparent jet speed of about $8\,c$ and likely higher speeds of up to $15\,c$ to $20\,c$, 0716+714 displays considerably faster motion than other BL Lac objects, for which speeds of $\leq 5\,c$ are regarded as normal (e.g., Gabuzda et al. 2000b; Ros et al. 2002; Vermeulen & Cohen 1994). In this context it appears that 0716+714 is an extreme BL Lac object with a jet speed (and Lorentz factor) much higher than regarded typical for BL Lac objects and close to the speeds of $10\,c$ to $20\,c$ seen in quasars.

4.2.3 Kinematics and Geometry of the Jet

Using the measured motion, $(11.6 \pm 0.8)\,c$, of C3, the fastest, best constrained jet component in our model, we can place limits on the jet speed and orientation of 0716+174. Adopting

$$\beta_{app} = \frac{\beta \sin \theta}{1 - \beta \cos \theta} \tag{4.3}$$

we find that the jet inclination, that maximises the apparent speed, θ_{max} is $4.9°$. From that, one derives a minimum Lorentz factor, $\gamma_{min} = (1 + \beta_{app}^2)^{1/2}$ of 11.6, which corresponds to a Doppler factor of $\delta_{min} = \gamma_{min}^{-1}(1 - \beta_{min} \cos \theta_{max})^{-1} = 11.7$, where $\beta_{min} = \sqrt{1 - \gamma_{min}^{-2}}$. For smaller viewing angles ($\theta \to 0$) the Doppler factor approaches $\delta = 2\gamma$, which yields $\delta = 11.7$ to 23.4 at viewing angles between $4.9°$ and $0°$ for component C3. Including the higher

---

[1]Jorstad et al. originally published $11\,c$ to $15\,c$ using $H_0 = 100\,km\,s^{-1}\,Mpc^{-1}$ and $q_0 = 0.1$. We corrected these numbers for the cosmological parameters used in this paper.

values found by Jorstad et al. (2001) and the highest speed derived from our data (16.1 c), a Doppler boosting factor of up to $\delta \geq 40$ appears possible.
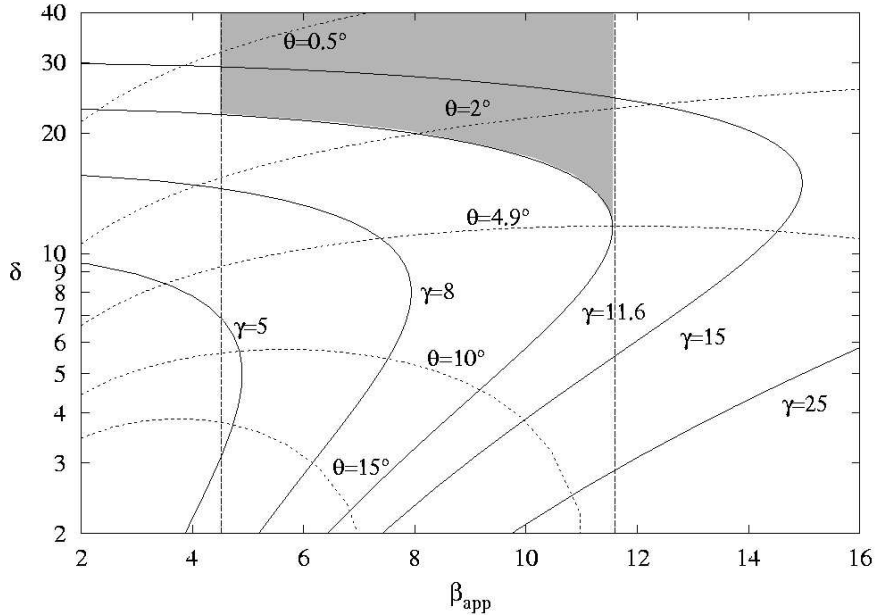
Figure 4.6: Shown is a diagram of the Doppler factor versus the apparent speed for constant intrinsic Lorentz factor, γ, (solid lines) and constant viewing angles θ (dotted lines). The range of measured speeds is indicated by the dashed lines and the grey shaded area marks the possible values for γ and θ (see text for details).

At cm-wavelengths, 0716+714 is a prominent intraday variable source, which shows amplitude variations of 5 % to 20 % on time-scales of 0.25 d to 2 d (Kraus et al. 2003; Wagner et al. 1996). Correlated radio-optical IDV observed in this source (Qian et al. 1996; Quirrenbach et al. 1991; Wagner et al. 1996) suggests that at least some fraction of the observed rapid variability has a source of intrinsic origin and cannot be attributed to refractive interstellar scintillation (RISS) alone, as is done for some other IDV sources (e.g., Kedziora-Chudczer et al. 2001; Qian et al. 2001; Rickett 2001b). The presence of the observed broad-band correlations of the variability and recently detected IDV at 9 mm wavelength, where RISS should not play a dominant role due to its λ^{-2} dependence (cf. Kraus et al. 2003; Krichbaum et al. 2002), further support a non negligible intrinsic contribution to the IDV in 0716+714. In the following we use a typical brightness temperature of $10^{15.5}$ K to 10^{17} K derived from the IDV observed at 6 cm. Slightly higher values of up to a few times 10^{18} K were measured only occasionally. To bring these brightness temperatures down to the inverse-Compton limit of 10^{12} K, Doppler factors in the range of $\delta = (T_{\rm b}/10^{12}\,{\rm K})^{\frac{1}{3}} \approx 30$ to 50 are required. Adopting these Doppler factors, we obtain jet Lorentz factors of $\gamma \approx 15$ to 25 and viewing angles of $\theta \leq 1°$.

The relation between the Doppler factor, intrinsic Lorentz factor, viewing angle and apparent speed is illustrated in Figure 4.6. The Doppler factors derived from IDV lie within the grey shaded area.

If we now try to explain the observed range of apparent component speeds through variations of the viewing angle (under the assumption of a constant Lorentz factor along the jet), we cannot reach slow apparent speeds of $\sim 4.5\,c$ without violating the lower limit of the Doppler factor of 2.1 from synchrotron self-Compton (SSC) models (Ghisellini et al. 1993). Therefore, we can exclude $\theta > 5°$ and the only solution remaining is to decrease the viewing angle which automatically leads to higher Doppler factors. The grey shaded area in Figure 4.6 marks the allowed region of Lorentz factors and viewing angles. It becomes obvious that we need at least a Lorentz factor of $\gamma \approx 15$ and a viewing angle of the VLBI jet of $\theta \approx 2°$ to explain the large range of observed apparent speeds as an effect of spatial jet bending. These values are consistent with those derived from IDV.

4.2.4   Flux Density Evolution

In Figure 4.7 we show the evolution of the flux density of VLBI components at 22 GHz with their increasing separation from the core. We show this frequency because a large fraction of the data were obtained at 22 GHz (11 epochs). With the exception of a few data points, the components fade as they travel down the jet. This agrees qualitatively with the theory of a conically expanding jet (e.g., Blandford & Königl 1979). As the VLBI components expand they become optically thin and their spectra steepen. This is illustrated for component C7 in Figure 4.8. The spectral index α is defined as $S \propto \nu^{\alpha}$. Knowing the turnover frequency and the size of a jet component allows us to calculate the strength of the magnetic field in the jet (e.g., Marscher 1983) as

$$B = 10^{-5} \; b(\alpha) \; \frac{\theta^4 \nu_{\mathrm{m}}^5 \delta}{S_{\mathrm{m}}^2 \, (1+z)} \; \text{gauss}, \qquad (4.4)$$

where $b(\alpha)$ is a tabulated parameter dependent on the spectral index (Table 1 in Marscher 1983) with a value ranging from 1.8 to 3.8 for optically thin emission ($\alpha = -0.25$ to -1.0), S_{m} (in Jy) is the flux density at the turnover frequency ν_{m} (in GHz) and θ (in mas) is the size of the component. If we calculate B for each of our modelfit components, without correcting for the Doppler factor δ, we get the apparent magnetic field along the jet. Since we do not have adequate spectra for all positions along the jet we will consider a decrease of the turnover frequency along the jet proportional to r^p, to correct for the expansion of the component. The best results are obtained when we start with a turn-over frequency of 4 GHz for the inner jet ($r \approx 0.2$ mas). This is plausible from the early spectrum (1994) of component C7 (Figure 4.8) though the turnover is actually not observed, and use $p = -1.3$, which is in good agreement with the relativistic jet model (Marscher & Gear 1985). For all components along the jet we derive magnetic fields in the range of $10^{-4}\,\delta\,\mathrm{G}$ to $10^{-7}\,\delta\,\mathrm{G}$. Since the minimum magnetic field strength that should be present due the energy density of the cosmic microwave background is a few microgauss (e.g., van der Laan & Perola 1969) the $10^{-7}\,\delta\,\mathrm{G}$ already imply a Doppler factor of about 10. At this stage the core component is excluded from the analysis because both the source size and the turnover frequency are poorly known.
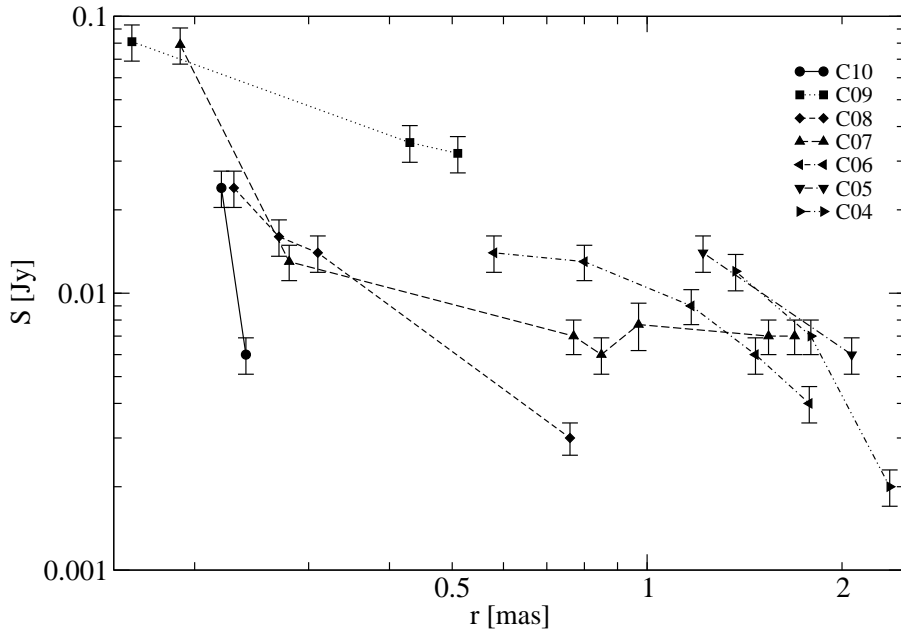
Figure 4.7: Flux density of the VLBI components at 22 GHz plotted versus core separation. The components fade as they travel down the jet.

Assuming equipartition between the energy of the particles, E_e, and the energy of the magnetic field, E_B, one can also derive the minimum magnetic field from the synchrotron luminosity, L.

$$L = 4\pi \, d_L^2 \, (1 + z) \int_{\nu_1}^{\nu_2} S \, d\nu \qquad (4.5)$$

$$E_e = f(\alpha, \nu_1, \nu_2) \, L \, B^{-1.5}, \qquad (4.6)$$

where $f(\alpha, \nu_1, \nu_2)$ is a tabulated function (e.g., Pacholczyk 1970) and ν_1 and ν_2 are the upper and lower cutoff frequencies of the synchrotron spectrum with typically values of 10 MHz to 10^8 MHz. Taking the energy density of the magnetic field $1/8\pi \, B^2$ and assuming spherical symmetry the total energy of the source is

$$E_{\text{tot}} = (1 + k)E_e + E_B \qquad (4.7)$$

$$= (1 + k) \, f(\alpha, \nu_1, \nu_2) \, L \, B^{-1.5} + \frac{1}{6} \, R^3 \, B^2,$$

where k is the energy ratio between the heavy particles and the electrons and R (in cm) is the size of the component. The ratio k depends on the mechanism of generation of the relativistic electrons, which is unknown at the present. It can range from $k \approx 1$ for an electron-positron plasma up to $k \approx 2000$, if most of the energy is carried in the protons. We used $k \approx 100$ in our calculations, which seems to be a reasonable value (e.g., Pacholczyk 1970). Given that $E_e \propto B^{-1.5}$

and $E_{\mathrm{B}} \propto B^2 \, E_{\mathrm{tot}}$ has a minimum and we find

$$
\begin{aligned}
B_{\mathrm{min}} &= \left(\frac{9}{2} \, (1+k) \, f(\alpha, \nu_1, \nu_2) \, L \, R^{-3} \right)^{2/7} \tag{4.8} \\
&= 5.37 \cdot 10^{12} \, (S_{\mathrm{m}} \, \nu_{\mathrm{m}} \, d_{\mathrm{L}}^2 \, R^{-3})^{2/7}.
\end{aligned}
$$

Using $z = 0.3$ and the same values for S_{m}, ν_{m} and θ as in Equation 4.4 we obtain magnetic fields between $10^{-4}\,\mathrm{G}$ and $10^{-2}\,\mathrm{G}$ for the jet. These values are larger than those derived before, which means that either the particles energy dominates and we do not have equipartition or that the emission is relativistically beamed. In the later case, the different dependence of the magnetic field from the Doppler factor in Equation 4.4 ($B \propto \delta^{-1}$) and in Equation 4.8 ($B_{\mathrm{min}} \propto \delta^{2/7\alpha+1}$) can be used to calculate the Doppler factor from $B_{\mathrm{min}}/B = \delta^{2+2/7\alpha}$. Comparing the results from all jet components yields Doppler factors of 5 to 50 with a mean value of 17. Although based on many assumptions these values are in good agreement with those derived from the kinematics.
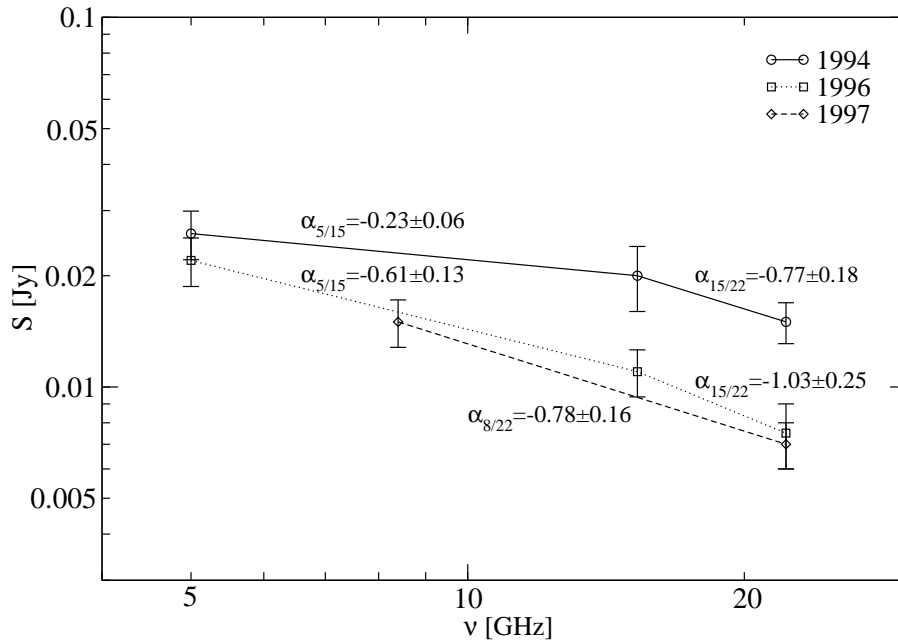
Figure 4.8: Spectral evolution of component C7.

In Figure 4.9 we show the long-term radio variability and the spectral index of 0716+714 over the time range in which the VLBI components were born. We show a combined data set with flux-density measurements at 5 GHz and 15 GHz from the UMRAO flux-density monitoring program (Aller et al. 2003) and from our flux-density monitoring performed with the 100 m radio telescope at Effelsberg (Peng et al. 2000). A detailed discussion of the flux-density variability using these and other data was recently done by Raiteri et al. (2003). Here, we restrict the discussion to a possible correlation of the radio variability with the ejection of new jet components. The ejection dates of new VLBI compo-

nents are indicated by the grey shadowed areas. Their widths correspond to the uncertainty in the back-extrapolated ejection dates (see Table 4.3). Although these uncertainties are rather large and the time sampling of the light curves is not always dense enough, a weak correlation between the ejection of new components and the flares in the radio bands is obvious. Each of the shaded areas either lies at or shortly before the time of a flux density increase of at least one of the two observing bands.

The two outbursts in mid 1992 and early 1995, which are best seen in the 2 cm band, are both surrounded by two new components, but the time sampling is too sparse to draw any further conclusions. In the lower panel of Figure 4.9 we calculated the spectral index between 5 GHz and 15 GHz, from the two light curves. Since the light curves were not measured simultaneously we searched for the closest pairs in the data set and calculated the spectral index from these pairs. The mean separation between two points is about eight days. The graph itself represents an eight-point running average to reduce the noise in the data. This figure shows an obvious correlation between the spectral index variations and the ejection of a new VLBI component. Seven out of eight ejection of a new VLBI components are accompanied by a flattening of the source spectrum. The exception is component C9. The flattening is in good agreement with an expanding component that becomes optically thin first at the higher frequency and later at the lower frequency (e.g., Marscher & Gear 1985).

We note that at the times of particularly dense time sampling (after 1994) a number of minor radio flares are visible, which are not related to the ejection of any of the known VLBI components. According to the light-house model and other related helical-jet models (e.g., Camenzind & Krockenberger 1992; Roland et al. 1994) it is possible that initial outbursts, which are related to the ejection of new jet components are followed by secondary flux density variations, which are not or only indirectly related to the component ejection. Of course, it is also possible that we missed some jet components in our infrequently sampled VLBI monitoring.

To test the significance of the correlations found by eye, we repeatedly placed eight fields with a similar width randomly over the light curves between 1989 and 1999 and each time determined how many coincided with a flare in the light curve or a flattening of the spectrum. For the light curves this test yielded a 50 % probability of our results occurring at random. The probability of measuring a flattening of the spectrum in seven out of eight components selected at random from our spectrum is 5.7 %. Generally a result is accepted to be statistically significant if the probability is below 5 % , which means that the correlations of the light curve with the ejection dates are likely to be a coincidence, but given that we might have missed a component the correlation of the spectral index might be significant. A coordinated and much denser sampled multi-frequency flux density and VLBI monitoring is necessary to study in more detail such outburst-ejection relations.
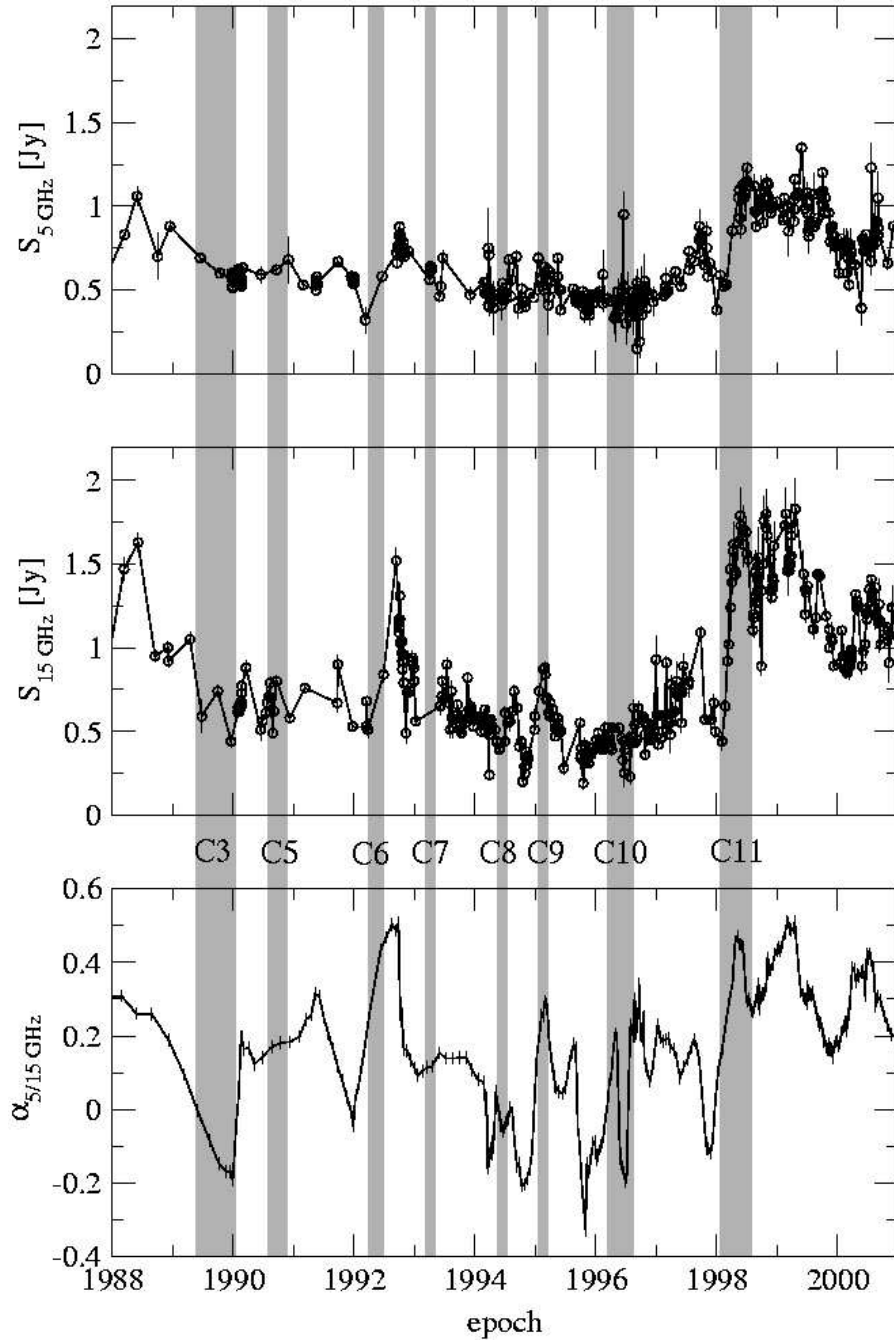
Figure 4.9: The long term flux density variability of 0716+714 as measured at Effelsberg and with the Michigan radio telescope at 5 GHz (top) and 15 GHz (middle) and the spectral index (bottom), $\alpha_{5/15\,\mathrm{GHz}}$. The shaded areas mark the ejection dates of the VLBI components and their uncertainties.

4.2.5 Variation of the Ejection Position Angle and Core Flux Density

The visual inspection of position angle of the innermost portion of the VLBI jet in the maps of Figure 4.1 & 4.2 indicates a variation of the P.A. of the jet near the core with time. To quantify this, we used the Gaussian models and fitted a straight line to the first milliarcsecond of the jet. For each observing epoch, the position angle of this line provides a good estimate of the direction of the inner portion of the VLBI jet. In Figure 4.10 (top panel) we plot the P.A. grouped in one year time bins to reduce the noise.
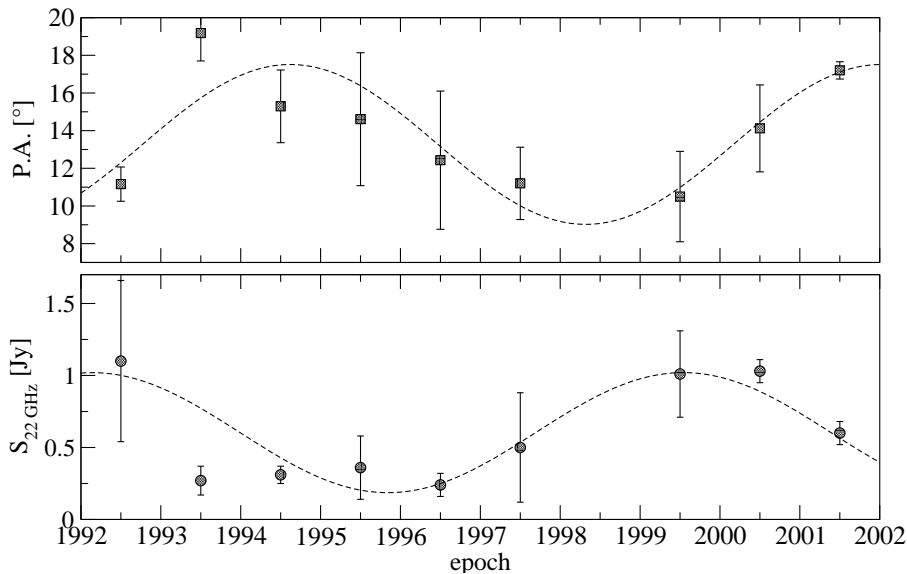
Figure 4.10: Top: Position angle of the central 1 mas of the VLBI jet grouped in one year time bins. The dashed line is a sinusoidal fit to the data. The position angle of the inner jet (ejection angle) varies with a period of ~ 7.4 years. Bottom: One year bins of the 22 GHz core flux density. The dashed line represents a sinusoidal fit with a fixed period of 7.4 years.

A sinusoidal fit to the data reveals a period of (7.4 ± 1.5) yr. The fit yields a reduced χ_r^2 of 1.55, which is much better than the χ_r^2 of 4.28, obtained for a linear fit. Unfortunately our data cover only one period of the variability and it will be interesting to see if the trend holds in the future. A possible explanation for such periodic variation would be a precessing footpoint of the jet. This should also result in a flux density variation of the VLBI core, and indeed, there is a tendency in the core flux density at 22 GHz is consistent with a periodic variation of ~ 7 yr (see Figure 4.10, bottom panel). Recently Raiteri et al. (2003) published an analysis of the optical and radio flux density variability of 0716+714 and found a periodicity of 5.5 yr to 6.0 yr for the flux-density variations in the radio regime. This is compatible within the error bars with the periodicity of the P.A. in the inner region of the jet. Based on the geometrical considerations in Sect. 4.2.3, the apparent peak to peak variation of $\approx 7°$ of the ejection angle corresponds to a small change of only $7° \sin \theta \approx 0.6°$ of the jet direction.

Such small variations of a few degrees in the rest frame of the source in several years have recently been detected also in other AGN, e.g. 3C 345 (Biretta

et al. 1986), 3C 279 (Carrara et al. 1993), 3C 273 (Krichbaum et al. 2001) and
BL Lac (Stirling et al. 2003). The most common explanation is a precessing
jet, which could be caused by a binary super-massive black hole system (e.g.,
Biretta et al. 1986; Britzen et al. 2001; Hummel et al. 1992) or a warped accre-
tion disc (Lai 2003 and ref. therein). However, also hydrodynamic effects can
lead to a precession of the jet (e.g., Hughes et al. 2002). In this case the pre-
cession is introduced by a potentially strong oblique internal shock that arises
from asymmetric perturbation of the flow.

4.2.6   Redshift Dependence of the Results

Since all the derived parameters of the kinematics and the geometry scale with
the distance to 0716+714, knowing the redshift is of great importance. The
distance to 0716+714 and therewith the speeds of the jet components scale
nearly linearly with z at these low redshifts. Thus a redshift decrease by a factor
of three would also decrease the Doppler factor by three. The dependence of
brightness temperature derived from IDV is $T_{\mathrm{b}} \sim T_{\mathrm{b}}' \left(\frac{z}{1+z}\right)^2$ (e.g., a decrease
from $z = 0.3$ to $z = 0.1$ would reduce T_{b} by a factor of 6.4). Since, $T_{\mathrm{b}} \propto \delta^{\sim 3}$ this
would increase the discrepancy between the Doppler factor, which is needed to
reduce T_{b} and the Doppler factor derived from the kinematics. An increase in
redshift would bring the derived parameters closer together.

Our assumption of the redshift of $z \geq 0.3$ is based on the non-detection
of an underlying host galaxy by Wagner et al. (1996). BL Lac host galaxies
have typical absolute magnitudes of $M_{\mathrm{R}} \approx -24$ and an effective radius of $r_{\mathrm{c}} \approx$
10 kpc (Jannuzi et al. 1997 and ref. therein). The lower limit of Wagner et
al. corresponds to an absolute magnitude of $M_{\mathrm{R}} = -20.4$, which would be an
unusually faint BL Lac host and so is a very conservative lower limit. An upper
limit for the redshift can be given from the lack of absorption by foreground
galaxies, which results in a redshift of $z \leq 0.5$ (Wagner priv. comm.). The
new findings by Kadler et al. (2004), who reports the possible detection of a
Fe K_α line in X-rays at 5.8 keV, which corresponds to a redshift of 0.10 ± 0.04,
would cause serious problems for understanding the nature of the host galaxy of
0716+714. A confirmation of this detection with future observations is urgently
needed.

4.3   Conclusions

We analysed 26 epochs of VLBI data at 4.9 GHz, 8.4 GHz, 15.3 GHz, and
22.2 GHz observed over 10 yr, between 1992 and 2001, and derived a new kine-
matic scenario for the jet in 0716+714. In this scenario the components move
with apparent speeds of $4.5\,c$ to $16.1\,c$ ($z = 0.3$). These speeds are atypically
fast for BL Lac objects, which typically exhibit speeds of $\leq 5\,c$ (e.g., Gabuzda
et al. 2000b; Ros et al. 2002; Vermeulen & Cohen 1994). Since this analysis is
based on much denser sampled VLBI data than previous studies, we are con-
vinced that we can rule out the somewhat slower scenarios which were presented
previously (e.g., Gabuzda et al. 1998; Schalinski et al. 1992; Witzel et al. 1988).

We find a periodic variation of the P.A. of the innermost jet which could be a sign of jet precession on a time-scale of (7.4 ± 1.5) yr. If this can be confirmed in future observations the higher speeds found by Jorstad et al. (2001) might be explained by non-linear motion of the jet components.

No correlation was found between the component ejection and radio flux density flares at the cm-wavelengths. There seems to be a weak correlation between the ejection of new components and the flattening of the radio spectrum.

From the component motion in the jet, we obtain a lower limit for the Lorentz factor of 11.6 and a maximum angle to the line of sight of $4.9°$. To explain the large range of observed apparent speeds as an effect of spatial jet bending, a Lorentz factor of $\gamma > 15$ and a viewing angle of the VLBI jet of $\theta < 2°$ are more likely. Under these circumstances, the Doppler factor would be $\delta \approx 20$ to 30. Such high Doppler factors are indeed required in order to explain the high apparent brightness temperatures of up to 10^{17} K derived from intraday variability at cm-wavelengths.

Chapter 5

VSOP Polarimetry of 0716+714

In this chapter the linear polarization properties and especially its short term day-to-day variability of 0716+714 will be discussed. Magnetic fields are likely to play a crucial role in the formation and collimation of jets in active galactic nuclei and are a tracer of the underlying hydrodynamics of the jet, showing the effects of oblique shocks, boundary layer interactions, shear, turbulence, and cloud interactions. The technique of VLBI polarimetry (VLBP) provides information about the ordering of pc-scale magnetic fields, their orientation and the Faraday depth along the line of sight to, and within, the jets. The polarimetric observations we made were done with the VLBI Space Observatory Programme (VSOP). The VSOP mission is a Japanese program, which operates an 8 m radio telescope in an Earth orbit. The VSOP satellite was launched in February 1997. The satellite, named HALCA is in an elliptical orbit, with an apogee height of 21 000 km and a perigee height of 560 km, which enables us to make VLBI observations on baselines of about ($\sim 33\,000$ km) when combined with the ground based VLBI arrays. This is more than three times longer than those achievable on Earth ($\sim 10,000$ km). HALCA is capable of observations at 1.6 GHz and 5 GHz with a maximum bandwidth of 32 MHz. Since, HALCA orbits the earth in about 6,3 h, the data of the satellite is transmitted to several tracking stations (usually two to four) around the world that record the data on tape.

0716+714 is a prominent IDV source, showing variability in every wavelength band were it was observed. In the radio bands it is also known to be variable in linear polarization yielding amplitude modulations of up to 100 % together with a rotation of the polarization angle (Wagner & Witzel 1995 and ref. therein). A direct conclusion drawn from polarization IDV is the need of multiple components with different compactness and polarization that interact either due to deflection in the inter stellar medium or due to superposition of multiple components inside the beam. Since, IDV is more pronounced in longer wavelengths, but the resolution of interferometers decreases towards longer wavelengths, the high resolution of VSOP is needed to reveal the the ori-

gin of the rapid IDV in 0716+714. Therefore, a multi-epoch VSOP experiment was done in September and October 2000 yielding the resolution to study the small structures that are believed to cause the IDV.

The observations and the data reduction procedures will be described in Section 5.1. This section will be followed by the presentation and discussion of the results (Section 5.2) and at the end we will give a summary with the conclusions (Section 5.3).

5.1 Observations and Data Reduction

An array of 12 antennas consisting of the complete VLBA, Effelsberg and HALCA Space antenna was used to follow the short term variability of 0716+714 at 5 GHz within one week. The source was observed at three epochs, namely September 29 (project code: V053 A2), October 4 (V053 A4), and October 5 2000 (V053 A5). In some figures and tables the project code is used to identify the epochs. The observations yielded a nearly identical (u, v)-coverage (see Figure 5.1) and each epoch was of 16 h duration. A detailed observing log is given in Table 5.1. 0836+710 and 0615+830 were used as calibrators to check the stability of the amplitude calibration between the epochs and to calibrate the polarization data. The calibrators were not observed by the HALCA antenna, because it is not possible to steer HALCA to different source positions during one observation.

Table 5.1: Observing log. For each epoch and each source the total integration time, time together with HALCA, total flux density, the uniform weighted beam size and the residual noise are given.

Epoch	Source	Int. [h]	HALCA [h]	S_{tot} [Jy]	Beam [mas × mas]	P.A. [°]	S_{rms} [mJy]
Sep. 29[a]	0716+714[b]	7.67	2.75	0.55	0.58 × 0.27	−80	0.492
		7.67	0.00	0.58	0.95 × 0.78	−26	0.034
	0836+710	1.17	0.00	2.23	1.10 × 0.88	−10	0.193
	0615+820	1.17	0.00	0.74	0.90 × 0.78	−42	0.191
Oct. 4	0716+714[b]	7.72	4.59	0.52	0.58 × 0.23	−79	0.513
		7.72	0.00	0.55	0.92 × 0.77	−25	0.041
	0836+710	1.20	0.00	2.28	0.99 × 0.83	−46	0.168
	0615+820	1.19	0.00	0.75	0.84 × 0.82	−47	0.173
Oct. 5	0716+714[b]	7.92	5.47	0.52	0.58 × 0.24	−71	0.580
		7.92	0.00	0.56	0.85 × 0.81	−28	0.038
	0836+710	1.21	0.00	2.27	0.96 × 0.81	−74	0.175
	0615+820	1.23	0.00	0.76	0.93 × 0.76	−55	0.171

[a]In this epoch the Pie Town antenna was substituted by a single VLA antenna.
[b]Two lines are given for 0716+714. First line gives the parameters including HALCA and the second using only the ground array data.

The participation of Effelsberg made it possible to obtain simultaneous

single-dish measurements in total intensity and linear polarization for all programme sources. This, not only allows one to calibrate the electric vector polarization angle of the VLBI measurements, but also allows one to compare the single-dish variability with the structural variations seen in the VLBI images and so to locate the regions that are responsible for the variablity in 0716+714.

Although HALCA can only observe left circular polarization (LCP) one can do polarimetry if enough stations of the remaining network provide dual circular polarization measurements. One cross correlates LCP from HALCA with RCP from the ground array stations and thus obtain the cross-polarized correlations on the space baselines. Normally one needs both cross polarizations, RL and LR, to image the linear polarization of a source, but using a complex $Q + iU$ image it is possible to include antennas with only a single cross polarization (see Section 5.1.2). A detailed description of the polarimetric capabilities of HALCA is given in Kemball et al. (2000).
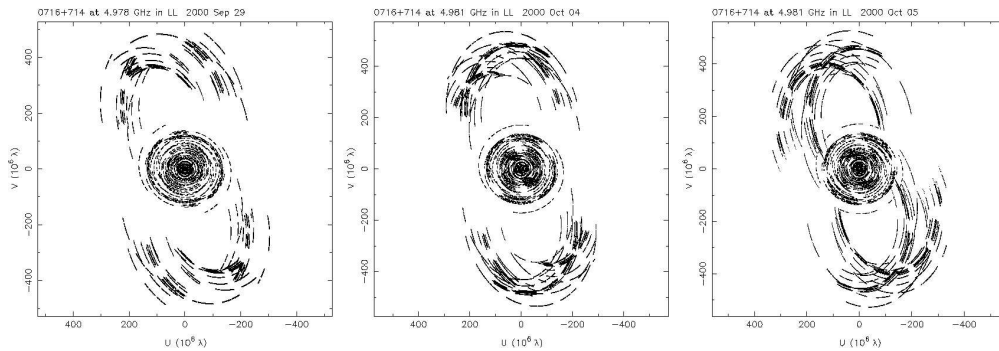
Figure 5.1: (u, v) coverage of 0716+714 at September 29 (left), October 4 (middle), October 5 (right). The individual coverages are nearly identical, which allows a reliable comparison of the obtained maps.

The data were recorded in VLBA format with two 16 MHz baseband channels per circular polarization in two-bit sampling, resulting in a recording rate of 256 Mbps at the ground array stations and, since HALCA recorded only LCP, a recording rate of 128 Mbps at the several tracking stations. The correlation was done at the VLBA correlator in Socorro, NM.

After loading the data into AIPS, the standard amplitude and phase calibration were performed. Given that the use of HALCA needs some extra care in the data reduction, we present a small How-To of VSOP data reduction in AIPS:

- FITLD loads the data from tape in to AIPS and is used with the standard inputs.

- MSORT sorts the (u, v) data in time.

- ACCOR corrects the amplitudes in the cross correlations, which might be wrong due to errors in the sampler threshold.

- UVCOP is necessary to extract only the cross correlation data. Since HALCA is not able to switch between sources it observes only the target

source, whereas the ground array observes various calibrators from time
to time. This causes problems with the index table and can be avoided if
one removes the auto-correlation data.

- INDXR creates a new index table.

- CLCOR (PANG) to remove the rotation of the parallactic angle.

- APCAL performs an amplitude calibration using provided T_{sys} and gain
  curve measurements.

- FRING; since HALCA does not provide pulse calibration information a
  manual phase calibration is needed to remove offsets between the two IF's.
  Usually HALCA is tracked by more than one tracking stations, therefore
  this step needs to be done for each tracking station separately.

- FRING performs a fringe fit for all data.

- CROSSPOL corrects the possible offsets between the IF's of the cross
  polarizations.

At this point the data were split (SPLIT) into separate files for each source
and exported as (u, v)-FITS files (FITTP) for further imaging and phase and
amplitude self-calibration using the CLEAN (Högbom 1974) and SELFCAL
procedures in Difmap (Shepherd 1994). Because of the small diameter of the
HALCA antenna, the data from the ground array stations yield a much bet-
ter signal to noise ratio (Figure 5.2). Therefore, we first imaged the ground
array data alone to be confident that the calibration was done correctly and
to get a good starting model. After this, we include also the HALCA base-
lines with a strong Gaussian taper ($10\,\%$ at $450\,\mathrm{M}\,\lambda$) at the beginning, which
was decreased during the self-calibration process. The self-calibration was done
in total intensity in steps of several phase-calibrations followed by careful am-
plitude calibration. During the iteration process the solution interval of the
amplitude self-calibration was shortened from intervals as long as the whole
observational time down to minutes. Finally the self-calibrated data were reim-
ported into Aips, where the calibration of the D-terms (see next Section) and
the polarization imaging was done.

5.1.1   Feed Calibration

To image the linear polarization of the sources one needs to calibrate the leak-
age terms (D-terms) from the left to the right circular polarization feeds at
each antenna and vice versa (see also Chapter 2 for further references). To
perform the calibration one needs a proper total-intensity model of the source
and to divide it into small sub-models using clean boxes, which can be done
conveniently using the Aips task CCEDT. Each of these sub-models should rep-
resent an isolated "component" with the same polarization properties. LPCAL
will then analyse the behaviour of the polarization angle with time to distin-
guish between the source intrinsic polarization, which should not rotate with a
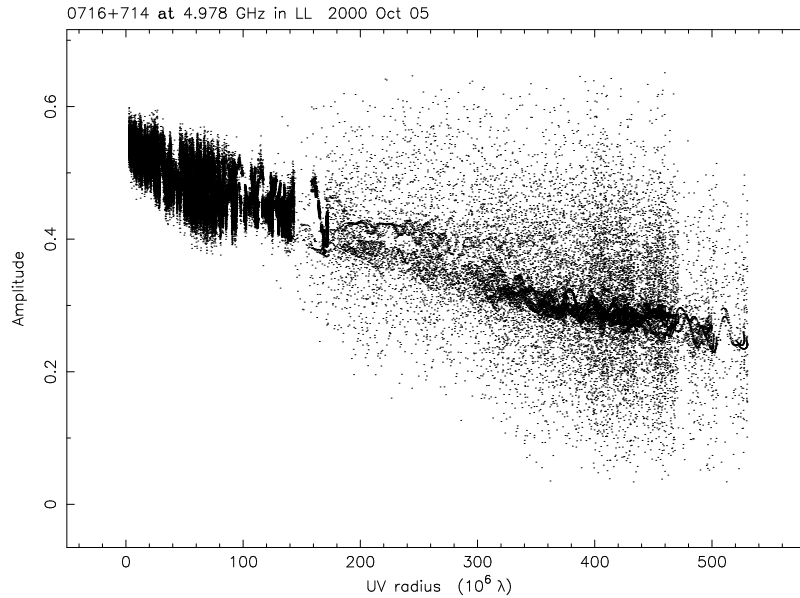
Figure 5.2: Amplitude vs. (u, v)-distance of 0716+714 (Oct. 5). Clearly visible is the higher noise at the HALCA baselines at large (u, v)-distances. The dotted line (marginally visible in the centre of the HALCA data) represents the final clean model).

change of the parallactic angle whereas the D-term of the telescope will rotate. In practice, one needs to iterate these steps a few times before the sub-models represent isolated components and one can be confident that the D-terms do not change significantly between the different source models.

The LPCAL algorithm is robust against different source structures, nevertheless one should prefer core-dominated sources for the calibration. All sources in our observations meet this criterion. The VLBA antennas and Effelsberg exhibit D-term values between 0.5 % and 2 % and for HALCA we derived about 4 %. A number of feed solutions was calculated by using slightly different source models and/or different calibrator sources (0816+710 and 0615+820). The RMS differences between these D-terms are typical smaller than 0.3 % for the ground array stations and reach ~ 0.5 % for the HALCA satellite. The D-terms of HALCA could only be checked with different source models of 0716+714, since the calibrators were not observed by the satellite. Plots of the real versus imaginary cross-hand polarization data indicated that a satisfactory D-term solution was obtained. This was also verified in plots of the real and imaginary cross-hand data versus (u, v) parallactic angle. After applying the D-term solution nearly no variation was seen as a function of (u, v) parallactic angle (see Figure 5.3). To estimate how the D-term variations affect the source polarization images, fractional polarization maps with different feed calibration tables were made and then subtracted. This yielded an accuracy of 0.1 % in fractional polarization for the core of 0716+714 and 1.2 % for the weaker jet. The effect of different D-terms on the accuracy of the EVPA was measured in a similar way. Here, we obtained an error of $0.3°$ on the core and about $2.0°$ in the jet.
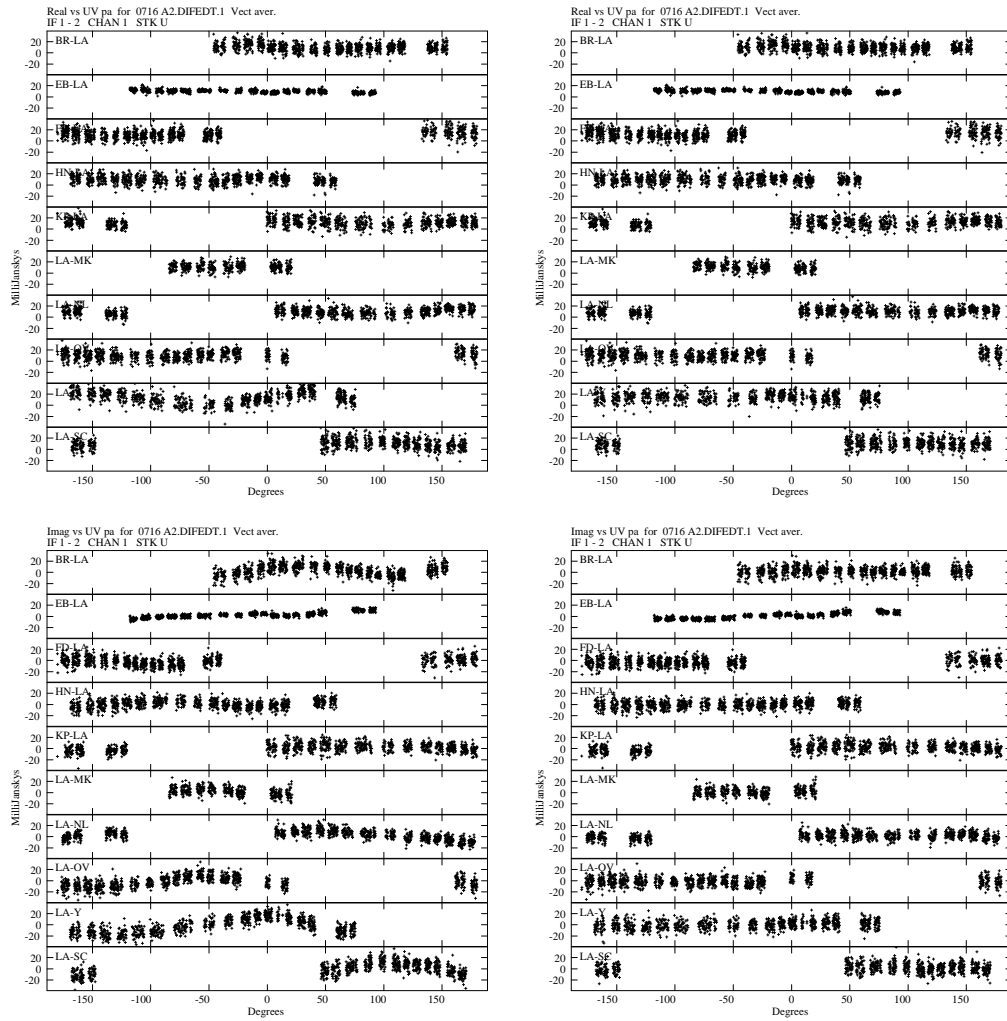
Figure 5.3: An example for the tests made to verify the D-term solutions: plots show the real (top) and imaginary part (bottom) of the Stokes U data on all ground array baselines to Los Alamos against the parallactic angle (Sep. 29). **Left panels:** Before D-term calibration was applied. **Right panels:** After D-term calibration was applied. The calibration improved the stability of the amplitudes vs. P.A. and nearly no variations are seen after the correction.

5.1.2   Polarization Imaging

The usual imaging technique for linear polarization is to form Q and U values
from the observed RL and LR correlations and separately image and deconvolve
the Q and U images. The task COMB can be used to combine the Q and U
images to obtain a linear polarization intensity map ($I_{\mathrm{P}} = \sqrt{Q^2 + U^2}$) and
a map which represents the electric vector polarization angle ($EVPA = \chi =
\arctan \frac{U}{Q}$). But this is only possible in observations, where both cross polarized
correlations, RL and LR, are available for each baseline.

   Since the HALCA antenna can only observe in LCP, only one of the cross
polarized correlations is present. However, it is still possible to form a linear
polarization image if a complex imaging and deconvolution of $Q + iU$ is used.
The Fourier transform of the complex $Q + iU$ image is in general asymmetric so
RL and LR measure different aspects of the source. Conversely, if the sampling
function is asymmetric (some measurements don't have both RL and LR) the
Fourier transform of the sampling function, the dirty beam, is complex. It is
therefore possible to use asymmetric sampling and produce a $Q + iU$ complex
image and complex beam. The complex deconvolution results in a complex
image for which the real part represents the Q emission from the sky and
the imaginary part the U emission. To build the complex image and beam
the procedure CXPOLN in AIPS can be used and the task CXCLN will do
a complex CLEAN to produce the Q and U images. These images can be
combined with COMB in the usual way to obtain linear polarization intensity
and polarization angle images.

5.1.3   EVPA Calibration

The orientation of the electric polarization vector in the VLBI maps was cali-
brated using the single dish measurements from Effelsberg of 0836+710. This
implies that most of the polarized emission seen by the Effelsberg telescope
is also present in the VLBI images. Comparing the linear polarization flux
densities suggest that this is indeed the case for our sources (see Table 5.2).
Therefore, the VLBI data were convolved with a very large beam, around two
times larger than the source structure, to get an average EVPA for the whole
map. The comparison to the single dish measurements of 0836+710 provided
the offset for which we corrected our VLBI maps. Unfortunately, 0615+820
is unpolarized it could not be used for this purpose and since 0716+714 is
variable it could also not be used. The Effelsberg measurements themselves
were calibrated in an iterative process using a technique first invented by Turlo
et al. (1985). A description specific for Effelsberg was recently given by Kraus
et al. (2003). For this technique one needs calibrators with known polarization
properties, or at least sources which are known to be variable only over longer
time-scales. In our observations we used 0836+710, 3C 286 and 0951+699,
which satisfy this criterion. After calibration, the residual error of the Effels-
berg EVPA was $\sim 0.3°$.

Table 5.2: Comparison of the VLBI and single dish linear polarization properties of 0836+710 used to calibrate the EVPA of the VLBI observations. The different value for the correction in the last epoch is due to the choice of a different reference antenna during the calibration.

Epoch	P_{Eff} [mJy]	χ_{Eff} [°]	P_{VLBI} [mJy]	χ_{VLBI} [°]	$\Delta\chi$ [°]
A2	160 ± 1	106.3 ± 0.3	131 ± 13	125.8 ± 1.2	-19.5 ± 1.2
A4	160 ± 1	106.3 ± 0.3	133 ± 13	125.6 ± 1.0	-19.3 ± 1.0
A5	160 ± 1	106.3 ± 0.3	128 ± 13	96.0 ± 1.1	10.3 ± 1.1

5.2 Results and Discussion

In this section the total intensity and linear polarization maps of 0716+714 from the ground array data and the VSOP data are presented and analysed. The high dynamic range of the ground array data (peak/rms $\sim 15\,000$) enables us to study the weak jet up to 12 mas from the core and the three times higher resolution in the VSOP images allows a detailed study of the core structure of 0716+714. The results and analysis of the single dish measurements of Effelsberg will be given in Section 5.2.3. It is worth mentioning here that 0716+714 did not show much variability in total intensity during each VSOP observation (see Figure 5.11). The contrary would violate the principle of aperture synthesis in interferometric imaging.

However, simulations of Hummel (1987) have shown that intraday variability during VLBI observations only reduces the achievable dynamic range without changing the source structure and he even considered much larger variations ($\sim 80\,\%$). Variations of about $4\,\%$, which are present in our observations, are smaller than the usual uncertainties of the T_{sys} measurements ($\sim 10\,\%$), that are used to calibrate the visibility amplitudes. Therefore, we can neglect the effects of the IDV on our VLBI maps. The larger variability of the linear polarization (up to $\sim 40\,\%$) might degrade the linear polarization images, but can not affect the self-calibration procedure, because the phase and amplitude self-calibration of LL, RR, LR, and RL during the imaging process was done using the total intensity data. The possible origins of the variablity will be discussed by comparing the measurements from the VLBI maps and the single dish measurements from Effelsberg in Section 5.2.4. Together with the results of the jet kinematics from the previous chapter one can also derive some basic parameters of the underlying shock in the jet, provided that the VLBI components correspond to moving shocks (Section 5.2.6).

5.2.1 Ground Array Data

The ground array images showing the parsec-scale structure of the jet of 0716+714 is shown in Figure 5.4. The panels in the left row show the total intensity contours of 0716+714 with polarization E-vectors superimposed for all three epochs. The jet is clearly visible up to 12 mas from the core in north-northeast direction (P.A. $\approx 15°$). Between the core and the jet a turn of $\sim 60°$ of the EVPA is visible. The right panels show the contour maps of the linear polariza-
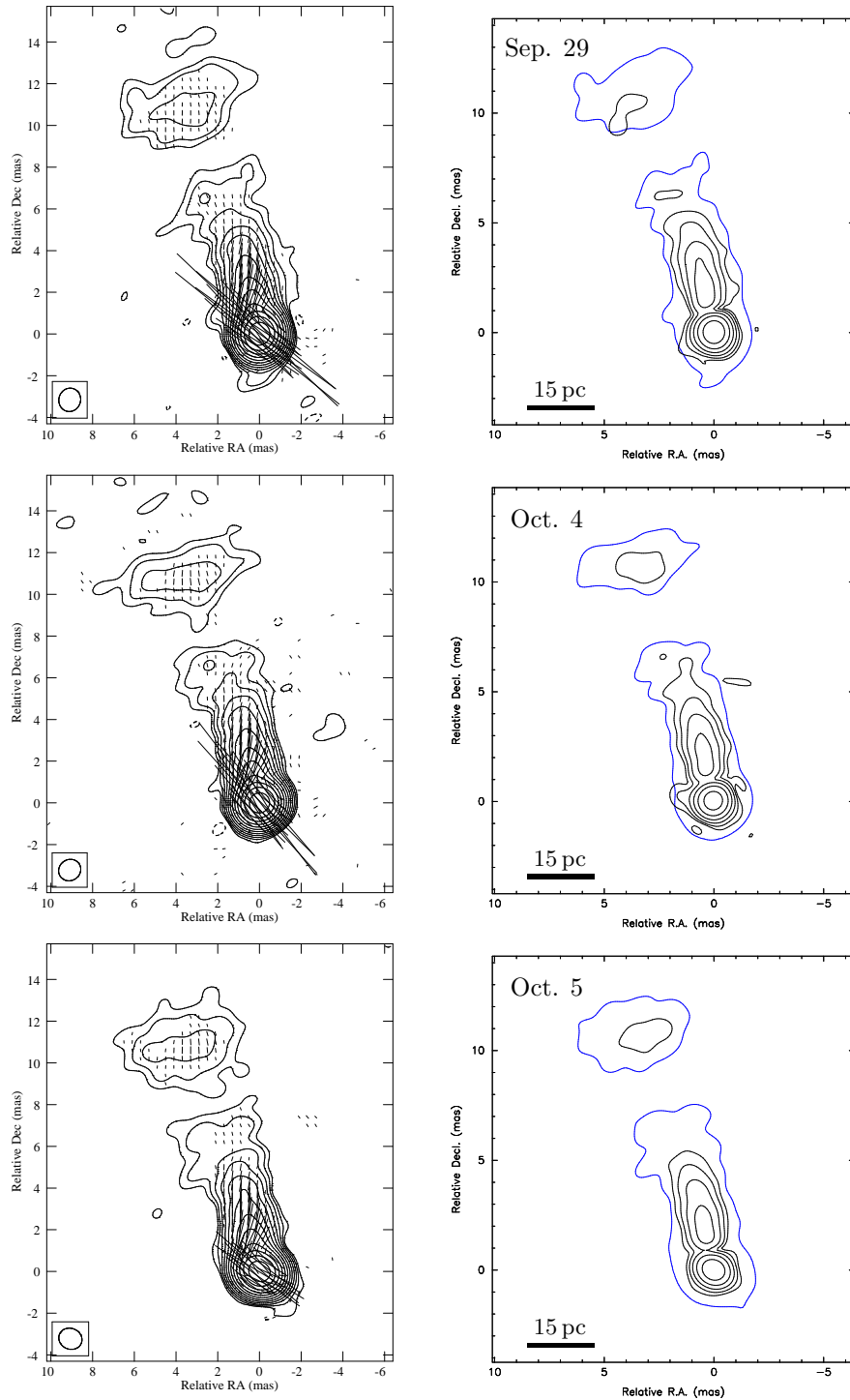
Figure 5.4: Left panels: Ground array contour maps of Stokes I of 0716+714 with polarization vectors superimposed. The length of the polarization vectors is proportional to the intensity of the linear polarization (1 mas corresponds to 2.5 mJy/beam in P). Contours start at 0.13 mJy/beam, increasing in steps of 2. **Right panels:** Contour maps of the linear polarization. Contours start at 0.25 mJy/beam, increasing in steps of 2. The lowest contour of the total intensity is given by the blue line. Time order is from top to bottom: 29 Sep, 4 Oct, and 5 Oct 2000. The beam size, total flux density and RMS are given in the observing log, Table 5.1.

tion. The jet electric field vectors are well aligned with the jet axis. Provided
that the jet emission is optically thin, which is supported by the high degree of
fractional polarization (Figure 5.6), the alignment suggests that the magnetic
field is oriented perpendicular to the jet axis. With respect to the jet, the elec-
tric field vectors of the core are misaligned by about 60°, which can be either
explained by the fact that the core is optically thick or by jet bending in the
inner region of the core. Recent 3 mm global VLBI observations at a resolution
of 50 μas provide evidence that the jet is strongly curved in the inner region
and therefore, support the later case (Figure 5.5). The 43 GHz map was ob-
tained from a snapshot observation during a regular monitoring of NRAO 150
and since it was obtained nearly simultaneously with the 86 GHz map, it can
be used to confirm the curved jet.
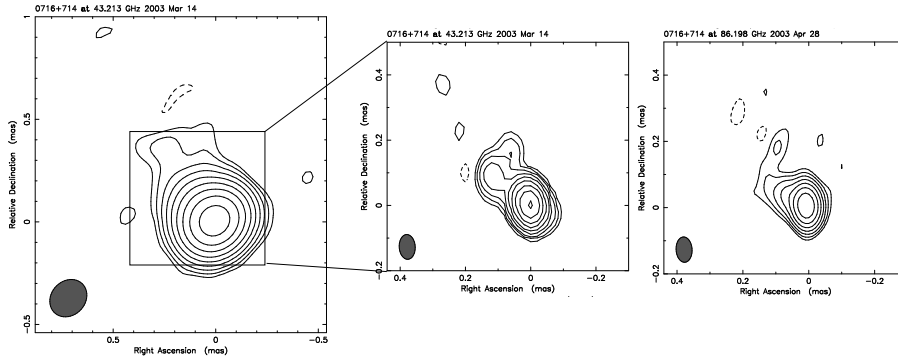
Figure 5.5: Contour images of 0716+714 at 43 GHz and 86 GHz showing that the jet is bent
by about 20° in the inner 1 mas with respect to the jet at lower resolution. **Left:** 43 GHz
VLBA contour map at a resolution of $166 \times 196 \mu$as at $-43.5°$ from March 14, 2003. The
peak flux density is 2 Jy/beam and the contours start at 6 mJy and increasing in steps of 2.
Middle: Super resolved ($76 \times 49 \mu$as at 3.5°) version of the 43 GHz map. **Right:** 86 GHz map
at a resolution of $76 \times 49 \mu$as at 3.5° from April 28, 2003. Peak flux density is 2.4 Jy/beam
and the contours start at 20 mJy.

At first sight, no major changes in the total intensity structure between the
epochs occur, but the integrated flux densities in Table 5.1 reveal a marginally
significant decrease of 5 % from the first to the last two epochs. In Table 5.3
the integrated flux densities are given separately for the core and the jet.

Table 5.3: Summary of the ground VLBI maps.

Epoch		I [mJy]	P [mJy]	χ [°]
A2	Core	520.3 ± 26.9	12.1 ± 1.3	49.4 ± 4.1
	Jet	$56.0 \pm\ 4.7$	7.4 ± 0.8	-10.8 ± 5.6
A4	Core	499.3 ± 26.1	11.8 ± 1.3	40.7 ± 4.0
	Jet	$54.8 \pm\ 6.3$	7.3 ± 0.8	-11.2 ± 7.8
A5	Core	503.9 ± 25.4	6.5 ± 1.1	52.7 ± 5.2
	Jet	$54.7 \pm\ 6.0$	7.5 ± 0.8	-9.5 ± 7.4

One can see that the core flux density decreases from 520 mJy to about

500 mJy in the later epochs whereas the jet flux density stays relatively stable at ~ 55 mJy. The measurements were made several times with the tasks IMSTAT and TVSTAT in AIPS and the errors are derived from the scattering of the individual measurements. The task IMSTAT integrates over a rectangular region that is not necessarily in good agreement with the source structure, whereas TVSTAT integrates over a polygonal region that is specified by the user. However, given that the flux density accuracy of the amplitude calibration itself (using gain curves and T_{sys} measurements) is limited to about 5 %, which was derived from the gain corrections during the amplitude self-calibration, it is so far questionable whether this is real source variability.
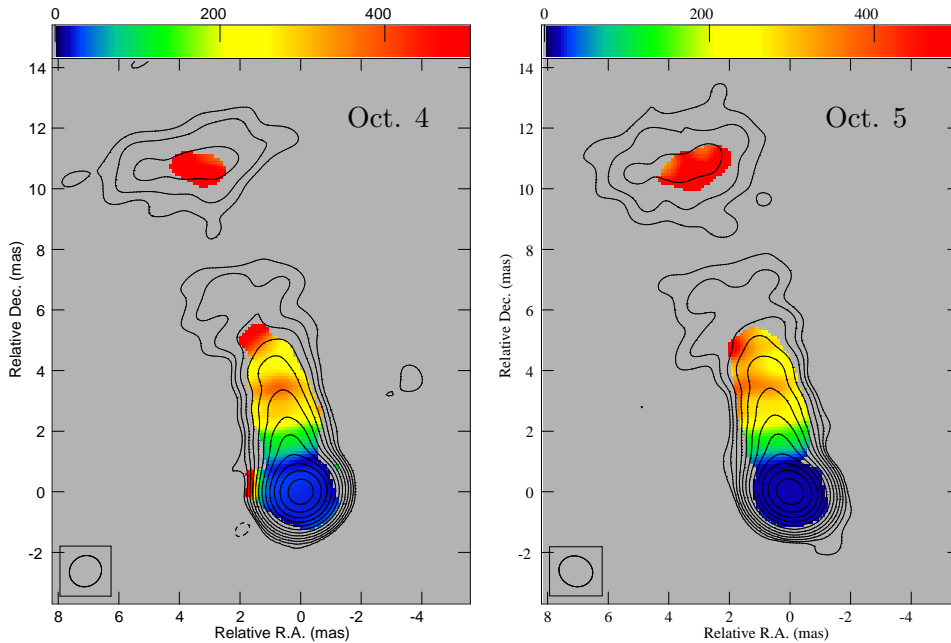
Figure 5.6: Fractional polarization maps of 0716+714. Shown are total intensity contours and the colours represent the fractional of polarization in milli-fractions of the total intensity.

Contrary to the marginal variability of the total flux density, strong variability is seen in linear polarization. An inspection by eye of the polarization vectors in Figure 5.4 indicates that the linear polarization of the core component varies significantly. From the integrated values in Table 5.3, one can see that there are (within the errors) no changes in the polarized intensity between the first two epochs, but in the last epoch the polarized intensity of the core drops by ~ 45 %, from ~ 12.0 mJy to ~ 6.5 mJy, corresponding to a decrease in fractional polarization from ~ 2.4 % to ~ 1.3 %. The polarized intensity of the jet shows no variability and stays constant at an average degree of polarization of ~ 13.6 %. The average EVPA of the jet is also constant at an angle of $\sim -10°$, whereas the core EVPA rotates from around $\sim 50°$ to $\sim 40°$ and back to $\sim 53°$ during the observations.

Fractional polarization maps are displayed in Figure 5.6. Since there were no changes between the Sep. 29 and Oct. 4, but change was seen between Oct. 4 and Oct. 5, only maps from the the last two epochs are shown. Noticeable are
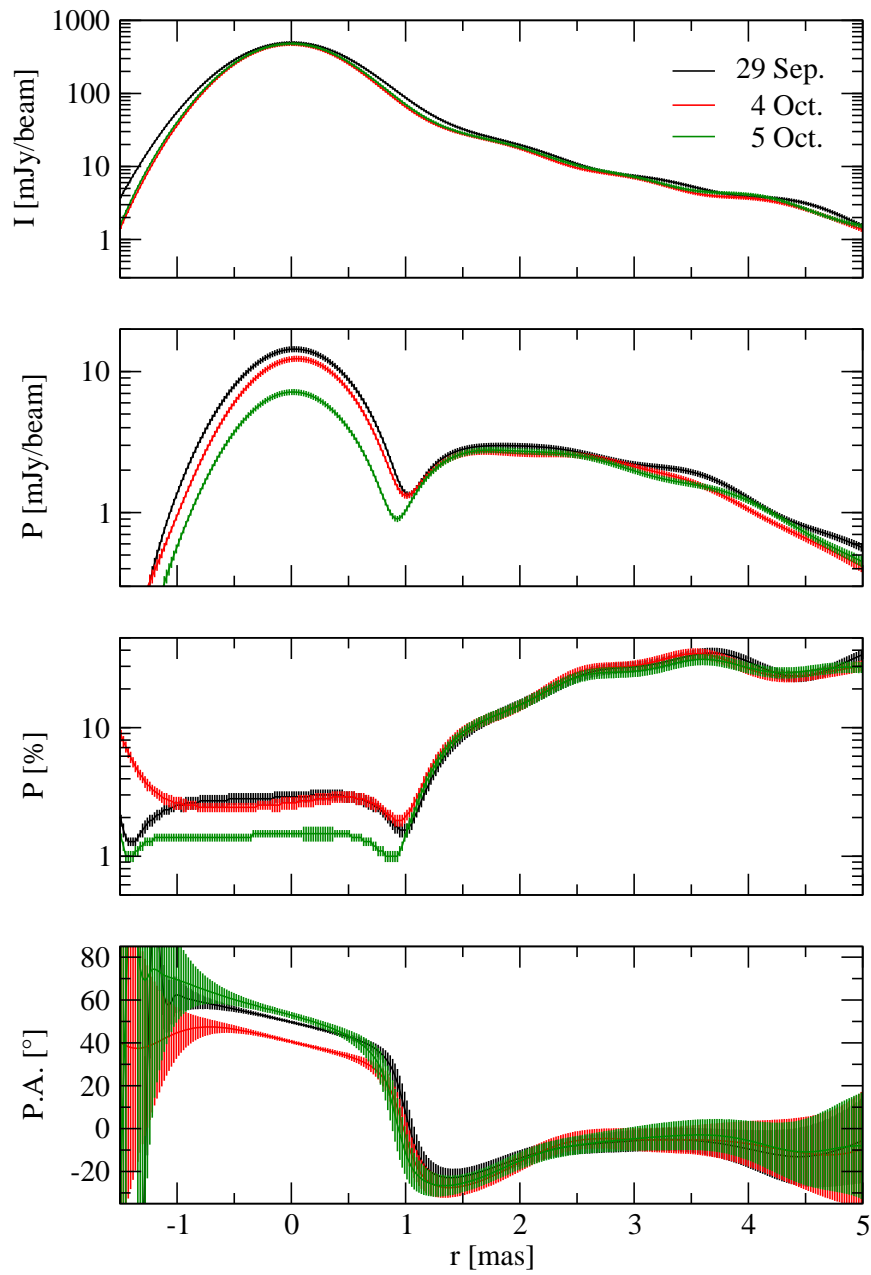
Figure 5.7: Slices through the total intensity, linear polarization intensity, fractional polarization and EVPA images of the core and the jet of 0716+714.

the two peaks of up to 40 % fractional polarization in the jet at 2.5 mas, 3.5 mas and 4.5 mas from the core (see also Figure 5.7). At the same positions we found modelfit components in total intensity that we used to study the kinematics in the jet (see Section 4.2 and Table 4.3) with motion of $6.9\,c$ to $8.3\,c$. This provides further evidence that these are real structures in the jet, probably shocks, where we might have a higher density that enhances the total intensity and a more ordered magnetic field that enhances the linear polarization.

Figure 5.7 shows profiles of total intensity, linear polarization, degree of polarization, and the orientation of the E-vector and summarises all these results. The errors of the total intensity and the polarization are dominated by the uncertainties of the amplitude calibration, of about 5 %. The error of the EVPA depends on the SNR of the linear polarization. Therefore, the error bars are scaled in such a way that they match the uncertainties for the core and the jet EVPA derived from the D-term analysis and the EVPA calibration (see Section 5.1.1 & 5.1.3). One can clearly see that there was no variation in the jet and that all the variations are due to the core component of 0716+714.

5.2.2 Space VLBI Data

Combining the VLBI ground stations with the radio antenna on board the satellite HALCA improves the resolution at 5 GHz by nearly a factor of three (see Table 5.1). Besides the higher resolution one has to hazard the low sensitivity of the HALCA antenna (diameter, $\varnothing = 8\,\text{m}$), which results in a higher noise on the longest baseline. The nominal system equivalent flux density (SEFD) of the HALCA antenna is 15300 Jy at 5 GHz (Hirabayashi et al. 2000) compared to 312 Jy at each VLBA antenna ($\varnothing = 25\,\text{m}$) and 18 Jy at Effelsberg ($\varnothing = 100\,\text{m}$). The I and P maps are presented in Figure 5.8. In total intensity the jet is visible up to 3 mas from the core, which dominates over the weak jet. This makes it easier to distinguish between the core and the jet as it was for the ground array only, when we want to measure their flux densities. In linear polarization only the core component was significantly detected and the jet was only marginal visible as indicated by the lowest contour. A summary of the integrated flux densities in I and P is given in Table 5.4.

In comparison with the ground array data (see Table 5.3) we measured a core flux density that was slightly lower, but a jet flux density that was comparable although the jet is much shorter. This is most likely because we could not properly separate the core from the jet in the ground array images and added some of the jet emission to the core. In all three epochs $\sim 6\,\%$ of the total flux density of ground array maps is missing in the VSOP maps, which is reasonable, since the outer jet is resolved and therefore much shorter. One can recover the missing flux density by using natural weighting, but this would also decrease the resolution. Since, we know from the ground array images that the jet flux density is not variable, and we now concentrate the study on the core region, we chose the highest possible resolution.

The VSOP images show the same variability behaviour as the ground array images. The total intensity varied only marginal, but the linearly polarized flux density of the core was highly variable. The integrated polarization flux
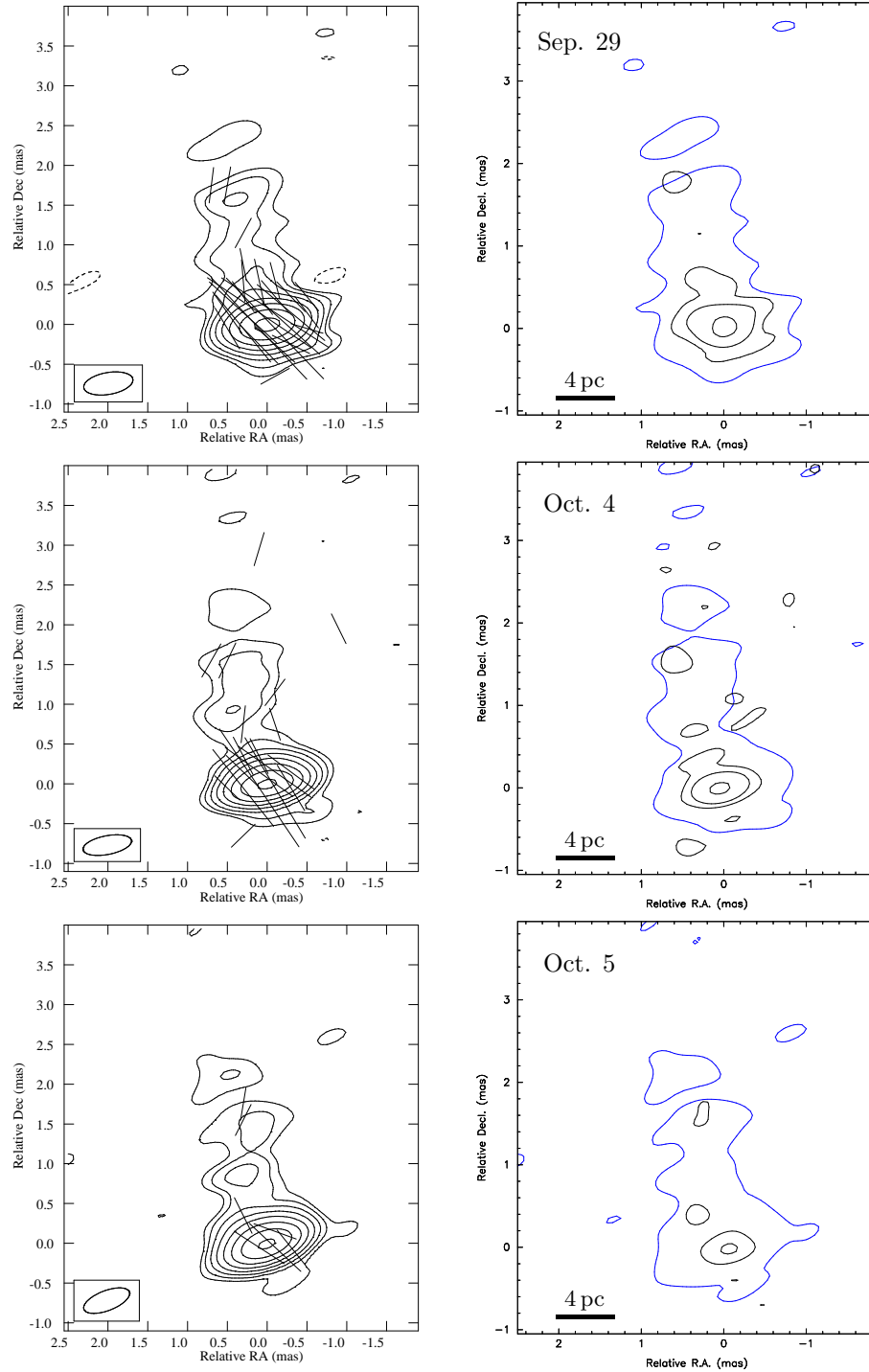
Figure 5.8: Left panels: VSOP contour maps of Stokes I of 0716+714 with polarization vectors superimposed (1 mas corresponds to 6.7 mJy/beam). Contours start at 2.5 mJy/beam and increasing in steps of 2. **Right panels:** Contour maps of the linear polarization. Contours start at 1.4 mJy/beam and increasing in steps of 2. The outline of the total intensity is indicated by the blue contour. Time order is from top to bottom: 29 Sep, 4 Oct, and 5 Oct 2000. The beam size, total flux density and RMS are given in the observing log, Table 5.1. Intensity profiles along the jet that better show the variability are given in Figure 5.9

Table 5.4: Summary of the flux densities of the VSOP maps.

Epoch		I [mJy]	P [mJy]	χ [°]
Sep.	Core	492.5 ± 25.0	9.8 ± 2.2	48.2 ± 6.3
29	Jet	62.4 ± 4.0		
Oct.	Core	465.4 ± 23.6	7.6 ± 1.9	40.3 ± 12.1
4	Jet	59.5 ± 3.7		
Oct.	Core	462.4 ± 23.3	4.3 ± 1.4	57.6 ± 11.5
5	Jet	60.1 ± 3.7		

densities of the core was somewhat lower then in the ground-array images, which is most likely due to confusion between the jet and the core region in the ground VLBI images. That the core itself is already resolved in the VSOP images can almost certainly be ruled out, since 0716+714 is one of the two sources that were detected in a 230 GHz VLBI observation on a transatlantic baseline. This sets an upper limit to the source size of $\sim 17\,\mu$as, derived from the resolution of the $\sim 6000\,$km baseline (Krichbaum et al. 2004).

The linear polarization in the jet has nearly vanished in the VSOP maps. The polarization peak flux density of the jet in the ground array maps is $\sim$ 3 mJy, which should be detectable with VSOP at a signal-to-noise ratio of $\sim$ 9. But the jet seems to be already resolved with VSOP and the peak flux density decreases to 1.5 mJy, which yields a $4\,\sigma$ detection. This corresponds approximately to the lowest contour in the polarization contour maps in the bottom panels in Figure 5.8.

As in the ground array maps, the EVPA in the core of 0716+714 rotate between the epochs. The vectors rotated within the errors by the same amount, namely around $-8°$ between the first and the second epoch and around $+17°$ between the second and the third epoch. A comparison of the EVPA profiles from Figure 5.9 and Figure 5.7 reveals a complex fine structure in the inner core region, which was not seen in the ground array profiles. There seem to be at least two components with different EVPA, one at $r \approx -0.12\,$mas and the other at $r \approx 0.25\,$mas, indicated by the slope of the EVPA between the two positions.

This becomes more obvious in the polarization profiles between the first and the second epoch (Figure 5.9). While the integrated flux density stayed nearly constant (see Table 5.4), the polarization profile changed.The core profile on Sep. 29 was much wider than five days later. Although, the noise in the VSOP maps is quite high ($\sim 0.4\,$mJy/beam) the changes are significant. The error bars indicate the $1\,\sigma$ error of the flux density. An exchange of the D-term calibration tables between the two epochs shows within the errors no changes of the flux densities and confirms the different shapes of the profiles. The fast changes of the polarization structure provides further evidence that the core itself is the sum of highly variable sub-components.

An attempt to reveal the underlying structure of the core is made in Figure 5.10. Motivated by the extended core structure of the first epoch, two Gaussian functions were fitted to the peak of the polarization profile. To better
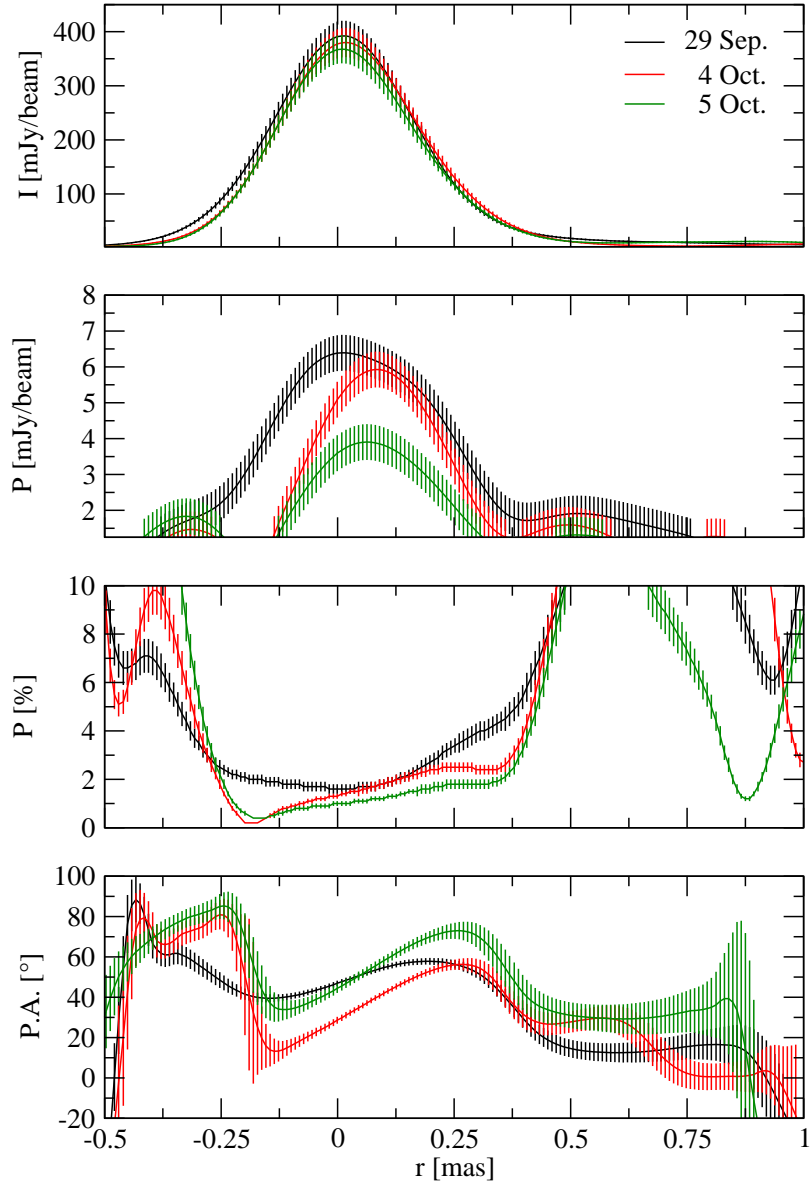
Figure 5.9: Slices through the total intensity, linear polarization intensity, fractional polarization and EVPA VSOP images of the core of 0716+714. It is a virtual zoom into the core region of Figure 5.7. $r = 0$ marks the same position in both plots.
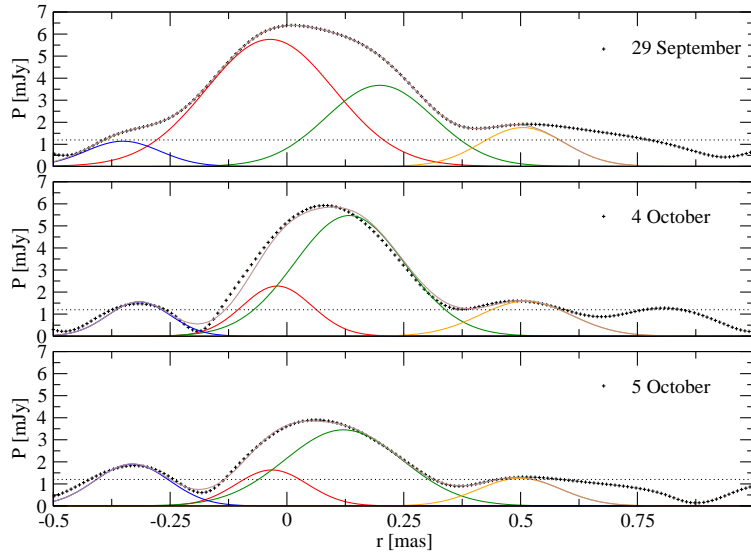
Figure 5.10: Gaussian fits to the central region of the VSOP linear polarization profiles (see Text for details). The parameters of the fits are given in Table 5.5.

constrain the position and the full width half maximum (FWHM) of the fits, two additional Gaussians were necessary and were fitted to the minor peaks left and right hand side to the main peak. Though the main peak in the last two epochs apparently need not to be fitted by two components, the two component model yields a much lower reduced χ_r^2. Fitting a single Gaussian yields a χ_r^2 of 3.9 (Oct. 4th) and 7.0 (Oct. 5th), whereas two Gaussians yield 1.1 and 1.4, respectively. The fits to the first epoch result in a χ_r^2 of 0.8. The resulting parameters of the fits are summarised in Table 5.5.

Within the errors the blue and the orange fits, that were fitted to the minor peaks, show no variability and are always at the same position. The two Gaussian functions in the centre instead show strong variability, but the green fit shows also a significant displacement by about $80\,\mu$as between Sep. 29 and Oct. 4. $80\,\mu$as correspond to about one third of the minor beam axis. This might indicate the existence of third component in the first epoch that vanishes in the later epochs, but attempts to fit a third component did not improve the χ_r^2.

The deconvolution of the FWHM with the beam size ($D = \sqrt{I^2 - B^2}$) yields a measurement of the source size D and the values of D are also given in Table 5.5. Since, the profiles were obtained along P.A. 15 ° and the beam major axis is oriented along P.A. $-80°$ to $-70°$ (see Table 5.1) the minor axis of the beam was used in the deconvolution. If D could not be calculated ($I < B$), the source diameter is assumed to be consistent with a point source, $D = 0$. However, if the variability is intrinsic to the source, the fact that we see a drop

Table 5.5: Summary of the Gaussian fits to the VSOP polarization profiles (Figure 5.10). To identify the individual fits each line is marked with a coloured bullet corresponding to the line colour of the fit in Figure 5.10. Shown are the peak flux density S_p, the full width half maximum (FWHM), the deconvolved size D (see text) and the peak position on the x-axis.

Epoch		S_p [mJy]	FWHM [mas]	D [mas]	x [mas]
A2	●	1.14	0.19	0.00	−0.35
	●	5.76	0.32	0.25	−0.04
	●	3.68	0.27	0.18	0.20
	●	1.76	0.22	0.07	0.50
A4	●	1.56	0.16	0.00	−0.32
	●	2.10	0.17	0.00	−0.03
	●	5.53	0.28	0.20	0.12
	●	1.57	0.23	0.11	0.50
A5	●	1.91	0.19	0.00	−0.33
	●	1.61	0.18	0.00	−0.03
	●	3.46	0.30	0.22	0.12
	●	1.26	0.22	0.07	0.50

of 40 % in polarized emission in 24 h gives us, due to the light propagation time (see also Section 1.3), an upper limit of the source size of $r < c \cdot \Delta t < 0.1\,\mu$as, which is much smaller than the about 0.1 mas that we are able to measure.

Small source sizes are also needed if the dominant source of the IDV is refractive inter stellar scattering (RISS). The source sizes that are inferred from RISS models are in the order of a few μas (e.g., Rickett 2001b). Therefore, the values derived from the fits (Table 5.5) have to be considered as upper limits and the real source sizes of the components that are causing the IDV are at least three or four times smaller.

5.2.3 Effelsberg Measurements

To have single-dish measurements simultaneous with the VSOP observations, gaps of several minutes between VLBI scans were included in the VLBI schedule. This allowed the 100 m antenna in Effelsberg, which was part of the array, to perform cross-scans in elevation and azimuth. Most of the measurements were made on the VLBI sources, but also additional flux density and polarization calibrators were observed. A list of all sources, the number of measurements and their mean flux density are given in Table 5.6.

The last two columns contain the modulation index m and the reduced χ_r^2 from a linear fit to the data. m is defined as $100\,\sigma_\mathrm{I}/I$, where σ_I is the standard deviation and is a first estimator if a source is variable. The modulation index is also affected by changing weather conditions and unstable receivers, but comparing the modulation index of the target source and the secondary calibrators helps to remove such uncertainties. A second estimator of variability is to test the hypothesis of a non-variable source with a reduced χ_r^2 test, which tries to fit a linear function to the light curve.

Table 5.6: Effelsberg observing log. Shown is the mean flux density, $< I >$, the number of scans, N, the modulation index, m, and the reduced χ^2_r from a linear fit (see text for details).

Source	$< I >$ [Jy]	N	m [%]	χ^2_r
0604+728	0.635 ± 0.010	1		
0615+820 ^{a,b}	0.773 ± 0.003	35	0.42	0.08
0716+714 ^{b}	0.747 ± 0.018	31	2.38	2.25
0718+793	0.843 ± 0.013	1		
0836+710 ^{a,b}	2.500 ± 0.008	45	0.33	0.05
0917+624	1.531 ± 0.012	4	0.79	0.28
0951+699 ^{a}	3.367 ± 0.005	4	0.14	0.01
0954+658	0.421 ± 0.006	1		
1928+738	4.147 ± 0.016	3	0.38	0.06
3C 196	4.360 ± 0.042	4	0.95	0.41
3C 286 ^{a}	7.521 ± 0.074	11	0.98	0.42
3C 295	6.593 ± 0.056	8	0.85	0.31
3C 48	5.537 ± 0.019	2	0.34	0.05
3C 84	19.999 ± 0.101	2	0.51	0.11

a: single-dish calibrators. b: VLBI sources.

3C 286 was used as the main flux density calibrator and 0836+710 as a secondary calibrator, which was observed around each 0716+714 scan. 0615+820 was also observed regularly as a secondary calibrator and and with VLBI and is known not to be variable at least over short time periods (Kraus 1997). If one compares the modulation indices and the χ^2_r of 0836+71, 0615+82 and 0716+714 it is obvious that 0716+714 was variable during the observations. A χ^2_r of 2.252 with 31 degrees of freedom means that the probability that the flux density of 0716+714 was constant is only 0.016 %, which is very unlikely. The same is true for the polarization. In Table 5.7 we show a summary of the linear polarization properties of 0716+714 and the polarization calibrators.

Table 5.7: Linear polarization as observed by Effelsberg. <> indicate mean values.

Source	$< P >$ [mJy]	$< I/P >$ [%]	m_P [%]	χ^2_r	$< \chi >$ [°]	χ^2_r
0615+82	1.8 ± 0.1	0.2 ± 0.1	0.00	1.16	71.9 ± 48.1	35.7
0716+71	19.9 ± 3.3	2.7 ± 0.4	9.26	15.39	18.8 ± 4.6	24.2
0836+71	160.0 ± 1.1	6.4 ± 0.1	0.00	0.05	106.3 ± 0.3	0.2
0951+69	1.4 ± 1.4	0.1 ± 0.1	11.60	1.29	111.1 ± 25.5	4.9
3C286	823.3 ± 12.8	11.0 ± 0.3	0.78	0.27	33.0 ± 0.2	0.2

Again 0716+714 is the only source that showed significant variability. The χ^2-test for 0615+820 and 0951+699 suggests that the sources show polarization variablity, but since they are nearly unpolarized this is due only to noise. The total intensity, linear polarization and EVPA light curves for 0716+714 and 0836+710 are presented in Figure 5.11. Labels of the absolute flux density values are given at the left ordinate and at the right ordinate the relative numbers to the overall mean are shown. Obviously, 0836+710 did not vary during the
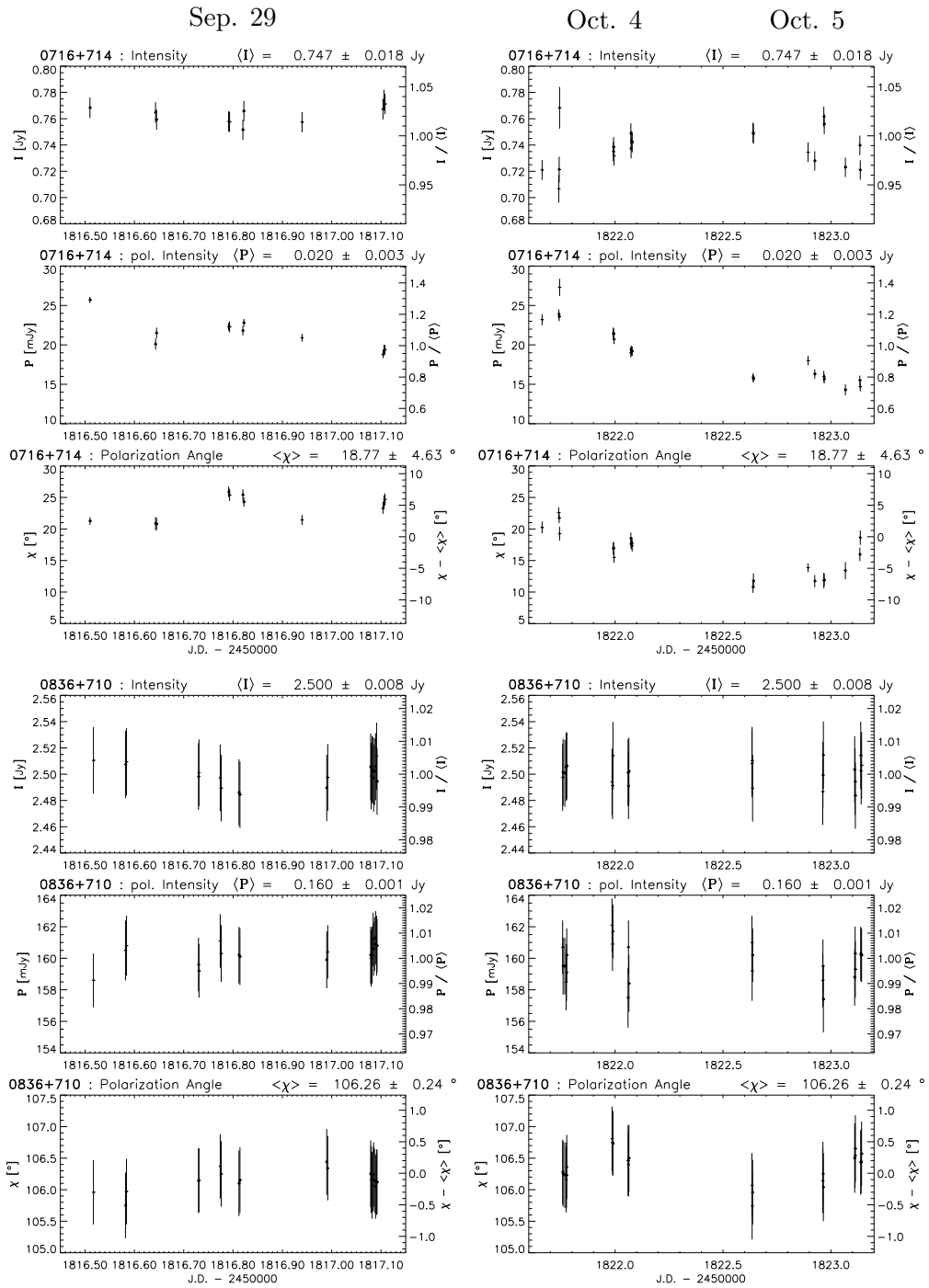
Figure 5.11: Total intensity (top), linear polarization (middle) and EVPA light curves of 0716+714 and 0836+710 from the Effelsberg antenna at 5 GHz. The left panels contain the data from September 29 and the right one from October 4 to 5. The left y-axis shows absolute flux density values and the right y-axis relative variations to the mean value that is given in on top of each panel.

observation, whereas 0716+714 shows up to 10 % variations in total intensity and about 40 % in linear polarization during the week of observations. The error bars are derived from the scattering of the calibrator measurements.

5.2.4 Origin of Variablity

A simple comparison of the average flux density measurements from Effelsberg and the integrated flux densities of the core and the jet region at the three epochs, reveals that all the variablity originates from the VLBI core component (see Table 5.8). The mean difference between the total flux density in the VLBI maps and the single dish flux density is (183.4 ± 3.1) mJy, corresponding to about 24.5 % less flux density in the VLBI images. This is plausible, since the arcsecond-scale structure of 0716+714 shows two lobes and surrounding halo like structure with a diameter of 10 arcsec (Antonucci et al. 1986) that is inside the Effelsberg beam, but not seen on VLBI scales. The absolute values of the core variability are, within the errors, similar to those of Effelsberg. We observe a decrease of 21 mJy (~ 3 %)with VLBI and 27.5 mJy (~ 5 %) with Effelsberg between epoch one and two and a constant flux density level between epoch two and three. This also means that we over estimated the flux density errors in our VLBI images and that the amplitude corrections derived from the self-calibration were indeed corrected and improved the accuracy flux density values.

Table 5.8: VLBI results in comparison with the single dish measurements from Effelsberg. The total linear polarization values of the VLBI images were calculated from the vector sum of the core and the jet polarization vectors.

Instrument	Part	I [mJy]	P [mJy]	χ [°]
		A2: 29 Sep 2000		
	Core	520.3 ± 26.9	12.1 ± 1.3	49.4 ± 4.1
VLBI	Jet	56.0 ± 4.7	7.4 ± 0.8	-10.8 ± 5.6
	Total	576.3 ± 31.6	17.0 ± 2.6	27.3 ± 6.0
Eb		763.2 ± 6.9	21.4 ± 2.6	23.4 ± 2.1
		A4: 4 Oct 2000		
	Core	499.3 ± 26.1	11.8 ± 1.3	40.7 ± 4.0
VLBI	Jet	54.8 ± 6.3	7.3 ± 0.8	-11.2 ± 7.8
	Total	554.1 ± 32.4	17.3 ± 2.7	21.3 ± 4.8
Eb		735.7 ± 16.2	21.6 ± 2.6	18.6 ± 2.2
		A5: 5 Oct 2000		
	Core	503.9 ± 25.4	6.5 ± 1.1	52.7 ± 5.2
VLBI	Jet	54.7 ± 6.0	7.5 ± 0.8	-9.5 ± 7.4
	Total	558.6 ± 31.4	12.0 ± 2.3	19.1 ± 5.3
Eb		740.2 ± 14.6	15.7 ± 1.1	13.3 ± 2.5

The variablity of the polarization flux density is anti-correlated to the total intensity variation. It shows nearly no variation between the first two epochs and a decrease of 5.3 mJy in the VLBI images and 5.9 mJy with Effelsberg

between epoch two and three, which corresponds to 40 % decrease of the core polarization flux density.

Only (4.2 ± 0.3) mJy of linear polarization was missed in the VLBI maps in comparison to ~ 180 mJy missing in total intensity. This yields an average fractional polarization for the large-scale structure of only 2.3 %, which would small compared to up to 40 % linear polarization found with the VLA at 1.4 GHz in the lobe like structure (Saikia et al. 1987). However, the VLA image shows a variety of EVPA orientations and the discrepancy is most likely due to in-beam depolarization at Effelsberg, so that polarization vectors at opposite position angles cancel. The missing polarization flux density also causes a difference between the EVPA measured from the VLBI images and at Effelsberg ranging from $2.7°$ to $5.8°$, but a look at the absolute differences between the epochs reveals that also the VLBI-core EVPA rotated simultaneously with the EVPA of the Effelsberg data.

Unfortunately, the time sampling of the Effelsberg light curve was not dense enough to measure reliable intraday variability for most of the time, but on Oct. 4 the light curve showed a significant decrease in polarization from (24.5 ± 1.7) mJy between 03^{00} UT and 07^{00} UT to (20.1 ± 1.1) mJy between 14^{00} UT and 18^{00} UT. In the same time the polarization vector rotated by $(4 \pm 2)°$. To check whether these polarization IDV can be found in the VLBI data, the corresponding time intervals were split from the data and imaged separately. The resulting maps show a decrease of the linear polarization in the core from (13.5 ± 1.4) mJy to (9.5 ± 1.0) mJy (Figure 5.12 and Table 5.9). Unfortunately, the inaccuracy of the core EVPA measurements in the VLBI images is to large to detected the rotation of the EVPA. But, given the very good agreement between the variation from hours to days between the VLBI-core and the single-dish measurements from Effelsberg, there is no doubt that the IDV in 0716+714 is coming from the VLBI core.

Table 5.9: Linear polarization variability from two time intervals of VLBI data (October 4th) in comparison with the single dish measurements from Effelsberg.

UT [h]	P_{VLBI} [mJy]	P_{Eb} [mJy]	χ_{VLBI} [°]	χ_{Eb} [°]
03–07	24.5 ± 1.7	13.5 ± 1.4	21.0 ± 2.3	40.8 ± 4.2
14–18	20.1 ± 1.1	9.5 ± 1.0	17.2 ± 1.8	43.0 ± 5.1

The simultaneous variation of the polarization angle with the polarized intensity suggests that the variations might be a result of the sum of the polarization of more than one compact subcomponent on scales smaller than the beam size. The large slope of the polarization angle over the core region seen with the higher resolution from the VSOP data (see Section 5.2.2) supports the idea that the core component itself is a composite of several subcomponents. The existent of such compact components in the core, was also introduced by Rickett (2001b) to explain polarization IDV via refractive interstellar scattering (RISS). In this scenario at least three components of a few μas have to be concentrated in an area smaller than $100 \, \mu$as. The independent scintillation of each component can then cause variability of the polarization intensity and a

rotation of the polarization vector by superposition of the components within the beam of the telescope or interferometer.
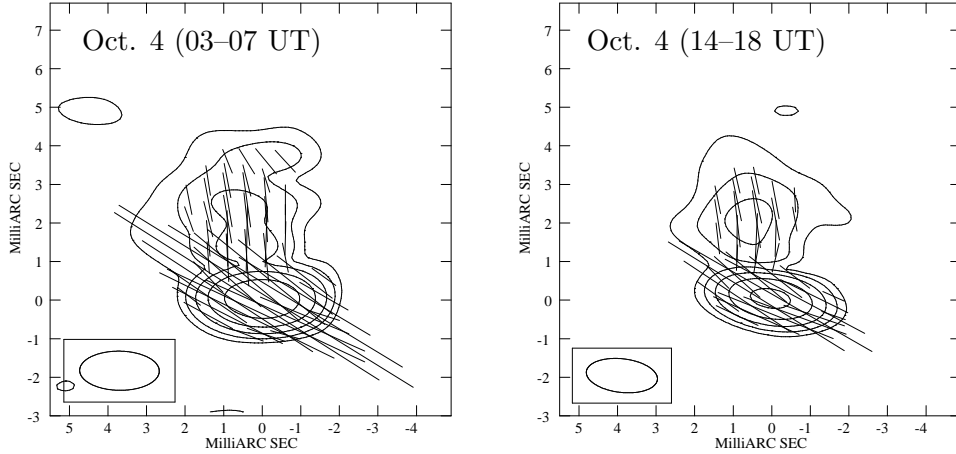
Figure 5.12: Linear polarization contour images of the split Oct. 4 VLBI data with polarization E-vectors superimposed. At a resolution of about $2\,\text{mas} \times 1\,\text{mas}$ at $\sim 85°$ and the contours start at $0.5\,\text{mJy/beam}$, increasing in steps of 2.

5.2.5 Brightness Temperature

Assuming that the variability has an intrinsic origin restricts the emitting region to be extremely compact, which then results in very high brightness temperatures exceeding the inverse-Compton limit of $10^{12}\,\text{K}$ (Kellermann & Pauliny-Toth 1969). The short time-scales observed imply linear dimensions of

$$l = \frac{c\,\delta\,\Delta t}{1 + z},\qquad(5.1)$$

where δ is the Doppler factor. Assuming a redshift of 0.3, the size of the emission region that is responsible for the variability is around $8 \cdot 10^{12}\,\text{m}$ or $\sim 55\,\text{A.U.}$, which is slightly larger than our solar system. The brightness temperature for a stationary source is given by Equation 1.12 (p. 12). To calculate the variability time-scale we use:

$$t = \frac{<S>}{\Delta S}\,\frac{\Delta t}{(1 + z)},\qquad(5.2)$$

where $<S>$ (in Jy) is the mean flux density, ΔS (in Jy) is the standard deviation and Δt (in yr) is duration of the variation (Wagner et al. 1996). Calculating the corresponding T_b of the linear polarization decrease between October 4th and 5th results in $T_\text{b} = 3 \times 10^{15}\,\text{K}$ and the drop of $4\,\text{mJy}$ during $10\,\text{h}$ on October 4th yields $T_\text{b} = 10^{16}\,\text{K}$. Since, $T_\text{b} \propto \delta^3$ a Doppler factor of 14 to 22 is needed to reduce the values to the inverse-Compton limit.

Readhead (1994) found an even lower limit to the brightness temperature from equipartition arguments. He states that if there is no large departure minimum energy and equipartition the limiting brightness temperature is $5 \times$

10^{10} K to 10^{11} K. This results in Doppler factors of up to 60 for the variability found in 0716+714. However, only a small departure from equipartition, e.g. by a factor of two, would bring the Doppler factor back to 30, which is within the range of possible Doppler factors derived from the kinematics in the previous chapter.

5.2.6   Jet Inclination and Lorentz Factor

Simulations of relativistic hydrodynamic jets show that shocks are likely to occur in highly supersonic flows. Those provide a natural way to enhance locally the magnetic field and relativistic electron density, producing knots of emission such as seen in VLBI images (e.g., Gomez et al. 1997, and references therein). Assuming that the knots in the jet are shocks travelling down the jet, we can use the observed degree of polarization of such a jet component to set limits on the angle to the line of sight and on the jet Lorentz factor (Cawthorne & Wardle 1988). The shock model, used here, is based on the scenario that Hughes et al. (1985) used to describe the polarization variability in BL Lac. In that model, the magnetic field of the jet is compressed by a propagating shock so that the initially random field is ordered in a plane transverse to the jet axis. They derive for the degree of linear polarization, m, of synchrotron radiation from a partially compressed field

$$
\begin{aligned}
m &\approx m_0 \, \frac{(1-k^2)\cos^2\epsilon}{2-(1-k^2)\cos^2\epsilon}, \text{ with} \\
m_0 &= \frac{s+1}{s+7/3},
\end{aligned}
\tag{5.3}
$$

where m_0 is the degree of polarization of synchrotron emission in a uniform magnetic field, s is the index of the power-law of the electron energy distribution, k the amount of compression, defined as a unit length compressed to a length k, and ϵ is the angle between the line of sight and the shock plane in the frame of the jet. With this we can constrain k and ϵ using the measured degree of polarization in the jet.

A modelfit to the linear polarization image with JMFIT in AIPS reveals that the peak of the linear polarization in the jet corresponds to component C7 (see Figure 4.3), which moves with a speed of $(6.9 \pm 0.2)\,c$. Integrating the flux density in the total intensity and in the polarization image over a region of 1.5 times the beam width around the component centre ($r = 2.7 \pm 0.2\,\text{mas}$) yields a fractional polarization, m, of about $(24 \pm 4)\,\%$. For a spectrum of $\alpha_{5/15\,\text{GHz}} = -0.7$ (compare Fig. 4.8) and therewith $s \approx 2.5$, the nominal degree of polarization of synchrotron emission in a uniform magnetic field is $m_0 \approx 0.72$.

We can solve Equation 5.3 in two cases. First, if the jet is oriented at the viewing angle that maximizes the apparent superluminal motion, then $\epsilon = 0$ and k gives an upper limit on the amount of compression. We find:

$$k_{\min} = \sqrt{\frac{1 - \frac{m}{m_0}}{1 + \frac{m}{m_0}}} = 0.71 \pm 0.04.$$

Second, if we assume a maximum of compression ($k \ll 1$), then ϵ corresponds to the maximum angle between the shock plane and the line of sight, which yields:

$$\epsilon_{\max} = \cos^{-1} \sqrt{\frac{2}{\frac{m_0}{m} + 1}} = \pm 45 \pm 4°$$

We can now relate these limits to the apparent speed of the jet and constrain the inclination of the jet, θ, and the jet Lorentz factor, γ (Cawthorne & Wardle 1988). If we assume that the shock travels with the same velocity as the emitting material then:

$$\cos \theta = \frac{\sin \epsilon + \beta}{1 + \beta \sin \epsilon}. \tag{5.4}$$

Combining this with the formula for the apparent speed (Equation 4.3, p. 32) results in:

$$\beta_{\mathrm{app}} = \gamma \beta \cos \epsilon \quad , \text{or} \tag{5.5}$$

$$\gamma = \sqrt{\left(\frac{\beta_{\mathrm{app}}}{\cos \epsilon}\right)^2 + 1}. \tag{5.6}$$

Taking the measured apparent speed of $(6.9 \pm 0.2)\,c$ of component C7 yields a jet Lorentz factor of ~ 7 and an angle to the line of sight of $\sim 8°$, if $k = k_{\min}$ and $\epsilon = 0$, which can already be exclude, because of the limits derived from the kinematical analysis. If $k \ll 1$ and $\epsilon = \pm 45°$, then $\gamma \approx 10$ and $\theta \approx 2.5°$ or $14°$ (depending on the sign of ϵ), but the larger viewing angle can again be excluded from the kinematics. This jet parameters show the same trend as the parameters ($\gamma > 16$ and $\theta < 2°$) derived from the kinematics. The shock scenario also favours the small-angle solution, where we have higher jet Lorentz factors and smaller viewing angles than those derived by maximization of $\beta_{\mathrm{app}} = \frac{\beta \sin \theta}{1 - \beta \cos \theta}$. For $\gamma \approx 10$ and $\theta \approx 2.5°$ the corresponding Doppler factor is about 17.

5.3 Conclusions

To reveal the origin of the rapid IDV in 0716+714, a multi-epoch VSOP experiment was done in September and October 2000. The ground array and the VSOP images show a bright core and a jet oriented to the north. The linear polarization images indicate that the jet magnetic field is perpendicular to the jet axis. Relative to the jet axis, the electric vector position angles in the core

are misaligned by around 60°. This can be due either to the core being optically thick or the jet is curved in the inner core region. Jet curvature is supported by recent high resolution 3 mm VLBI observations that show the inner jet structure ($r < 0.1$ mas) at a similar position angle as the EVPA in the core at 6 cm wavelength.

Simultaneous flux-density measurements with the 100 m Effelsberg telescope during the VSOP observations revealed variability in total intensity ($\sim 5\%$) and in linear polarization (up to $\sim 40\%$) accompanied by a rotation of the polarization angle by several degrees. The analysis of the VLBI data proves that the variations are caused by the core component of 0716+714. The ground array and the VSOP maps show a similar decrease of the flux densities in total intensity and linear polarization of the core component as the single dish measurements. The EVPA of the VLBI-core rotates by the same amount as in the single dish measurements. Over the period of the observations no rapid variability in the jet was observed and we can not confirm the variability out side the core found by Gabuzda et al. (2000a).

The simultaneous variation of the polarization angle with the polarized intensity in the core suggests that the variations might be the result of the sum of the polarization of more than one compact sub-component on scales smaller than the beam size. These sub-components already become visible in the higher resolution of the VSOP images. The linear polarization structure in the core region can be well fitted by two Gaussian components of about 0.1 mas diameter, which vary independently. Assuming that these variations are intrinsic to the source, we derive brightness temperature of $\sim 3 \times 10^{15}$ K to $\sim 10^{16}$ K and Doppler factors of > 20 are needed to reduce these values to the inverse-Compton limit. This numbers are in agreement with the observed speeds in the jet if the angle to the line of sight is very small ($\theta < 2°$).

However, also extrinsic effects could explain the observations. To explain the intraday polarization variability by interstellar scattering similar structures, of very small competing sub-components are proposed (Rickett 2001a,b). Anyhow, the small source sizes observed with VLBI already yielded brightness temperatures of $\sim 2 \times 10^{12}$ K and therewith exceed the inverse-Compton limit. This implies a Doppler factor of about 4 and, independent of the model we use to explain the variability, relativistic beaming seems to play a role. Unfortunately, the sub-components cannot be resolved with a sufficient dynamic range to study their individual behaviour to distinguish whether the variability is due to intrinsic variation of the source or whether it is introduced by the interstellar medium. A future detailed multi-frequency analysis of the sub-components in the core will help to solve this question.

To explain the enhanced degree of polarization in the superluminal jet we applied a simple shock model developed by Cawthorne & Wardle (1988) to our observations and found reasonable values for the jet Lorentz factor and the viewing angle. This supports the idea that the knots of bright emission in the jet are shocks travelling down the jet (Marscher & Gear 1985).

Chapter 6

Multi-Epoch & Multi-Frequency VLBI Observations of Cygnus A

In this chapter the physical properties of the core and the jet and the counter-jet in the inner region ($\sim 20\,\mathrm{pc}$) of the archetypical FR II radio galaxy Cygnus A are discussed. In terms of the unified scheme, this means, after the discussion of the jet in the BL Lac object S5 0716+714, that we now rotate the AGN by about $90°$. While in 0716+714 we looked nearly into the jet where the appearance of the jet is thought to be dominated by relativistic effects, the Cygnus A jet is seen nearly edge-on and enables us to study the internal jet physics from a different point of view.

This study is a continuation of the work started during my diploma thesis (Bach 2001) and aims to measure the jet speeds with improved accuracy and thereby better constrain the jet structure and source geometry. Further, we intend to probe the existence of a circum-nuclear absorber, which is proposed by the unified scheme to exist in narrow line radio galaxies, like Cygnus A, and that should block the emission from the broad line region. To achieve these goals we observed Cygnus A three times with the VLBA and Effelsberg at 5 GHz and 15 GHz in 2002 and 2003 and performed a first phase-referencing observation at 15 GHz and 22 GHz in 2003. We carried out, for the first time, VLBI observations at 86 GHz with the global 3 mm VLBI array and with the VLBA using the technique of fast frequency switching at 15 GHz, 43 GHz and 86 GHz developed by Middelberg et al. (2002) and Middelberg (2004). These observations are complemented by a multi-frequency data set at 15 GHz, 22 GHz and 43 GHz obtained with the VLBA and Effelsberg from 1996 and are additional ten epochs at 15 GHz from the VLBA 2 cm Survey between 1995 and 2003 (Kellermann et al. 2004, 1998; Zensus et al. 2002). A detailed observing log is given in Table 6.1

In Section 6.1 we will describe the observations and data reduction process. In Section 6.2 the results will be presented, analysed and discussed. The final conclusions are given in Section 6.3.

Table 6.1: Observation log. Listed are the observing epoch, frequency ν, total flux density $S_{\text{tot}}(\nu)$, beam size, beam position angle, peak flux density S_{peak}, σ the rms noise of the map and polarization mode. The page number at which the map of an epoch is first shown is given in the last column. Four of the 2 cm Survey maps are not shown, but the modelfits resulting are given in Figure 6.19 and Table 6.9.

Epoch	ν	S_{tot}	Beam	P.A.	S_{peak}	σ	Pol.	Page
	[GHz]	[Jy]	[mas × mas]	[°]	$[\frac{Jy}{beam}]$	$[\frac{mJy}{beam}]$		
1995.27 [1]	15.4	1.60	0.53 × 0.89	-7.9	0.56	0.54	LCP	90
1995.95 [1]	15.4	1.68	0.54 × 0.95	8.9	0.60	0.74	LCP	90
1996.38 [1]	15.4	1.42	0.56 × 0.91	-19.4	0.48	0.47	LCP	-
1996.73 [a]	15.4	1.71	0.30 × 0.61	-18.3	0.40	0.36	dual	79
1996.73 [a]	22.2	1.48	0.24 × 0.47	-16.1	0.36	0.82	dual	79
1996.73 [a]	43.2	1.01	0.23 × 0.27	3.6	0.40	1.90	dual	79
1996.82 [1]	15.4	1.18	0.62 × 0.97	3.2	0.48	0.27	LCP	-
1997.66 [1]	15.4	1.56	0.91 × 1.14	-10.3	0.82	0.39	LCP	90
1998.21 [1]	15.4	1.53	0.63 × 1.14	10.8	0.61	0.41	LCP	90
1999.38 [1]	15.4	1.70	0.43 × 0.80	-3.3	0.47	0.33	LCP	90
2001.17 [1]	15.4	1.53	0.49 × 0.97	-17.1	0.53	0.44	LCP	90
2001.97 [1]	15.4	1.42	0.54 × 1.01	-8.7	0.49	0.27	LCP	-
2002.03 [a]	4.9	0.89	0.92 × 1.54	-23.8	0.12	0.17	dual	81
2002.03 [a]	15.4	1.51	0.31 × 0.56	-21.3	0.28	0.12	dual	81
2002.51 [a]	4.9	0.91	0.87 × 1.56	-23.0	0.15	0.16	dual	81
2002.51 [a]	15.4	1.50	0.46 × 0.67	-14.4	0.39	0.17	dual	81
2002.88 [1]	15.4	1.38	0.65 × 1.11	-9.7	0.38	0.31	LCP	-
2003.04 [*]	15.4	1.27	0.46 × 0.73	-5.1	0.32	0.26	dual	73, 80
2003.04 [*]	22.2	1.27	0.31 × 0.51	10.4	0.34	0.45	dual	73, 80
2003.24 [a]	4.9	0.99	1.10 × 1.72	-20.1	0.21	0.14	dual	71
2003.24 [a]	15.4	1.38	0.25 × 0.52	-23.4	0.23	0.12	dual	81
2003.27	14.4	1.52	0.45 × 0.68	0.6	0.35	0.26	LCP	90
2003.27	43.1	0.75	0.16 × 0.26	-11.4	0.23	0.64	LCP	80
2003.27	86.2	0.41	0.32 × 0.36	88.4	0.33	1.89	LCP	75
2003.32 [b]	86.2	0.43	0.07 × 0.28	-23.0	0.33	5.35	LCP	76

Note: The array used was the VLBA, unless indicated by a footnote. Epochs in bold face denote own data. a: VLBA+Eb , b: Global VLBI array. $*$: phase-referencing.
References: (1): Kellermann et al. (1998), Zensus et al. (2002) & Kellermann et al. (2004)

6.1   Observations and Data Reduction

Most of our own observations were made in dual circular polarization, except
the two high frequency observations (2003.27 & 2003.32), and were correlated
in Socorro. The observation from the global 3 mm VLBI campaign (2003.32)
was correlated at the MKIV correlator in Bonn. Most of the data were re-
duced in the standard manner using NRAO's Astronomical Image Processing
System AIPS (see also Chapter 2). The imaging of the source employing phase
and amplitude self-calibration was done using the CLEAN (Högbom 1974) and
SELFCAL procedures in DIFMAP (Shepherd 1994). The self-calibration was
done in steps of several phase-calibrations followed by careful amplitude cal-
ibration. During the iteration process the solution interval of the amplitude
self-calibration was shortened from intervals as long as the whole observational
time down to minutes.

   To orient the reader, the most recent image of Cygnus A at 5 GHz from
2003.24 is shown in Figure 6.1. It shows the jet and the counter-jet up to
~ 50 mas from the core (1 mas ≈ 1.1 pc) separated by an emission gap of about
4 mas were we see no emission at 5 GHz. Since, some of the observations were
performed using non standard techniques the reduction of these epochs will be
explained in more detail now.
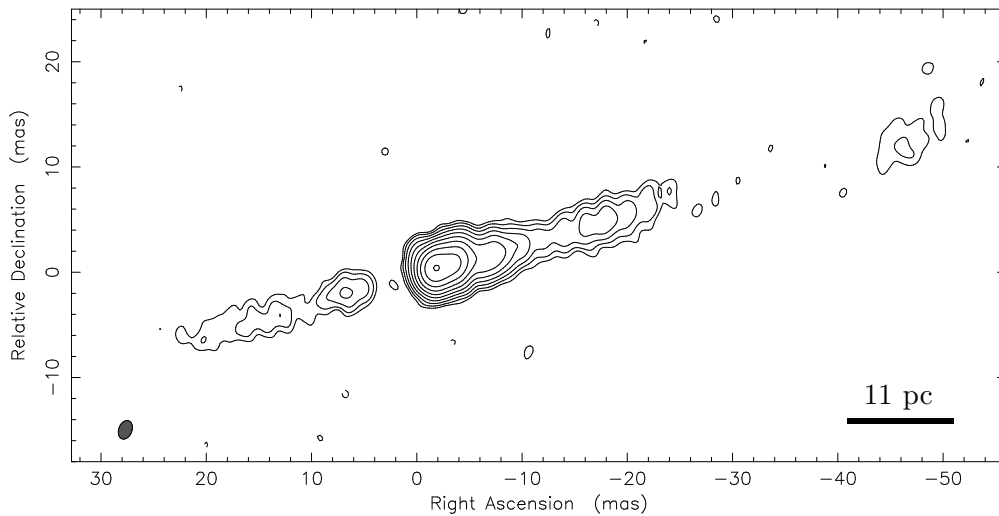
Figure 6.1: VLBI image of Cygnus A at 5 GHz (2003.24). The beam size, peak flux density
and rms noise are given Table 6.1. The lowest contours start at 0.45 mJy/beam and increasing
in steps of 2.

2003.04   In this epoch Cygnus A was observed at 15 GHz and 22 GHz using
phase-referencing. Phase-referencing VLBI allows one to measure the absolute
position of a source with respect to a calibrator source. Normally the absolute
position information is lost during the calibration process of VLBI data. The
aim of this observation was to start a phase-referencing monitoring to be able to
measure absolute motions in the jets and to determine the frequency-dependent
core shift in the jet. Here, we used the nearby quasar 2005+403 ($\sim 1.5°$ away)

to solve the phase errors which are left after the correlation at each station and applied the corrections to Cygnus A. Another Quasar, 2013+370, was used to check for possible frequency dependent position shifts in our calibrator.
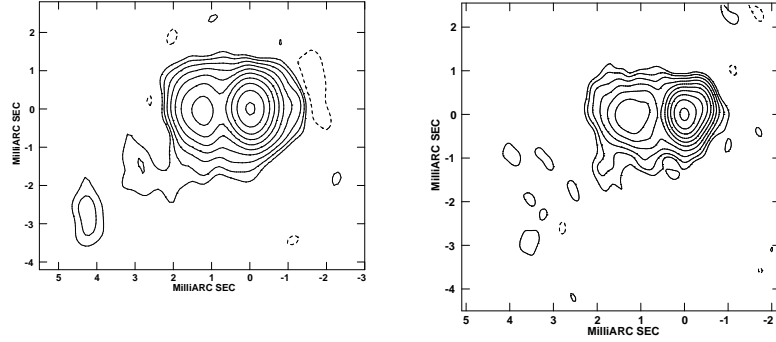
Figure 6.2: Contour images of the phase-referencing calibrator 2005+403. **Left:** At 15 GHz with a beam size of 0.8 mas × 0.5 mas at 3° and a peak flux density of 1.4 Jy/beam. Contours start at 2.5 mJy/beam and increase in steps of 2. **Right:** At 22 GHz with a beam size of 0.6 mas × 0.4 mas at 6° and a peak flux density of 1.4 Jy/beam. Contours start at 2 mJy/beam.
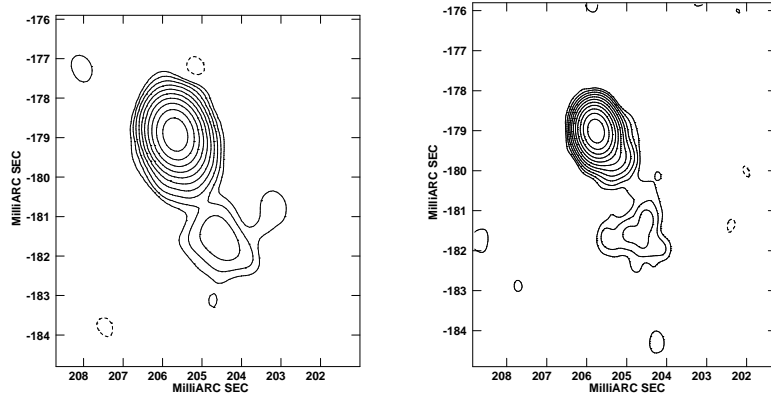
Figure 6.3: Contour images of the phase-referenced data of the second calibrator 2013+370. Note that the relative declination and right ascension shows an offset of about 200 mas to the position where the sources were catalogued. **Left:** At 15 GHz at a beam size 0.9 mas × 0.6 mas at 4° and a peak flux density of 3.1 Jy/beam. Contours start at 2.5 mJy/beam and increase in steps of 2. **Right:** At 22 GHz at a beam size of 0.6 mas × 0.4 mas at -2° and a peak flux density of 3.1 Jy/beam. Contours start at 2 mJy/beam.

The images of the calibrators are shown in Figure 6.2 & 6.3. Note that for 2013+370 in Figure 6.3 the relative declination and right ascension shows an offset of about 200 mas to the catalogued position of the source. A weaker source would have been hard to find, with such a large position off set, but due to its high total flux density of about 6 Jy, 2013+370 could be found in a 500 mas × 500 mas map. The coordinates of the sources from the catalog and those we derived from our phase-referencing are shown in Table 6.2.

The complicated double structure of the main calibrator 2005+403, with two peaks at comparable intensity can introduce shifts if one uses a simple point-source model during the fringe fitting. Therefore, a second fringe fit using a

Table 6.2: J2000 coordinates of the phase-referencing source. Given is the position of the International Celestial Reference Frame (ICRF) catalog (Ma et al. 1998) and the phase-referenced position to 2005+403 at 15 GHz.

	ICRF		phase-ref.	
Source	R.A.	Dec.	R.A.	Dec.
2005+403	20:07:44.9449	40:29:48.604	–	–
2013+370	20:15:28.7126	37:10:59.694	20:15:28.7298	37:10:59.515
Cygnus A	19:59:28.3567	40:44:02.097	19:59:28.3570	40:44:02.098

proper source model from the hybrid mapping in DIFMAP was done. With this we could successfully phase-reference Cygnus A to 2005+403 and were able to restore 90 % of the flux density in the phase-referenced image compared to the self-calibrated image. The phase-referenced images are shown in Figure 6.4.
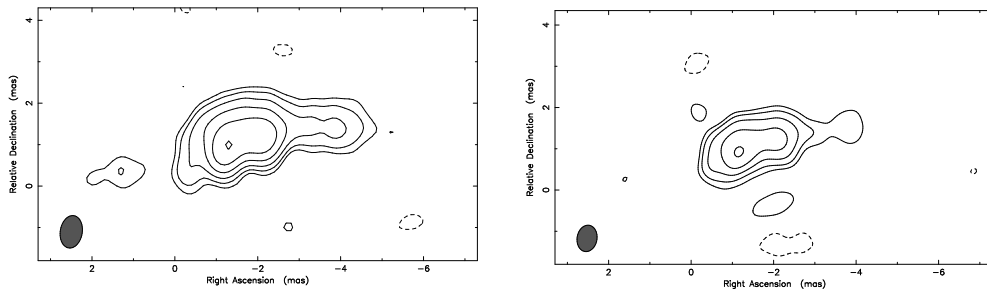
Figure 6.4: Phase-referenced images of Cygnus A. **Left:** At 15 GHz with a beam of 0.8 mas × 0.5 mas at −9° and a peak flux density of 0.33 Jy/beam. Contours start at 10 mJy/beam and increase in steps of 2. **Right:** At 22 GHz with a beam of 0.6 mas × 0.5 mas at −9°. The peak is at 0.31 Jy/beam and the contours start at 18 mJy/beam. For comparison the hybrid maps of these data are shown in Figure 6.10

In Table 6.3 we show the obtained position shifts between 15 GHz and 22 GHz. The positions were measured using the task MAXFIT in AIPS. The typical accuracy of a single phase-referencing experiment is about 50 μas (Fomalont 1999) and we will assume that this error also applies to our data.

Assuming that there is no frequency-dependent position shift in 2005+403 revealed comparable position shifts for 2013+370 and Cygnus A. Given that the position shifts point nearly into the same direction and the shift for 2013+370 is nearly perpendicular to its jet position angle it seems likely that a large fraction of the shift is caused by the calibrator 2005+403. Assuming that the position of 2013+370 does not change with frequency yields a shift of 80 μas along the jet for Cygnus A and a shift of 120 μas at P.A. $\sim$ 45° for 2005+403. Although 2005+403 extends in east west direction an elongation of the brightest component to P.A. $\sim$ 45° can be seen in the 22 GHz map (Figure 6.2) and a position shift in this direction might be possible. Assuming that the position of Cygnus A does not change with frequency yields again a shift for 2013+370, which can not be relate to its source structure and therefore the most likely scenario would be that 2013+370 is stationary, but given that the shift in Cygnus A is not significantly larger than the typical error of 50 μas we cannot

Table 6.3: Position shifts between 15 GHz and 22 GHz derived from the phase-referencing. In each block we assume that one of the sources does not show a frequency dependent position shift. First 2005+403, then 2013+370 and at the end Cygnus A.

Source	Δx [mas]	Δy [mas]	Δr [mas]	P.A. [°]
2005+403	−	−	−	−
2013+370	−0.08	+0.09	0.12	−44.5
Cyg A	−0.16	+0.11	0.19	−56.5
2005+403	+0.08	−0.09	0.12	+44.5
2013+370	−	−	−	−
Cyg A	−0.08	+0.02	0.08	−74.1
2005+403	+0.16	−0.11	0.19	+56.3
2013+370	+0.08	−0.02	0.08	+74.1
Cyg A	−	−	−	−

measure a reliable core-shift for Cygnus A. The actual alignment of the maps was done using Gaussian modelfit components (see Sec. 6.1.1). However, together with future phase-referencing epochs, these data will be very useful to study the absolute motions in the jets.

2003.27   For this high frequency epoch (15 GHz, 43 GHz & 86 GHz) the fast frequency switching technique, a new calibration strategy for high frequency VLBI (Middelberg et al. 2002), was used to measure the core-shift in Cygnus A. During the observations one cycles, within the coherence time of the higher frequency, between a lower reference frequency, ν_r, and a higher target frequency, ν_t. With this, the phases of the data at ν_t can be calibrated using scaled-up phase solutions from self-calibration at ν_r. In principle one gets two maps with phase-referenced positions, which allow one to measure the core-shift between these frequencies. The data reduction is basically done in the standard manner in Aips, but presently the scaling of the phases has to be done in a Python program written by Enno Middelberg outside Aips. A detailed description of the technique and its use is given by Middelberg (2004) and should soon be available as a VLBA Scientific Memo[1]. Although, the frequencies used are high there is still a contribution to the phases from the ionosphere, which has to be corrected. These corrections were determined using the task TECOR, which uses maps of the ionospheric total electron content derived from GPS data to calculate the phase and delay corrections. Unfortunately, the errors in these maps are too large and the accuracy of the scaled phases is not high enough to get a real phase-referenced map at ν_t and a measurement of the core-shift is not possible. But the scaled-up phases increase the coherence time at 86 GHz to about 30 minutes and the data could be successfully fringe fitted at 86 GHz on Cygnus A. Therewith, we were able to make the first 3 mm VLBI image of the core of Cygnus (see Figure 6.5).

---

[1]http://www.aoc.nrao.edu/vlba/html/MEMOS/scimemos.html
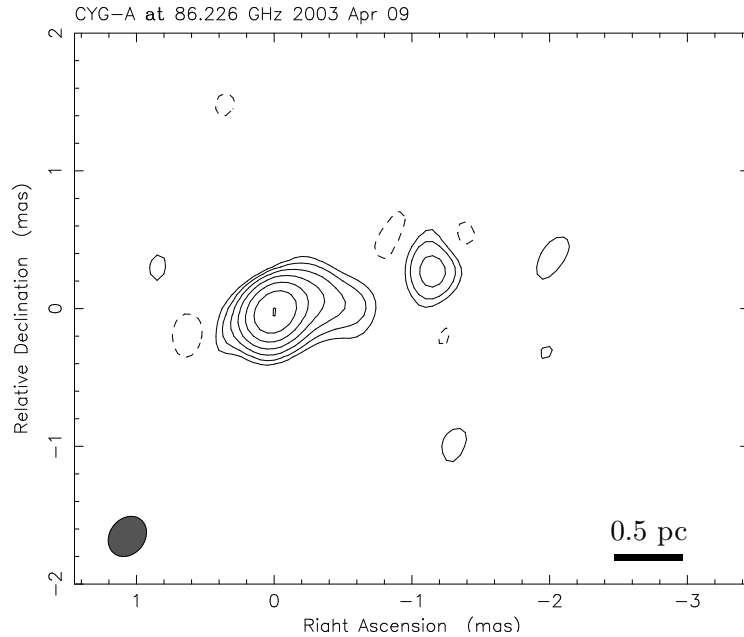
Figure 6.5: First image of Cygnus A at 3 mm wavelength at a resolution of 0.31 mas × 0.25 mas at −38° and a peak flux density of 0.29 Jy/beam. Contours start at 4.5 mJy/beam and increasing in steps of 2. The dynamic range dynamic range (D = peak/rms) is about 150.

2003.32 Only 18 days after the fast-frequency-switching observation, Cygnus A was observed with the global 3 mm array. The data were correlated at the MKIV correlator in Bonn (Alef & Graham 2002). After the correlation the phase offsets between the intermediate frequencies (IF) are removed using FOURFIT from the Haystack analysis package. The results were written to a table attached to the (u, v) data file and were applied to the data with the task BLAPP in AIPS. Because, the data format of the MKIV correlator is different from the VLBA format, the data had to be loaded into AIPS using the task MK4IN, instead of FITLD. The further phase and amplitude calibration steps were done in the standard manner in AIPS.

Unfortunately, Cygnus A was detected only on a few baselines and the resulting image shows only the central compact component (Figure 6.6). The image is obtained by model-fitting the (u, v) data using a delta component and an elliptical Gaussian component to fit the extended emission. The best fit was obtained by a 120 mJy delta component surrounded by an ∼ 340 mJy elliptical Gaussian component (0.17 mas × 0.16 mas at −78°). The direction of the elliptical component is coincident with the jet direction and might indicate that also some of the underlying structure is present in the visibilities.

Data from other Observers Additional Cygnus A data at 15 GHz were provided by the VLBA 2 cm Survey team[2]. The data from were provided as amplitude calibrated and fringe fitted (u, v) FITS files together with the images from the automatic mapping procedure that is used by the survey (Kellermann et al.

---

[2]http://www.cv.nrao.edu/2cmsurvey/
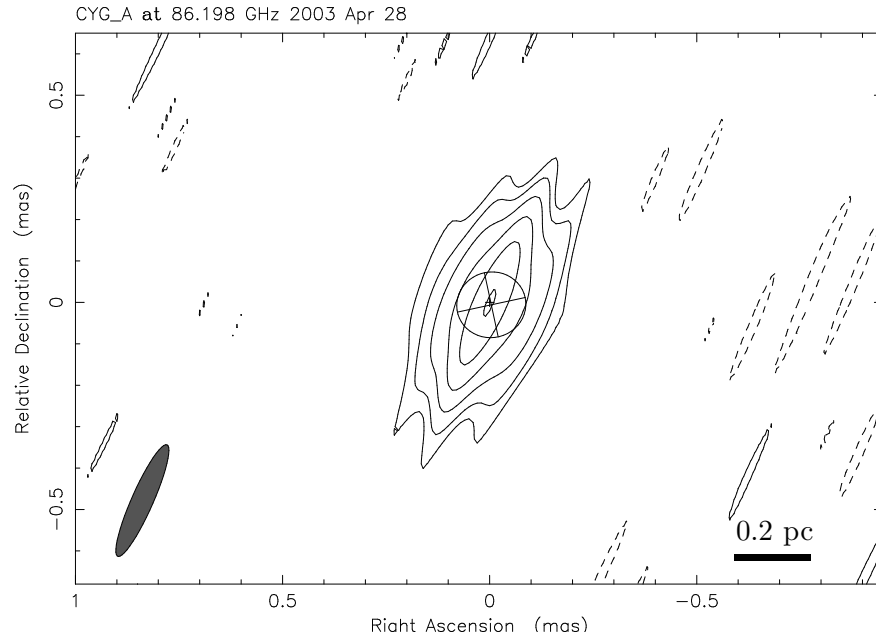
Figure 6.6: Shown is an image of Cygnus A at 3 mm wavelength obtained with the global 3mm VLBI array (2003.32). The image is obtained by model-fitting the (u, v) data using a delta component and an elliptical Gaussian component to fit the extended emission. The image and modelfit parameters are given in Table 6.1 and in the text.

1998). Where necessary, the data were recalibrated and reimaged in DIFMAP. In the most cases, however, the automatically self-calibrated (u, v) data could be used for the model-fitting procedure.

6.1.1   Model Fits

To measure proper motion in the jet and the counter-jet of Cygnus A and to align the images at different frequencies, circular Gaussian model components were fitted to the visibility data using the MODELFIT task in DIFMAP. The parameters of these model fits are given in Table 6.9 (p. 101). Conservatively, 1σ errors of 10 % in the flux density arising from the uncertainties of the amplitude calibration and from the formal errors of the model fits are assumed. An estimate for the position error is given by $\Delta r = \frac{\sigma \cdot \Theta}{2 S_{\text{peak}}}$ (Fomalont 1989), where σ is the residual noise of the map after the subtraction of the model, Θ is the width of the component, and S_{peak} is the peak flux density. This formula tends to underestimate the error if the peak flux density is very high or the width of the component is small. In the case of a small width we used the beam size, instead. An example comparing the result of the model-fitting with the intensity profile of the CLEAN map is given in Figure 6.7. It demonstrates that the components represent true structures in the jet.
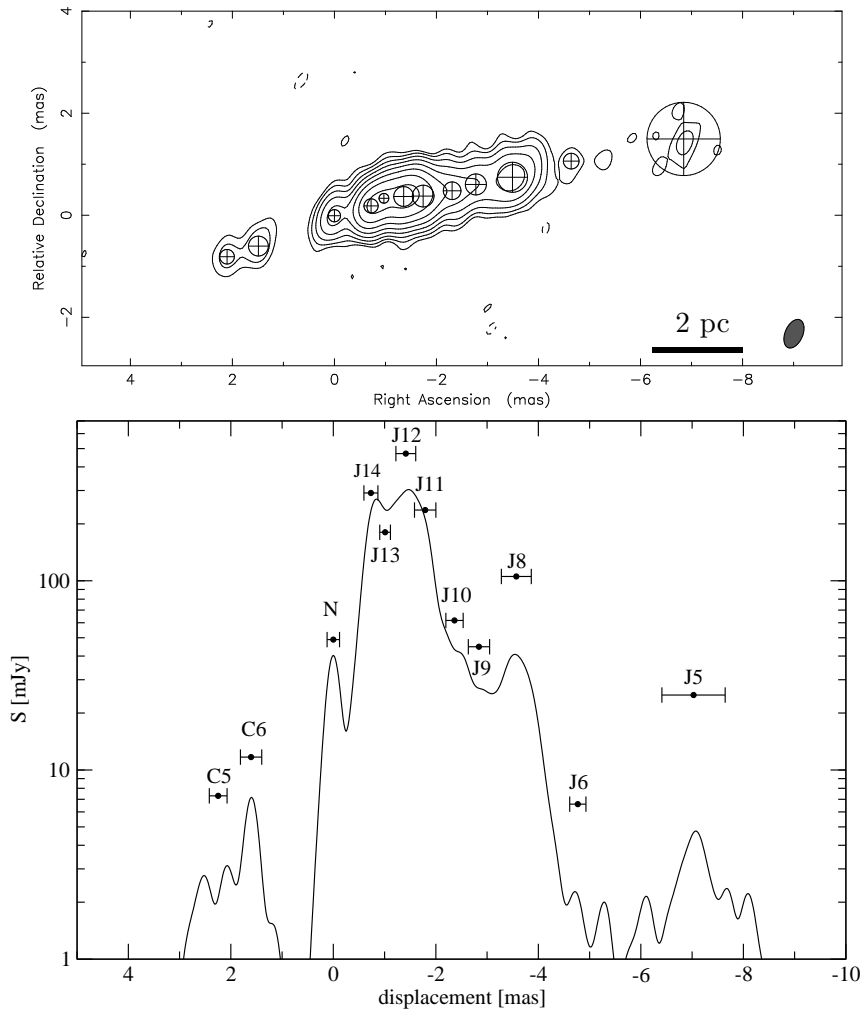
Figure 6.7: As an example we show the parameterization of the jets in Cygnus A using Gaussian model components of the January 2002 observation at 15 GHz (epoch 2002.03). **Top:** Shown are total intensity contours with overlaid modelfit components. The size of each component corresponds to the FWHM in milliarcseconds. **Bottom:** The position, FWHM and flux density of each component is displayed together with a total intensity profile along the jets of Cygnus A. The labels represent the identification from the kinematical analysis in Section 6.2.4. Most of the components are located on top of a peak in the profile and therefore represent real structures in the jet.

6.1.2 Polarization Calibration

The procedure of the D-term and EVPA calibration was done in a similar way as described in Section 5.1.1. No linear polarization could be detected at any of the frequencies, except the 2002.51 epoch at 15 GHz. However, the linear polarization in this epoch was found to be very weak (0.44 %). The resulting image is shown in Figure 6.8. Middelberg (2004) recently analysed the polarization properties of double sided parsec-scale radio sources including this Cygnus A epoch. In most of the sources no linear polarization could be found and we refer to his thesis about the details of the calibration and the discussion of the results.
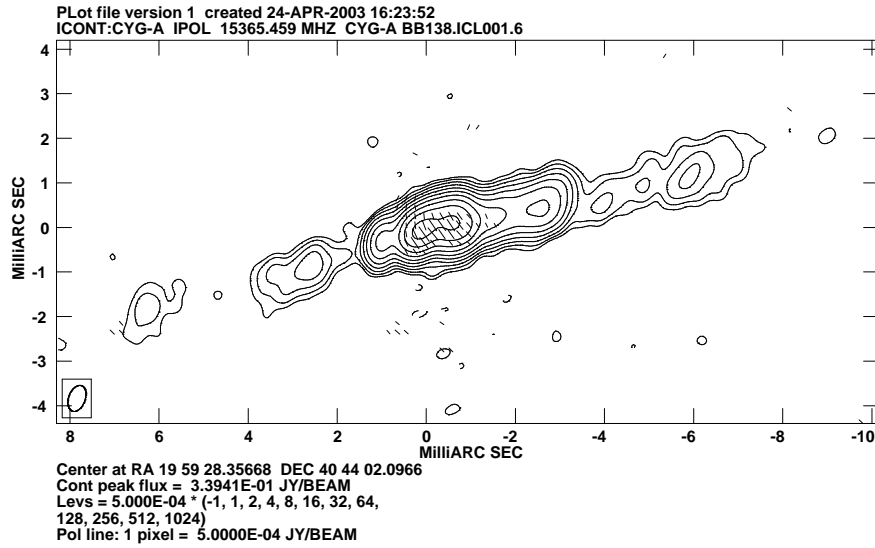
Figure 6.8: 15 GHz total intensity contours with overlaid linear polarization E-vectors (1 mas = 10 mJy/beam) from the 2002.51 epoch. The image parameters are given in Table 6.1.

6.2 Results and Discussion

In this section the maps of Cygnus A at the different frequencies and epochs will be analysed and discussed. First we discuss the alignment of the images, which is different from previous studies (Bach et al. 2004, 2002; Carilli et al. 1994; Krichbaum et al. 1998). This will be followed by a discussion of the multi-frequency epochs. Finally the 16 epochs at 15 GHz will be used for a detailed study of the motion in the jets of Cygnus A.

6.2.1 Identification of Jet Components

To investigate the spectral properties and the kinematics of Cygnus A on parsec scales we needed to align the images at different frequencies and epochs with each other. Since, in the usual phase self-calibration the absolute position information is lost the cross-identification was done using the individual modelfit components along the jets. The identification was done using their relative

separation from each other, their flux density and size. Although the phase-referenced observations from 2003 gave us no obvious core shift we can use the non detection of a shift to constrain the shift between 15 GHz and 22 GHz to be lower than ≤ 0.2 mas. Between 22 GHz and 43 GHz Krichbaum et al. (1998) measured a shift of $\sim 75\,\mu$as that we used to further constrain our alignment. The alignment was done using all multi-frequency epochs between 1996 and 2003 and from Figure 6.9 to 6.11, we show the results of this procedure.
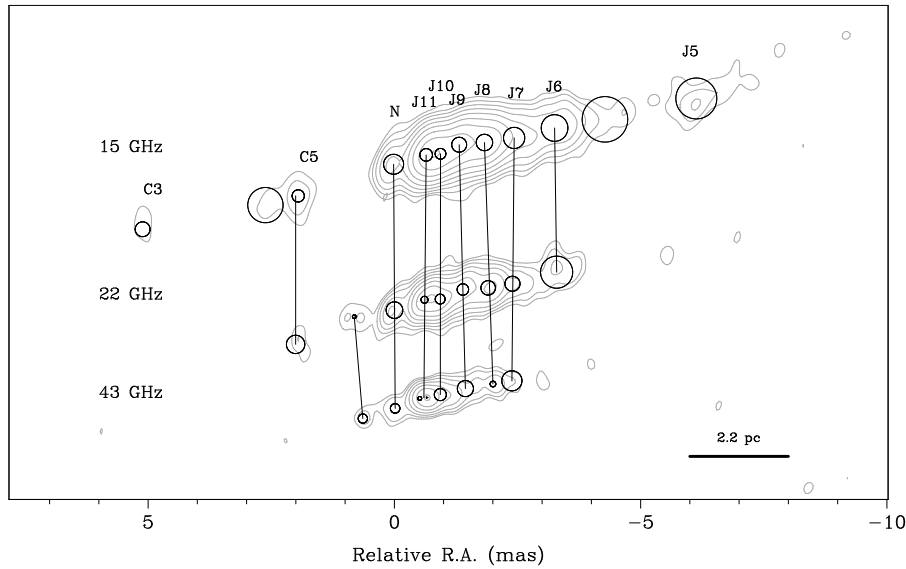
Figure 6.9: Identification of the modelfit components of the multi-frequency epoch 1996.73. The underlying images are the hybrid maps from which the modelfits were obtained. The parameters of the contour maps are given in Table 6.1; the contours start at $3\,\sigma$ and increasing in steps of 2.

The labels indicate the jet (J) and counter-jet (C) components as they result from the spectral and kinematical analysis given below. The component N labels the reference point of the kinematical analysis and it is assumed to be stationary. Although, it might not be the location of the central engine, the phrase 'core separation' is always used to describe the separation to component N at $r = 0$. The characteristic relative separations of adjacent components along the jets at the higher frequencies, were very useful to find an unambiguous alignment with reasonable accuracy. For example, the characteristic positions of the jet components J10 and J11 in 2003 (Figure 6.10) can be seen at all frequencies and mark a well defined structure, which can be used to align the images.

The situation between 5 GHz and 15 GHz is not as clear as at the higher frequencies, since the difference in resolution is much higher (Figure 6.11). However, supported by the results from the kinematics, the spectral analysis (Section 6.2.2 & 6.2.4) and the previous alignment found between 1.4 GHz, 5 GHz and 8.4 GHz (Bach 2001; Bach et al. 2002) a satisfactory alignment was found. Since the brightest component at 5 GHz is the sum of several jet components it is called N_5 and will be used as the reference point in the kinematical analysis at 5 GHz. The tendency to resolve ever more jet components with increasing
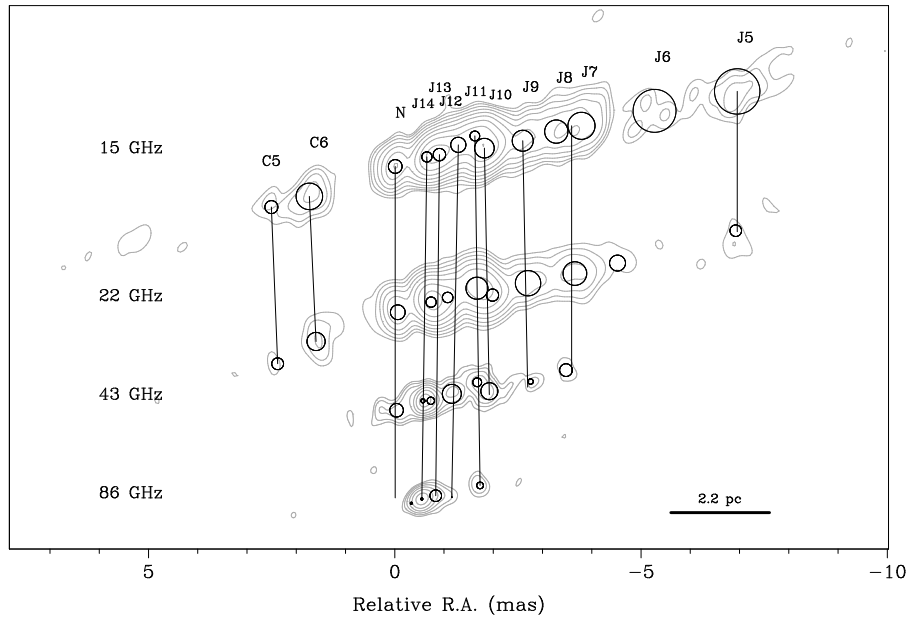
Figure 6.10: Identification of the modelfit components of the multi-frequency epochs in 2003. 15 GHz and 22 GHz are the hybrid maps of the phase-referenced observations (2003.04) and 43 GHz and 86 GHz are from 2003.27. Image parameters are described in the caption of Fig. 6.9.

resolution is not seen above 15 GHz. The only position where a new component at the higher frequency appears, which was not seen at lower frequencies, is between component N and J11 (J14) at 43 GHz and 86 GHz (Figure 6.9 & 6.10), but this region is likely affected by optical depth effects (see Section 6.2.2). Krichbaum et al. (1998) suggest that the most likely position of the central engine is located between our component N and the first jet component J10 (C1 and J0 in their paper) and it seems still to be the best position, but we will also see that component N is not necessarily the first counter-jet component (Section 6.2.6).

6.2.2   Spectral Analysis

Figures 6.12 to 6.14 show the spectral index maps with overlaid hybrid contour maps between 5 GHz, 15 GHz, 22 GHz, 43 GHz and 86 GHz. The overlaid contours are always given at the lower frequency. The images are registered in a way that the position of component N is at $r = 0$.

The shifts between the different frequencies were derived from the modelfits (Section 6.2.1) and are given in Table 6.4. For each spectral index map the higher frequency was imaged at the same resolution as the lower frequency by restricting the (u, v)-range to the maximum baseline length (in units of the observing frequency) at the lower frequency. The resulting maps were convolved with a circular beam corresponding to the size of the major beam axis of the lower resolution map. The beam sizes are given in the caption of the images. This procedure assures that we do not lose the extended emission at the higher frequency, which would result in steeper spectral indices with larger core sep-
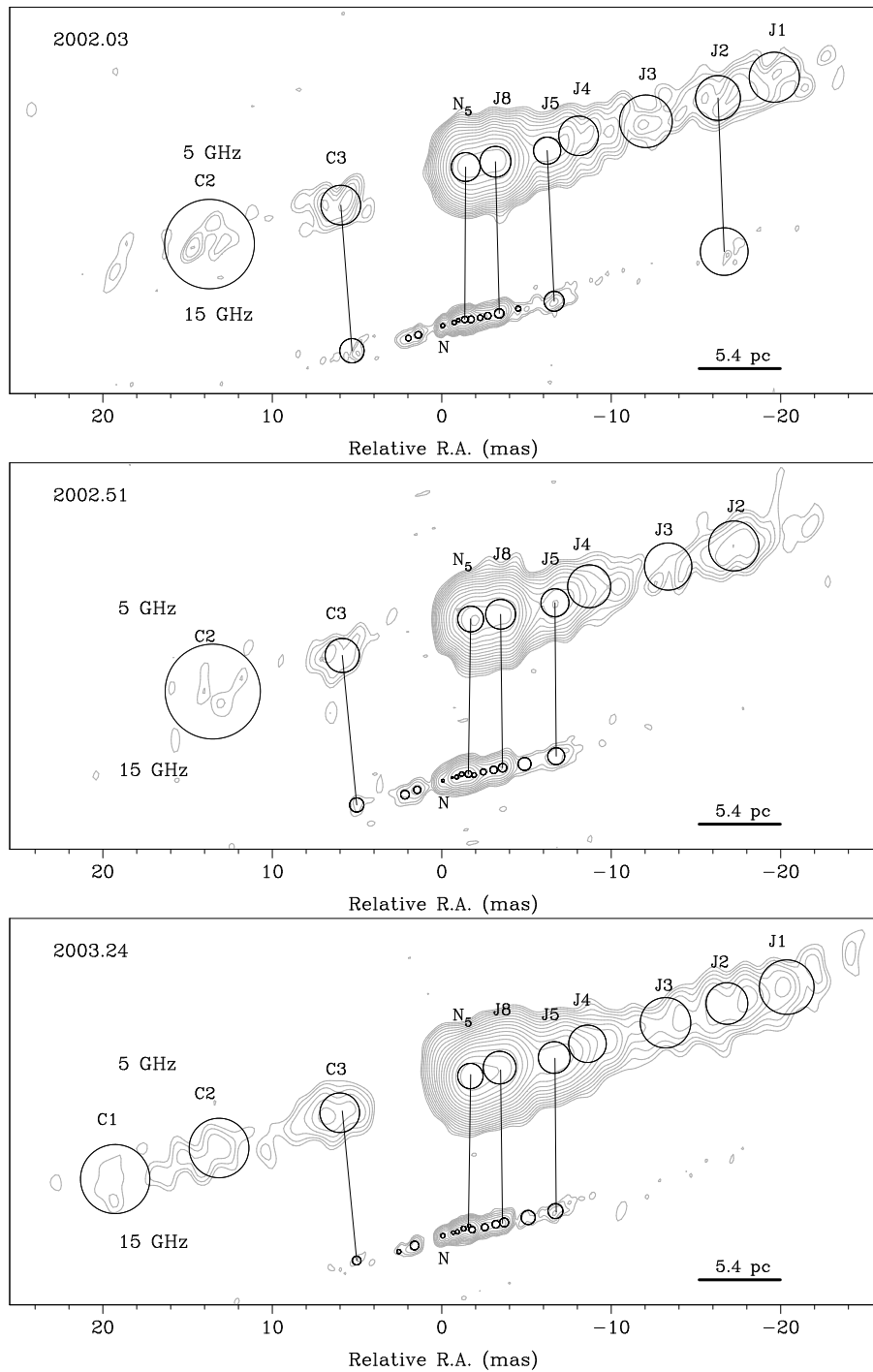
Figure 6.11: Identification scheme of the 5 GHz and 15 GHz maps between 2002 and 2003. The parameters of the contour maps are given in Table 6.1; the contours start at 3σ and increase in steps of 2.
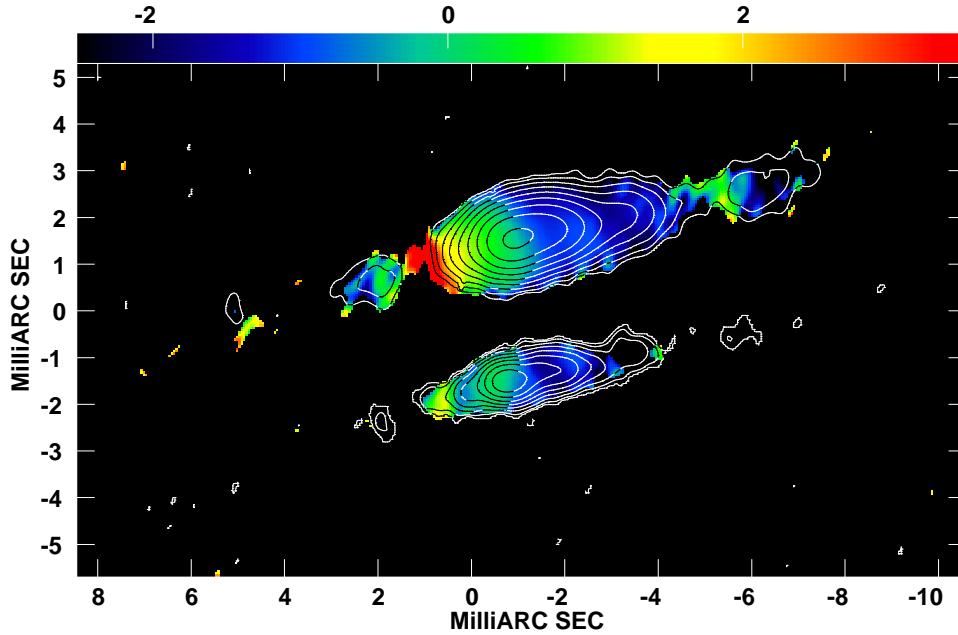
Figure 6.12: Spectral index maps between 15 GHz and 22 GHz (top), and 22 GHz and 43 GHz (bottom) with overlaid contours of the lower frequency image (1996.73). The maps were convolved with circular beams of 0.8 mas at (15/22) GHz and 0.5 mas at (22/43) GHz and the lowest contour corresponds to 2.5 mJy/beam

arations. The larger beam sizes also largely reduces the uncertainties, due to possible errors in the alignment between the different frequencies.

Table 6.4: Approximate shifts along the jet of the brightest component between the different frequencies. The given values are average values combing all epochs.

ν [GHz]	Δr [mas]
4.9–15.4	1.47 ± 0.32
15.2–22.2	0.19 ± 0.11
22.2–43.3	0.10 ± 0.07
43.3–86.2	0.06 ± 0.07

Our analysis reveals that most of the jet emission has a steep spectrum, whereas the counter-jet spectrum is flatter. The spectral properties in the core region are much more complex showing a highly inverted spectrum between 5 GHz and 15 GHz and also highly inverted regions at the higher frequency pairs, but always at different locations. A summary of the spectral indices along the jet is given in Table 6.5. The given values are average values of the specified jet region.

Spectral index profiles of the inner region around the core are presented in Figure 6.15 and they show more clearly the different behaviour of the spectral index at different frequency pairs. Since, the flux density errors are typically smaller than 10 %, a maximum uncertainty of 14 % applies for the spectral indices. Spectral index maps that were made by deliberately introduce slightly
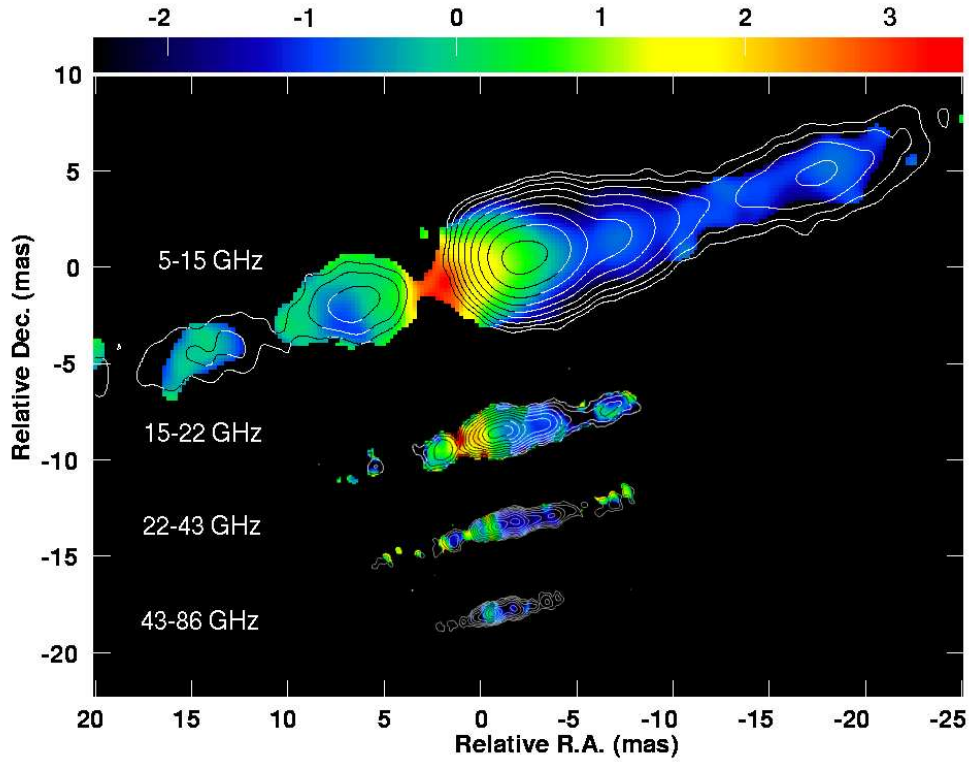
Figure 6.13: Spectral index maps between (5, 15, 22, 43, and 86) GHz with overlaid contours of the lower frequency image (2003.04 to 2003.27). The images of each spectral index map were taken simultaneous, except the spectral index map between 22 GHz (2003.04) and 43 GHz (2003.27), but a separation of 0.2 yr is small compared to the time scales on which Cygnus A evolves. The images were convolved with circular beams of 2 mas (5–15 GHz), 0.8 mas (15–22 GHz), 0.5 mas (22–43 GHz) and 0.4 mas (43–86 GHz) and the lowest contour corresponds to 3σ (see Table 6.1)

Table 6.5: Approximate values of the spectral index at the different frequencies along the jet.

r [mas]	$\alpha_{5/15}$	$\alpha_{15/22}$	$\alpha_{22/43}$	$\alpha_{43/86}$
-15.0 to -4.0	-0.2	—	—	—
-4.0 to -2.5	2.2	-0.6	—	—
-2.5 to -2.0	3.0	0.7	1.0	—
-2.0 to -1.0	2.9	1.4	-1.0	—
-1.0 to -0.5	2.1	3.0	1.0	—
-0.5 to 0.0	1.8	2.1	-0.4	-1.0
0.0 to 0.5	1.6	1.8	0.3	-0.3
0.5 to 1.0	1.4	0.6	-0.2	-0.5
1.0 to 5.0	0.3	-0.7	-1.5	-1.6
5.0 to 20.0	-0.7	-1.1	—	—
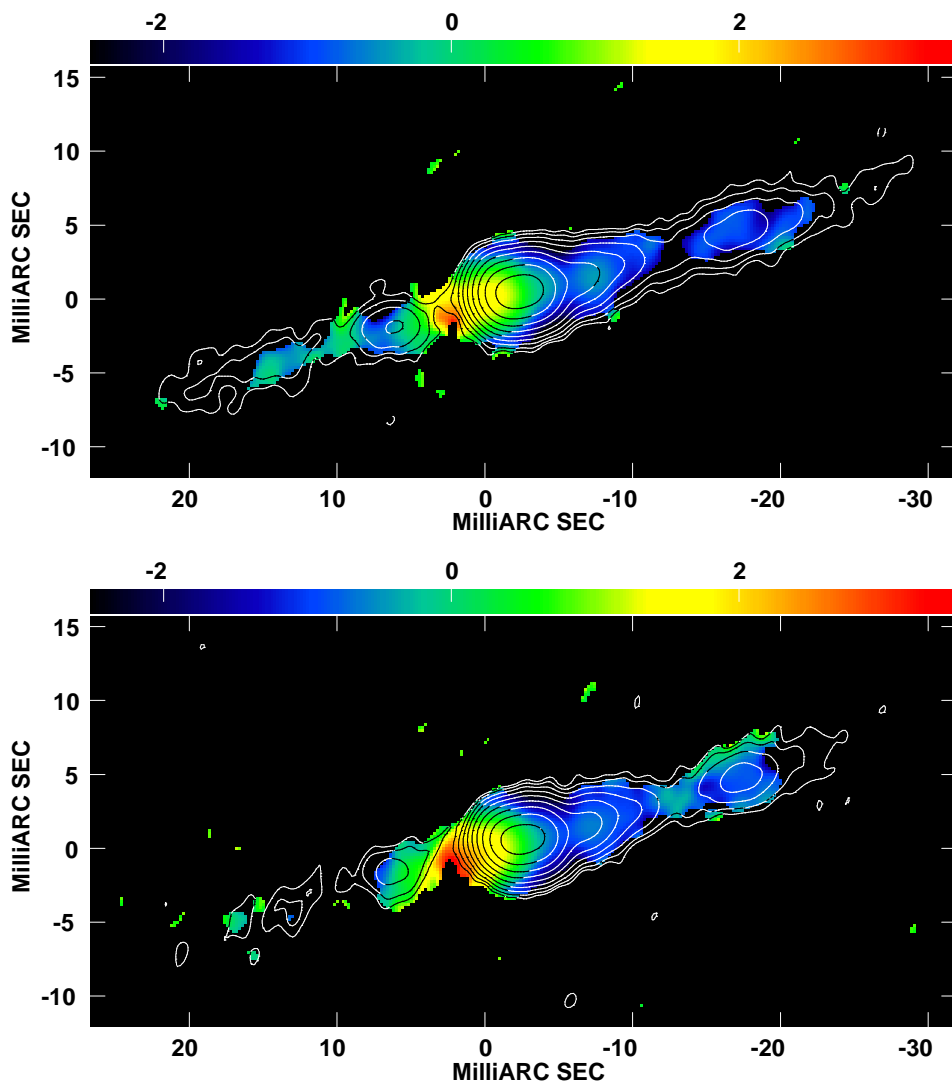
Figure 6.14: Spectral index maps between 5 GHz and 15 GHz with overlaid 5 GHz contours (2002.03 & 2002.51). The maps are convolved with a 2 mas circular beam and the lowest contour corresponds to 0.7 mJy/beam.

different shifts between the frequencies revealed that, due to the larger beam sizes, the uncertainties arising from the alignment errors are typically smaller than 5 %.
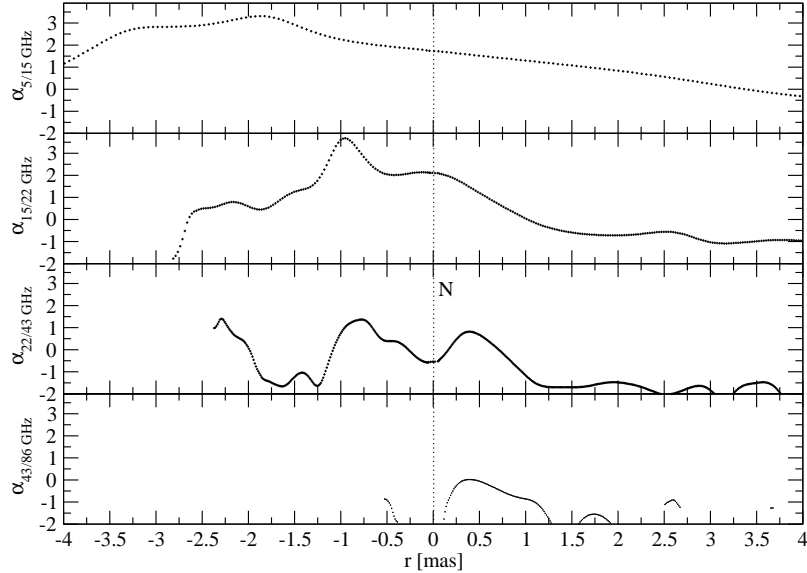
Figure 6.15: Spectral index profiles between frequency pairs at (5, 15, 22, 43, and 86) GHz. The profiles represent cuts through the spectral index maps along the ridge-line of the jet in Figure 6.13. The dotted line marks the position of component N.

Comparing the spectral indices at the same core separation in Figure 6.15 and in Table 6.5 reveals that the flattest region at frequencies above 15 GHz is at $r \approx 0.5$ mas coincident with the brightest component at 43 GHz and 86 GHz. This is most likely the region where the jet becomes optically thin at 86 GHz. Since, the $\tau = 1$ surface of the jet moves approximately with $r \propto 1/\nu$ closer to the footpoint of the jet and the position shifts of the brightest component are already small between 22 GHz 43 GHz and 86 GHz, this region should be very close ($r < 0.05$ mas) to the footpoint of the jet. The complex behaviour of the spectrum between $r \approx -4$ mas and $r \approx 0.5$ mas might be due to a combination of synchrotron self-absorption and a circum-nuclear absorber. The spectra of the core region are presented in Figure 6.16. The spectra were obtained by integrating flux density profiles at (5, 15, 22, 43 and 86) GHz from 2003 at intervals of 0.5 mas along the jet. In the panels between $r = 2$ mas and $r = 0.5$ mas a clear flattening of the spectrum at the higher frequencies is visible. In this region the inverted spectrum at $\alpha_{5/15}$ can be explained by synchrotron self-absorption and therewith the region becomes optically thick at 5 GHz.

Synchrotron self-absorption can produce spectral indices of up to 2.5, but between $(-5 \leq r \leq 0)$ mas the spectral index between 5 GHz and 15 GHz exceeds this maximum value significantly. The most likely explanation is that in this region the lower frequencies become affected by free-free absorption. The inner part of the counter-jet between 15 GHz and 22 GHz seems to be affected by free-free absorption. The absorber might even affect the counter-jet up to about 20 mas from the core since the spectrum in this part is still flat and not as steep

as on the jet side. This is supported by recent simulation of radiative transfer models for obscuring tori in active galaxies that were applied to Cygnus A (van Bemmel & Dullemond 2003). The spectral energy distribution (SED) was best fitted by an inclined ($\sim 50°$) torus of 10 pc to 30 pc, which would be in good agreement with our results.
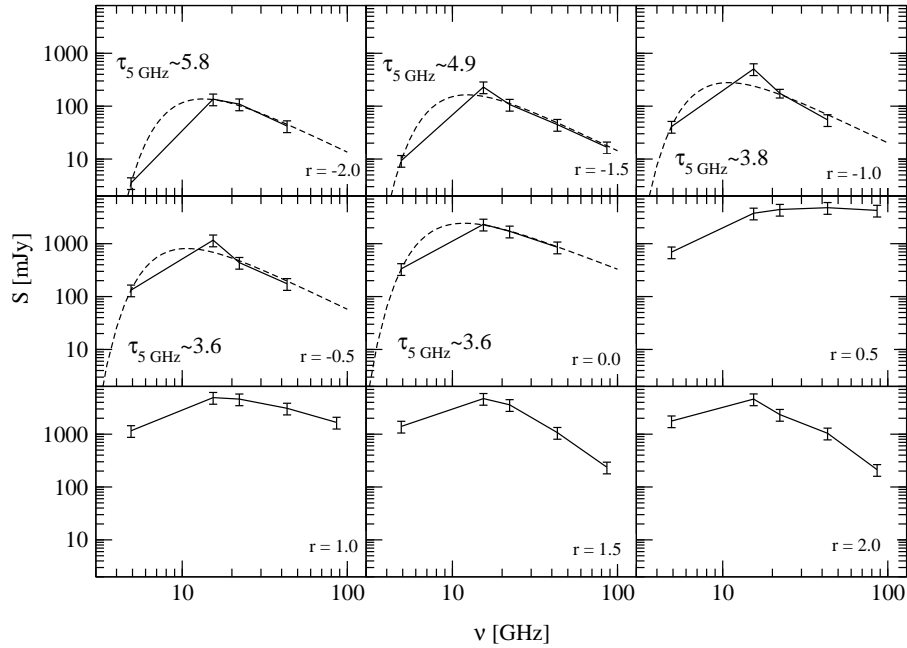
Figure 6.16: Jet spectra at different separations from the core. The spectra were obtained by integrating flux-density profiles at 5 GHz, 15 GHz, 22 GHz, 43 GHz, and 86 GHz from 2003 at 0.5 mas intervals along the jet. Where $\alpha_{5/15}$ exceeded a spectral index of 2.5, a free-free absorbed synchrotron spectrum was fitted to the data (see text).

Further evidence comes from UV spectroscopy (Antonucci et al. 1994) and optical spectro-polarimetry (Ogle et al. 1997) that show evidence for a hidden broad line region. According to the unified scheme, this is strong evidence for an obscuring torus around the central engine and is consistent with observations of H I absorption (Conway & Blanco 1995) close to the region where we see the highest absorption (left of the maximum in Figure 6.14, p. 84). The authors suggested that the absorption is caused by a ring or disk-like structure of gas with high H I opacity oriented perpendicular to the jet axis and shielding the inner part of the counter-jet. The required orientation would be close to that of the 2 kpc ring of dust and blue stars seen im HST images (Fosbury et al. 1999). Optical observation with the Keck telescope and the HST revealed an edge-brightened biconical structure on the scale of a few hundred parsecs (Jackson et al. 1998; Tadhunter et al. 1999). This structure is most likely a direct result of the nuclear-driven winds hollowing out ionization cones in the kiloparsec-scale dust lane in which the AGN is embedded. From these data, the best estimate for the half-opening angle of the biconical structure, and therefore of the torus, is about 60° and an inclination to the line-of-sight of $\geq 60°$ (Tadhunter et al. 2003). High resolution X-ray observations of the Cygnus A revealed also a

bipolar structure in the soft X-rays and a high absorption column density in the line of sight to the nucleus of $N_{\mathrm{H}} \approx 4 \times 10^{23}\,\mathrm{cm}^{-2}$ (Ueno et al. 1994; Young et al. 2002).

To estimate the amount of absorption in the radio bands we fitted a synchrotron spectrum that was modified by free-free absorption to the spectra in Figure 6.16, at the position where we think free-free absorption is most relevant:

$$S_\nu = S_0\, \nu_0^{\alpha_0} \times \exp(-\tau_\nu^{\mathrm{ff}}), \qquad (6.1)$$

where

$$\tau_\nu^{\mathrm{ff}} = 8.24 \times 10^{-2}\, T^{-1.35}\, \nu^{-2.1} \int N_+ N_-\, ds \qquad (6.2)$$

(e.g., Osterbrock 1989, eq. 4.32). Here, S_ν is the observed flux density in mJy, S_0 is the intrinsic flux density (before the radiation passes the absorber) in mJy, ν_0 is the frequency in GHz, α_0 is the dimensionless intrinsic spectral index, T is the gas temperature in K, N_+ and N_- are the number densities of positive and negative charges, respectively, in cm^{-3}, and s is the path length in pc. Assuming $N_+ = N_- = n_{\mathrm{e}}$ then $\int N_+ N_-\, ds$ reduces to $n_{\mathrm{e}}^2 \cdot s$.

The resulting optical depth at 5 GHz, $\tau_{5\,\mathrm{GHz}}$, is shown in the panels in Figure 6.16 at the different positions. The values of $\tau_{5\,\mathrm{GHz}}$ are upper limits, because part of the absorption can also be due to synchrotron self-absorption, but the fit will only be constrained by the optically thin emission from the higher frequencies. Although, the counter-jet seems to be affected by the absorption up to 20 mas from the core, we cannot apply this method for $r < -2\,\mathrm{mas}$, because there the counter-jet is only marginally detected at frequencies above 15 GHz and we need at least four frequencies to get a reliable fit. Assuming a typical temperature of 10^4 K we can solve the product $n_{\mathrm{e}}^2 \cdot s$ from Equation 6.2. Taking an average $\tau_{5\,\mathrm{GHz}}$ of 4.3 ± 1.0 results in $n_{\mathrm{e}}^2 \cdot s = (3.7 \pm 0.9) \times 10^8\,\mathrm{pc\,cm}^{-6}$. If we further assume a path length of about 5 pc (if the 'torus' is inclined we will observe only through the inner edge) the electron density is $n_{\mathrm{e}} \approx 4 \times 10^4\,\mathrm{cm}^{-3}$. This corresponds to a column density of about $7 \times 10^{23}\,\mathrm{cm}$, which is about two times higher than the column density inferred from X-ray absorption of $4 \times 10^{23}\,\mathrm{cm}^{-2}$ (Young et al. 2002). Since the X-ray measurement is made with a much lower resolution and therefore averages the absorption over a larger area, it is not surprising that we observe a higher column density.

Thus, the emission gap between the jet and the counter-jet at 5 GHz seems to be the imprint of a circum nuclear absorber that might cover also a large fraction of the counter-jet up to 20 mas and becomes thinner further out, where the counter-jet shines through.

6.2.3 Jet to Counter-Jet Ratio

Another indication of free-free absorption towards the counter-jet comes from the jet-to-counter-jet ratio, R (Equation 1.8). The jet-to-counter-jet ratio was estimated by summing all CLEAN components of the hybrid map models to the left and to the right of the position of component N. This was done for all

epochs and the result is shown in Figure 6.17. The scatter of the data points gives a good estimate of the uncertainties of the measurements. The errors bars are calculated assuming an error of 10 % for the flux density measurements.
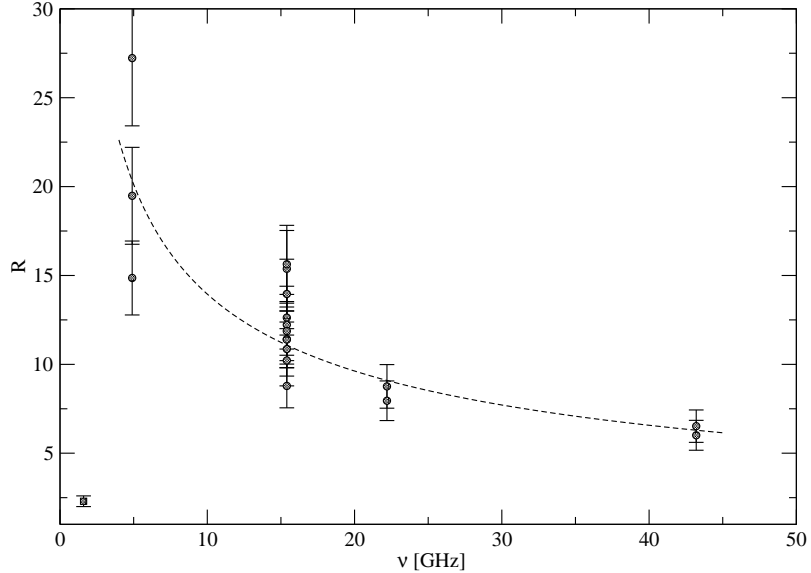
Figure 6.17: Frequency dependence of the jet to counter-jet ratio. Each point corresponds to a measurement at a different epoch. The dashed line represents an exponential fit to the data.

Specially at 5 GHz the measurement of R is strongly dependent on the location of core, or reference position, because of the strong flux density gradient between $r \approx -2$ mas and $r \approx 1$ mas. Since the reference position used in this work is shifted with respect to previous studies (Bach et al. 2002; Krichbaum et al. 1998) towards the counter-jet the values of R are also somewhat higher. This also shows the importance of the true location of the central engine and the continuation of our phase-referencing experiment will help to solve this question. However, the trend for the ratio to decreases towards higher frequencies is still present. The trend can be explained by an optical depth effect; if free-free absorption shields the inner part of the counter-jet, the emission will be absorbed at the lower frequencies and R will increase. Towards higher frequencies, the absorber would become optically thin and the jet to counter-jet ratio will decrease. Measurements at 1.6 GHz revealed again a much lower jet-to-counter-jet ratio of about 1.5 (Bach et al. 2002; Krichbaum et al. 1998), which can be explained if the absorbing region at this frequency becomes small compared to the beam size and the effect of the absorption is diluted. Therefore, the beam size of the 1.6 GHz observations can set an upper limit of 10 mas (corresponding to 10.8 pc) for the projected size of the torus. A reanalysis of the 1.6 GHz image from Bach et al. (2002) using the new alignment results in $R \approx 2.3 \pm 0.3$. Together with the apparent motion of the jet, the jet-to-counter-jet ratio can be used to constrain the angle to the line of sight (Equation 6.3).

6.2.4   Kinematics and Geometry

Most of the previous kinematical studies of the jet in Cygnus A were made at lower frequencies (Bach et al. 2002; Carilli et al. 1994), except one study at 22 GHz but using only two epochs (Krichbaum et al. 1998). To measure more precisely the motion in the jets we complemented our data set of six 15 GHz epochs with ten epochs from the VLBA 2 cm Survey (Kellermann et al. 2004, 1998; Zensus et al. 2002). These data cover exactly 8 years (1995.27 to 2003.27) and some of the epochs were separated by only a few weeks or months which proved very useful for resolving the confusion between the many jet components. The component-identification was made from epoch to epoch by comparing the individual models in x, y coordinates and their flux density. Figure 6.18 shows the hybrid maps with overlaid modelfit components and solid lines to indicate the moving jet components. Several different identification scenarios were tested, assuming either that

- the brightest component is stationary,

- one of the inner jet components (at the right hand side of the maximum) is stationary,

- a fictitious point, defined by the weighted mean between N and the brightest component is stationary,

- that component N is stationary.

The best fit was obtained assuming N to be stationary and all components of the jet and the counter-jet are moving away from this position. The first scenario caused unusually large shifts between some closely spaced epochs indicating that the brightness maximum is not stationary and no motion was observed on the counter-jet side. Fixing one of the inner jet components produced the worst alignment causing inwards motion on the counter-jet side. The weighted mean scenario was also highly affected by the changes in the brightness maximum. Therefore, we assumed that component N is not moving and we are able to measure the motion of the other components with respect to that position (see also Section 6.2.6 for a discussion about the nature of N).

Figure 6.19 displays all modelfit components against time and linear fits to those, yielding proper motions, μ, as follows. On the jet side the components start with $0.14 \, \mathrm{mas \, yr^{-1}}$ near the core and accelerate to $0.28 \, \mathrm{mas \, yr^{-1}}$ at larger separations. On the counter-jet side the components are not so well constrained and only the two innermost components show significant motion of $(-0.09 \pm 0.02) \, \mathrm{mas \, yr^{-1}}$ and $(-0.18 \pm 0.03) \, \mathrm{mas \, yr^{-1}}$. If component N is not a stationary feature that is somehow related to the central engine or the footpoint of the jet or the counter-jet then it is most likely a counter-jet component. Hence, a motion of component N would increase the motion on the counter-jet side and decrease the observed motion in the jet. From our analysis, however, we are confident that we can exclude higher proper motions than $0.02 \, \mathrm{mas \, yr^{-1}}$ for component N, but certainly this can only be answered from the coming phase-referencing observations.
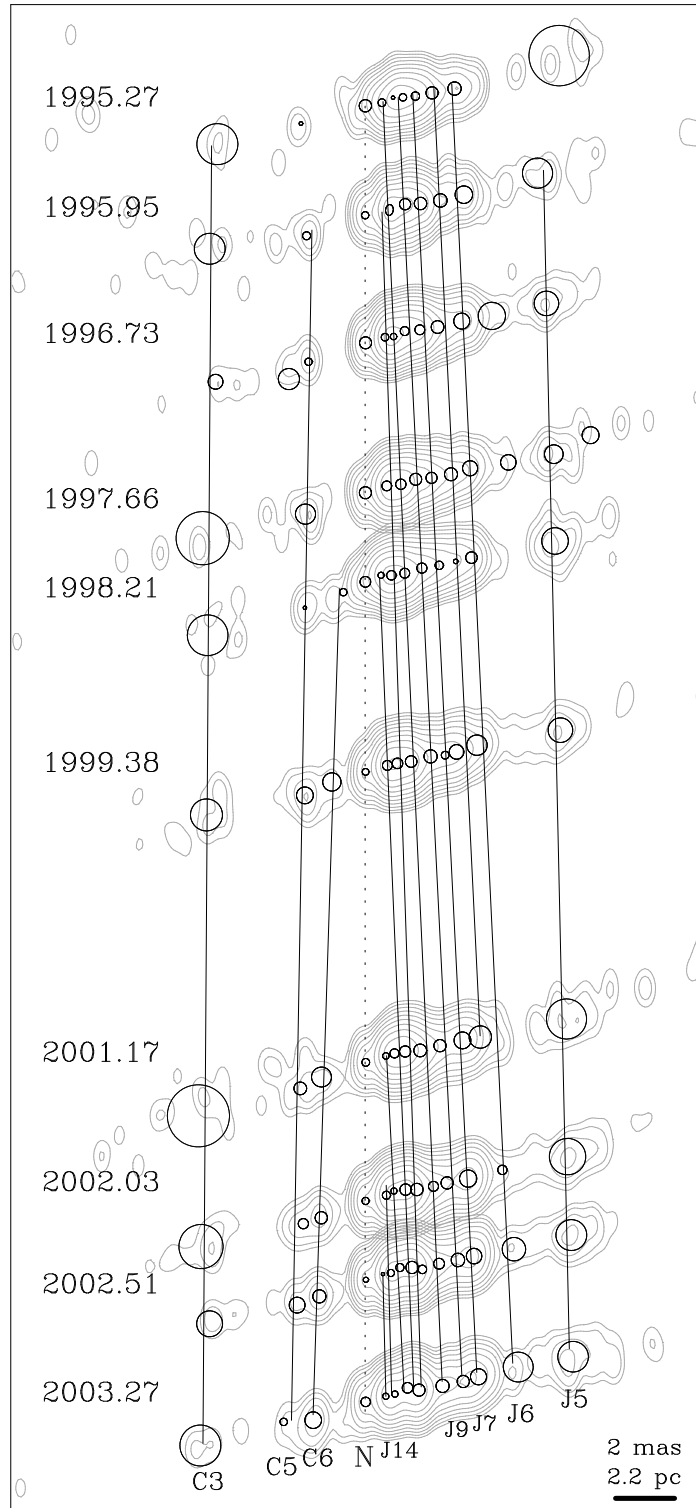
Figure 6.18: Time series of 15 GHz VLBI images with overlaid modelfit components. The solid lines guide the motion of the components, the dashed line connects component N, which is not moving in this scenario. Figure 6.19 shows the motion of all modelfit components.
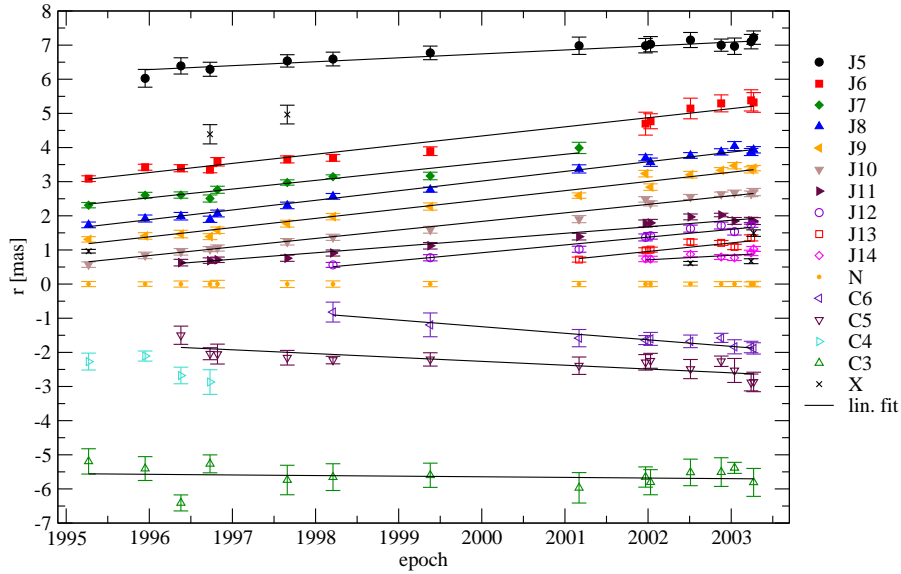
Figure 6.19: Core separation vs. time of the modelfit components at 15 GHz. The solid lines represent the linear fits to the different components. The results of the fits are given in Table 6.6.

All proper motions, the corresponding apparent speeds, and the minimum Lorentz factor, $\gamma_{\mathrm{min}} = \sqrt{\beta_{\mathrm{app}}^2 + 1}$, are given in Table 6.6. The errors are derived from the uncertainties of the weighted linear regression and the last column gives the reduced χ^2 of these fits. The new alignment reveals somewhat faster proper motions in the inner jet region ($r < 4\,\mathrm{mas}$) than previous studies (Bach et al. 2002; Krichbaum et al. 1998), but since these studies were all based on two or three epochs with sometimes separations of several years the component identification was not unique. A ten percent increase in the measured speeds was due to the new cosmology used (see Section 1, p. 1). The identification was mostly based on the very closely spaced epochs between 2002 and 2003 and between 1996 and 1997. After aligning the epochs in those time ranges it was possible to trace the found component well with linear fits through the other epochs.

By comparing the proper motions of the individual components it seems that the jet components accelerate as they travel down the jet and reach their maximum speed of $\sim 1\,c$ at a distance of $r \geq 2\,\mathrm{mas}$. To account for the possible acceleration, a polynomial function was fitted to those components where the χ_{r}^2 of the linear fit exceeded unity, but for none of the components a better fit was obtained. The minimum Lorentz factors given in Table 6.6 correspond to a minimum intrinsic speed, β_{min}, of $0.4\,c$ to $0.7\,c$ and an angle to the line of sight that maximizes the apparent speeds, θ, of $50°$ to $70°$. From the appearance of the jets on the VLBI images and also from the larger scale jets on the VLA images (Perley et al. 1984) it seems reasonable to assume that the jets are relatively straight and the differences in the observed motion can be more likely related to changes in the intrinsic speed than to changes of the viewing angle. Using the fastest observed motion of J8 ($1.04\,c$) the lower limit of the intrinsic

Table 6.6: Proper motions of the jet and counter-jet components at 15 GHz (negative motion corresponds to outwards motion on the counter-jet side). The apparent speeds were derived as described in Section 4.2.2.

Comp	μ [mas/yr]	β_{app}	γ_{min}	χ_{r}^2
C3	-0.013 ± 0.034	-0.05 ± 0.13	1.00	1.6
C5	-0.085 ± 0.021	-0.32 ± 0.08	1.05	0.9
C6	-0.183 ± 0.029	-0.68 ± 0.11	1.21	0.3
J14	0.139 ± 0.065	0.52 ± 0.24	1.13	1.2
J13	0.247 ± 0.052	0.92 ± 0.19	1.36	1.5
J12	0.226 ± 0.018	0.84 ± 0.07	1.30	1.3
J11	0.198 ± 0.011	0.73 ± 0.04	1.24	1.5
J10	0.252 ± 0.006	0.94 ± 0.02	1.37	0.8
J9	0.269 ± 0.011	1.00 ± 0.04	1.41	2.0
J8	0.282 ± 0.007	1.04 ± 0.03	1.45	0.8
J7	0.249 ± 0.026	0.92 ± 0.10	1.36	1.6
J6	0.242 ± 0.018	0.90 ± 0.07	1.34	1.2
J5	0.111 ± 0.010	0.41 ± 0.04	1.08	0.2

speed $\beta_{\mathrm{min}} \approx 0.7\,c$ corresponds to an angle to the line of sight of $\theta \approx 50°$. Combining the results from all previous studies the most likely range of the viewing angle is restricted to $65° \leq \theta \leq 85°$ (Bach et al. 2002; Krichbaum et al. 1998, and Carilli & Barthel (1996) for a summary of previous studies before 1996).

The viewing angle can be further constrained by combining the measured apparent speeds with the jet-to-counter-jet ratio. Solving Equation 1.6 and Equation 1.8 for θ leads to

$$\theta = \arctan^{-1}\left(\frac{2\beta_{\mathrm{app}}}{R^{1/(2-\alpha)} - 1}\right), \tag{6.3}$$

where R is the jet-to-counter-jet ratio and α is the spectral index. Using the measurements of R at 1.4 GHz, which should be only weakly affected by the absorption in the few central parsecs, and which varies between 1.4 and 2.4 (depending on the position of the core), $\alpha = -0.5$ for optically thin emission, and $\beta_{\mathrm{app}} \approx 0.9$ we obtain $57° \leq \theta \leq 78°$.

Therefore it is most likely that the jets of Cygnus A are not observed under the angle that maximises the apparent speed ($\cot\theta = \beta_{\mathrm{app}}$), but are seen at larger viewing angles (on the right hand side of the maximum of Figure 1.4, p. 9). A list of possible jet parameters and their resulting observable is shown in Table 6.7. Using this list one can try to find a single set of jet parameters that explain the observed speeds on the jet side and on the counter-jet side, and the jet-to-counter-jet ratio together. By restricting ourselves to solutions that have a jet Doppler factor of more than one (exclude deamplification), we obtain $70° \leq \theta \leq 80°$ and $0.8 \leq \beta \leq 0.9\,c$ (corresponding to $1.4 \leq \gamma \leq 2.3$). For smaller viewing angles R would become too large and for angles $> 80°$ the observed motions on the counter-jet side should be larger. At speeds smaller

than $0.8\,c$ the apparent jet speeds become too small and at speeds larger than $0.9\,c$ the deamplification gets too large.

Table 6.7: Range of possible intrinsic jet parameters (β and θ) and the resulting observable (β_{app} in jet and counter-jet, Doppler factor δ, and jet-to-counter-jet ratio R).

β [c]	θ [$^\circ$]	$\beta_{\mathrm{app,j}}$ [c]	$\beta_{\mathrm{app,c-j}}$ [c]	δ	R
0.7	65	0.90	0.49	1.4	4.6
0.8	65	1.10	0.54	1.0	5.8
0.9	65	1.32	0.59	0.6	7.4
0.7	70	0.86	0.53	1.6	3.4
0.8	70	1.03	0.59	1.1	4.1
0.9	70	1.22	0.65	0.6	4.9
0.7	75	0.83	0.57	1.7	2.5
0.8	75	0.97	0.64	1.1	2.9
0.9	75	1.13	0.71	0.7	3.3
0.7	80	0.78	0.61	1.9	1.8
0.8	80	0.91	0.69	1.2	2.0
0.9	80	1.05	0.77	0.7	2.2
0.7	85	0.74	0.66	2.2	1.4
0.8	85	0.86	0.75	1.4	1.4
0.9	85	0.97	0.83	0.7	1.5

We note that the observed speeds on the counter-jet side are not so well constrained as on the jet side, because we observe only two components (C5 & C6) and they have different speeds. But both of these components are visible in more than ten epochs spread over several years and follow a defined path. Therefore, they have to be considered as representatives of well defined physical regions. Although with a large uncertainty due to its faintness, component C3 shows a somewhat slower proper motion, but this component is also visible at 5 GHz and its motion can be confirmed. In Figure 6.20 and in Table 6.8 the results of the kinematic analysis of the 5 GHz data is presented. Due to the sparse time sampling and the different resolutions, a unique identification is difficult, but settled the most plausible one based on the alignment found in previous studies at 5 GHz (Bach et al. 2002; Carilli et al. 1994). The labels identify the components with those at the same separation at 15 GHz, although they are actually the sum of multiple high frequency components and therefore it is questionable how these features are related to the jet flow. However, the apparent speeds at 5 GHz are comparable with those at 15 GHz and thus the component blending has not affected the speed estimate.

A summary of all apparent speed measurements of the parsec-scale jets in Cygnus A are presented in Figure 6.21. Obviously, the infrequent time sampling of previous studies has lead to an underestimation of the speeds in the jets of Cygnus A. One can see that the jet seems to accelerate from about $0.5\,c$ at $0.5\,\mathrm{mas}$ to about $1\,c$ at $3\,\mathrm{mas}$ and continues at this speed at least to about $50\,\mathrm{mas}$, from the core. Parsec-scale acceleration has been observed in a number of other sources e.g., NGC 6251 (Sudou et al. 2000) and NGC 315 (Cotton et al.
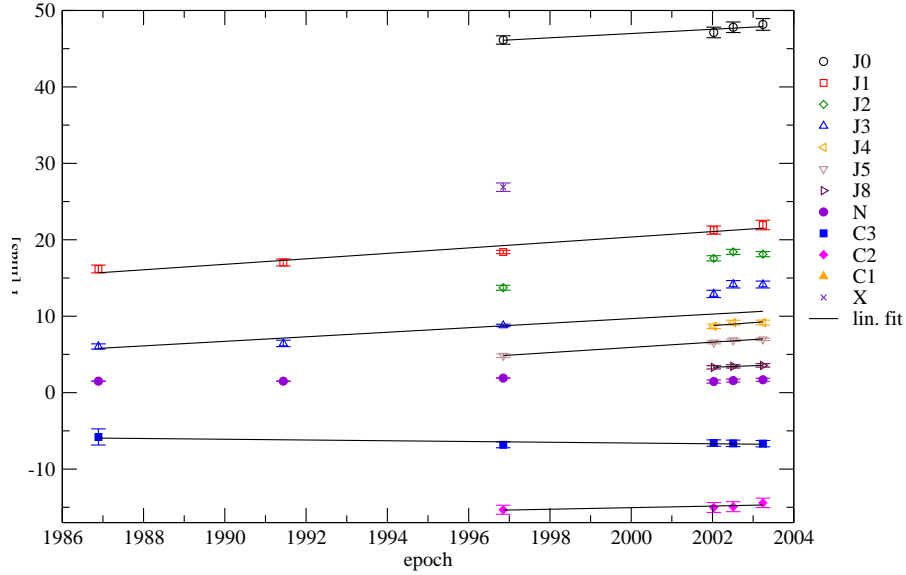
Figure 6.20: Core separation vs. time of the modelfit components at 5 GHz. The solid represent the linear fits to the different components. The data points from 1986 and 1991 are from Carilli et al. (1994) and 1996 from Bach et al. (2002).

Table 6.8: Proper motions of the jet and counter-jet components at 5 GHz (negative motion corresponds to outwards motion on the counter-jet side). The apparent speeds were derived as in Section 4.2.2.

Comp[a]	μ [mas/yr]	β_{app}	γ_{min}	χ_{r}^2
C2	0.003 ± 0.091	0.01 ± 0.34	1.00	0.6
C3	-0.018 ± 0.028	-0.07 ± 0.10	1.00	0.3
J8	0.200 ± 0.028	0.74 ± 0.10	1.24	0.0
J5	0.341 ± 0.045	1.27 ± 0.17	1.61	0.2
J4	0.389 ± 0.274	1.44 ± 1.02	1.75	0.6
J3	0.297 ± 0.067	1.10 ± 0.25	1.49	3.4
J1	0.337 ± 0.067	1.25 ± 0.25	1.60	3.2
J0	0.280 ± 0.062	1.04 ± 0.23	1.44	0.3

[a]The labels identify the components with those at the same separation at 15 GHz, although they are actually the sum of multiple high frequency components.
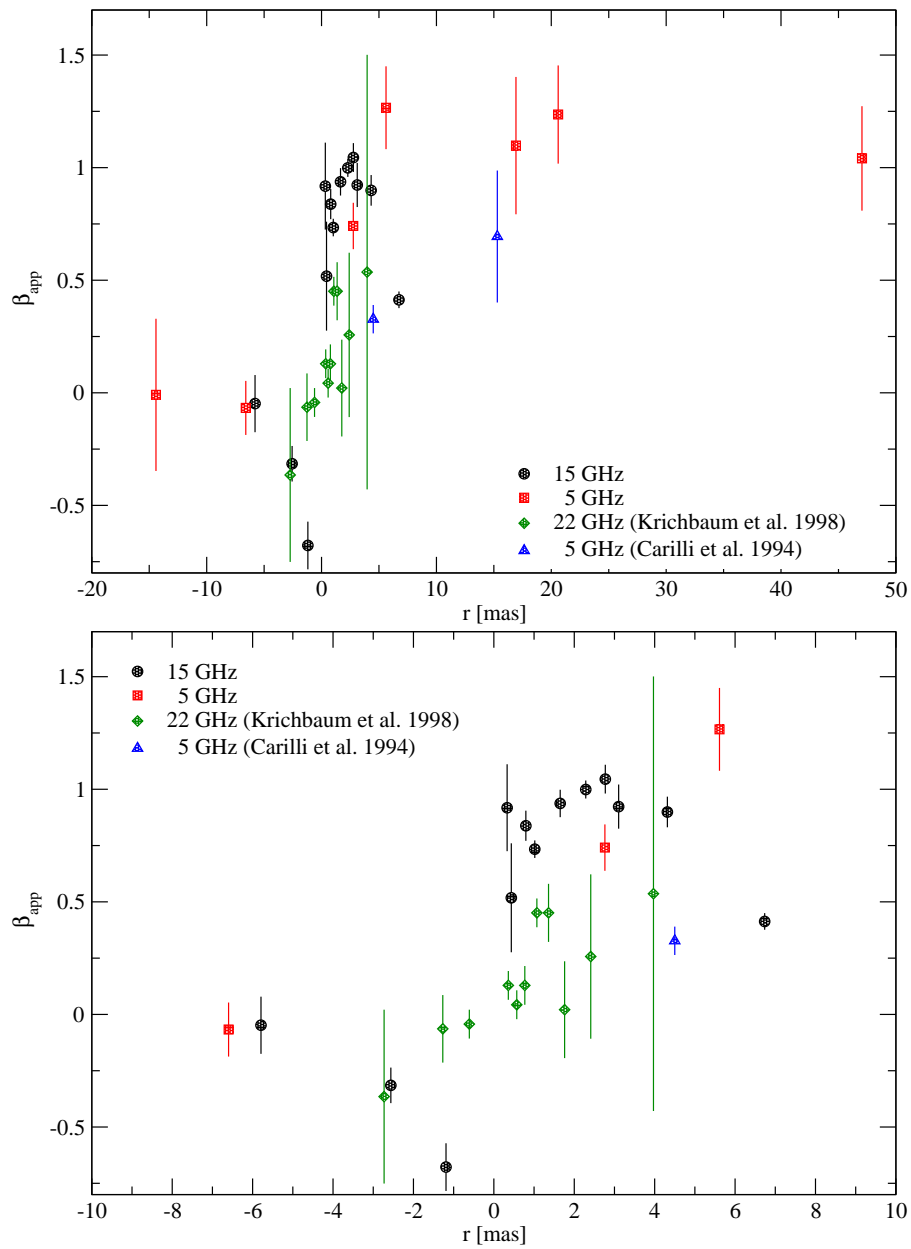
Figure 6.21: All existing proper motion measurements of the parsec-scale jet vs core separation.

1999), but the common mechanisms to accelerate jets, like thermal acceleration of a proton-electron plasma (Melia et al. 2002) or centrifugal driving (Blandford & Payne 1982), act on much smaller scales. A mechanism which seems to explain the observed acceleration in NGC 6251 is a magnetic driven acceleration that involves acceleration by a gradient in the azimuthal magnetic-field pressure.

The velocity structure on the counter-jet side is less clear. Most of the counter-jet components do not show the fast motion that would be expected from a simple conical jet model (Königl 1981) that assumes symmetry between the intrinsic properties of the jet and the counter-jet. From Table 6.7 we have seen that, at an an inclination of 65 ° to 85 °, one would expect a proper motion of $\beta_{\mathrm{app}} = 0.5\,c$ to $\beta_{\mathrm{app}} = 0.7\,c$ on the counter-jet side. That we do not see these 'high' speeds (except component C6) in the counter-jet points to a more complicated jet structure. It might be that because we observe a stratified jet with the different velocities belonging to different layers and because we see the counter-jet from its 'back' then the emission of the faster components is beamed away from us and we observe only the slower velocities of the outer sheath of the counter-jet. These jet models are called two-fluid models (Pelletier & Roland 1989; Sol et al. 1989).

There is growing evidence that the jets in radio galaxies indeed exhibit stratified jets e.g., 3C 31 (Laing & Bridle 2002), 3C 353, (Swain et al. 1998), and B2 1144+35 (Giovannini et al. 1999. A recent statistical analysis of a sample of radio galaxies also suggests that their jets contain a highly relativistic spine ($\gamma \geq 10$) in the centre surrounded by slower layers (Laing et al. 1999). In the case of Cygnus A we would not be able to detected the fast spine, because of its large inclination which beams the radiation of the spine away from us (see Section 1.2.3 about relativistic beaming).

6.2.5   The Jet Opening Angle

An important constraint on jet physics is the opening angle. For a freely expanding jet the opening angle, Θ, will equal two times the Mach angle Φ defined by

$$\tan \Phi = \frac{1}{\gamma M}, \qquad (6.4)$$

where M is the Mach number and γ is the jet Lorentz factor. The Mach number is a dimensionless number giving the ratio of the speed of an object to the ambient speed of sound in the surrounding medium. The jet opening angle was derived from the FWHM of the modelfit components at 5 GHz and 15 GHz (Figure 6.22). At the other frequencies the small number of components does not allow one to obtain a reliable fit. The opening angle of the jet is $(4.6 \pm 0.6)°$ at 5 GHz and $(6.7 \pm 0.7)°$ at 15 GHz. The opening angle of the counter-jet $(6.6 \pm 1.2)°$ at 5 GHz and $(8.5 \pm 1.5)°$ at 15 GHz. Although visible at both frequencies the difference between the jet and the counter-jet opening angle is not significant, because the uncertainties for the components on the counter-jet side are much larger than for those on the jet side. More reliable is the difference between the jet opening angle between 5 GHz and 15 GHz, suggesting that the

jet opening angle decreases with larger separations from the core.

Using the opening angle of the jet we obtain $\gamma M \approx 25$ at 5 GHz and $\gamma M \approx 17$ at 15 GHz. For a free relativistic jet filled with relativistic fluid the internal sound speed is $c/\sqrt{3}$, hence $M = \sqrt{3}$ and thus the Lorentz factors are $\gamma = 14$ and $\gamma = 10$, which are already at the upper boundary for superluminal quasars (Vermeulen & Cohen 1994). Previous studies revealed a wide range of γM measurements up to 72 (Carilli & Barthel 1996) depending on the scale at which the opening angle was measured. In general one finds that the measured viewing angle is smaller on larger scales and the most reasonable conclusion is that the Cygnus A jet is not freely expanding, but is confined. The simplest way to confine the jets would be external pressure. Perley et al. (1984) point out that minimum energy pressures in the jet are about an order of magnitude greater than in the lobes, therefore requiring an alternative means for jet confinement, if minimum conditions apply. However, X-ray and optical observations suggest that the lobes may be over-pressured relative to equipartition values by just this amount and hence that pressure confinement may still be viable (Carilli et al. 1989; Osterbrock 1989; Reynolds & Fabian 1996).

6.2.6 The Nature of Component N

So far, component N was only used as the reference point. It was used to define a common point at which all images at different frequencies were aligned and it turned out that N seems also to be the most stationary feature in the jets of Cygnus A. In previous studies N was referred to as the first counter-jet component (Bach et al. 2004; Krichbaum et al. 1998). If N is indeed the first counter-jet component or the footpoint of the counter-jet, this would place the central engine between N and the first jet component (J14 in 2003). Footpoint of the jet means the $\tau = 1$ surface, where the jet starts to be optically thin.

For jets it is commonly excepted that the brightest jet component that usually shows also a flat spectrum marks the footpoint of the jet and we have seen that in Cygnus A this component has indeed a flat spectrum and therefore seems to mark the $\tau = 1$ surface of the jet. It is also the region with the largest variations in the flux density and where the new jet components seem to appear.

These characteristics, however, seems to disqualify N as the footpoint of the counter-jet. Component N shows a steep spectrum at the higher frequencies (Figure 6.16) and appears not very variable, though that can be explained if the variations that cause the variability are relativistically beamed and therefore are suppressed on the counter-jet side. Assuming that N is already an optically thin counter-jet component is questionable since we can follow the ejection of a new counter-jet component around 1998 without any variations seen in N.

Another possibility would be that N is related to the true central engine. There is observational evidence mainly from X-rays for hot gas coexisting with cold gas in the vicinity of an accreting black hole (e.g., Mushotzky et al. 1993), which is presumably a corona lying above an accretion disc. The average brightness temperature of $(3.3 \pm 0.4) \times 10^9$ K at 15 GHz (the given error correspond to the standard deviation of the measurements) and the steep spectrum of N do not contradict a thermal origin of the emission. Simulations by Liu et al.
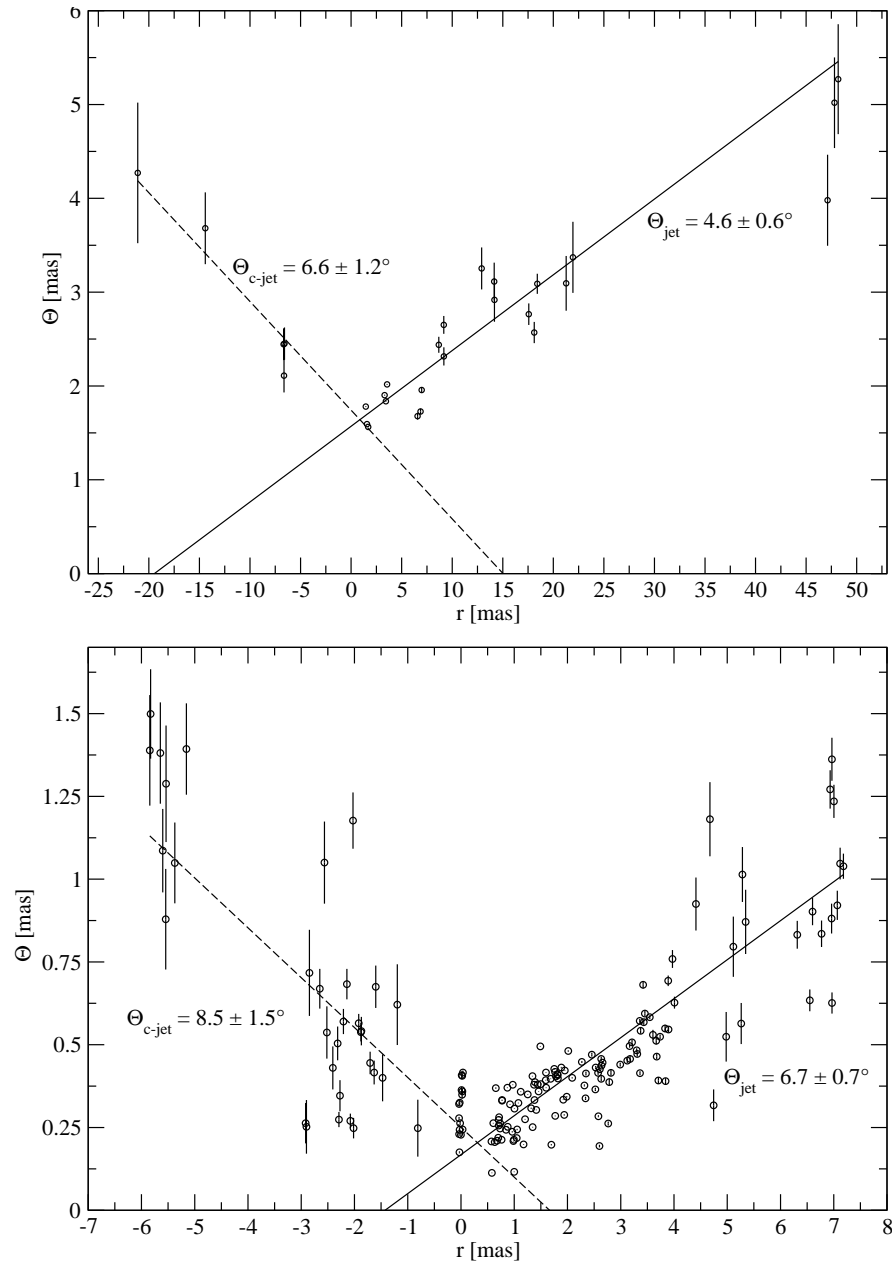
Figure 6.22: Shown are a plots of the width of the modelfit components against their separation from the core at 5 GHz (top) and 15 GHz (bottom). The opening angle was derived from a weighted linear regression to the data.

(2003) show that it is possible to create such a corona above the accretion disk at radii of about 3 to 50 Schwarzschild radii for a $10^8 \, M_\odot$ black hole and an accretion rate of 0.1 $\dot{M}_{\mathrm{Edd}}$, which is comparable to what we expect for the AGN in Cygnus A (Conway & Blanco 1995). Liu et al. (2003) derive plasma temperatures of a few $10^9 \, \mathrm{K}$, electron densities of $3 \times 10^9 \, \mathrm{cm}^{-3}$, and magnetic fields of about $10^3 \, \mathrm{G}$, which would be sufficient to create synchrotron emission at radio wavelengths. Therefore it might be possible that N can be related to such a hot corona above the accretion disc.

Since the spectrum seems to peak around 15 GHz we can estimate the total luminosity, L, of N from $L \propto \nu S d_{\mathrm{L}}^2$ to about 1.5×10^{41} erg/s, where S is the flux density, ν is the frequency, and d_{L} is the luminosity distance. We can now compare this value to the predicted from the corona simulations. The total emitted radiation of a single electron is given by

$$
\begin{aligned}
P &= \frac{3}{4}\beta^2\Gamma^2 c\sigma_{\mathrm{T}}U_{\mathrm{B}}, \text{ with} \\
\Gamma &= \frac{kT}{\beta m_{\mathrm{e}}c^2},
\end{aligned}
\tag{6.5}
$$

where $\beta \approx 1$ is the speed of the electrons, their Lorentz factor is Γ, σ_{T} is the Thompson cross-section ($6.65 \times 10^{-25} \, \mathrm{cm}^2$), $U_{\mathrm{B}} = B^2/8\pi$ is the energy density of magnetic field, k is the Boltzmann constant (1.38×10^{-16} erg/K), T is the temperature, and m_{e} is the mass of the electron (9.1×10^{28} g). Using the parameters from Liu et al. (2003) the emission per particle is about 1.5×10^{-8} erg/s. Multiplied by the number density of particles and assuming a cylindrical geometry for the corona above the accretion disk with an extend of about 50 pc and a hight of 1 pc, and that the whole volume is optically thin, the total luminosity of the corona would be $L = 2.4 \times 10^{45}$ erg/s. This is about 10^4 times higher than the observed value, which either means that the coronal model is not applicable, or that the cyclotron frequency (eB/mc) is much smaller than 15 GHz and the missing emission at the lower frequencies is cut by the steep Rayleigh Jeans part of the thermal spectrum. In the later case, however, one should observe a very steep synchrotron spectrum and it would not be possible to see component N anymore at the higher frequencies. Therefore, it seems that the model is actually not applicable and the most likely explanation left is that N is already part of the counter-jet.

6.3 Conclusions

We carried out an intensive VLBI study of the core region of Cygnus A at 5 GHz, 15 GHz, 22 GHz 43 GHz and 86 GHz during the last three years. Combing these new high quality data with archival data dating back to 1995 revealed new insights into the kinematics of the jets and the spectral properties of the nuclear region.

The analysis of the multi-frequency data revealed a steep jet spectrum and a more complex spectrum around the core. The spectrum between 5 GHz and

15 GHz is clearly inverted, at separations between $-0.5 \leq r \leq 0.5$ mas, whereas at the higher frequencies the same region shows a flat spectrum. On the counter-jet side the inner part ($r \leq 2$ mas) shows a highly inverted spectrum with an $\alpha_{5/15}$ of more than 3, $\alpha_{15/22}$ of up to 2.5 and $\alpha_{22/43} \approx 1$. In the outer regions, the counter-jet spectrum flattens first at frequencies above 15 GHz and later also between 5 GHz and 15 GHz. Together with the frequency dependence of the jet to counter-jet ratio and further indications from H I absorption (Conway & Blanco 1995), modelling of the infrared emission (van Bemmel & Dullemond 2003), UV spectroscopy (Antonucci et al. 1994), optical spectro-polarimetry (Ogle et al. 1997), and recent high resolution optical and X-ray observations (Tadhunter et al. 2003; Young et al. 2002) there is strong evidence for the existence of a free-free absorbing torus. Although we do not directly see the torus and cannot precisely measure its geometry, the observations suggest that the absorber is oriented perpendicular to the jet axis with a half opening angle of about 60° and a maximum extent of about 30 pc. It effectively blocks the 5 GHz emission in the inner ~ 4 pc and the optical depth decreases further out.

We measured apparent speeds of $0.5\,c$ to $1\,c$ in the jet and $0.3\,c$ to $0.6\,c$ on the counter-jet side. The apparent acceleration in the jet and the large differences in the measured motions on the counter-jet side might reflect a more complicated jet structure than that of the simple Königl jet with a well defined jet flow and questions the assumption that the jet and counter-jet are intrinsically the same. The differences of the jet and the counter-jet speeds might be caused by a stratification of the jet where we observe different velocity sheaths depending on the optical depth and the orientation of the jet. Assuming that the highest speeds on both sides are due to a jet flow at intrinsically the same speed, and using the possible range of the jet-to-counter-jet ratio to further constrain the results, the most likely jet parameters are a jet Lorentz factor of about 2 (corresponding to $\beta \approx 0.9\,c$) and an angle to the line of sight of 70° to 80°. Jet Lorentz factors of 1.5 to 2 and Doppler factors of about 1 seem to be typical for radio galaxies and are significantly lower than those from radio-loud quasars with typical values of 10 (Lähteenmäki & Valtaoja 1999).

With regard to the unified scheme, Cygnus A supports the idea that type 2 AGN, which do not show broad emission lines, are indeed seen from large viewing angles and the BLR is shielded behind a circum-nuclear absorber. From the jet speeds it seems that it depends not only on the orientation whether an AGN appears as a FR II radio galaxy or a quasar (Barthel 1989), but there are also differences in the power of the jets that might be triggered by the accretion rate and/or the spin of the black hole (e.g., Meier 2002). However, there are hints that the jets in radio galaxies exhibit a highly relativistic spine ($\gamma \geq 10$) in their centre and a surrounding slower but still relativistic layer (Giovannini et al. (1999); Laing et al. (1999); Swain et al. (1998)). In this case we are not able to detect the fast spine at large viewing angles due to the relativistic beaming, but observe the more moderate outer layers and the orientation depend unification of FR II radio galaxies and quasars can be still valid.

Table 6.9: Results from Gaussian Model fitting and component parameters.

Epoch	ν [GHz]	S [mJy]	r [mas]	ϕ [°]	θ [mas]	Id.[a]
1995.27	15.4	0.010 ± 0.001	5.19 ± 0.37	104 ± 1	1.39 ± 0.14	C03
	15.4	0.005 ± 0.001	2.27 ± 0.25	104 ± 2	0.03 ± 0.01	C04
	15.4	0.073 ± 0.007	–	–	0.42 ± 0.01	N
	15.4	0.368 ± 0.037	0.57 ± 0.08	-75 ± 11	0.26 ± 0.01	J10
	15.4	0.292 ± 0.029	0.96 ± 0.05	-75 ± 6	0.12 ± 0.01	X
	15.4	0.362 ± 0.036	1.31 ± 0.08	-81 ± 5	0.25 ± 0.01	J09
	15.4	0.231 ± 0.023	1.73 ± 0.08	-83 ± 3	0.28 ± 0.01	J08
	15.4	0.069 ± 0.007	2.31 ± 0.08	-81 ± 2	0.41 ± 0.01	J07
	15.4	0.062 ± 0.006	3.09 ± 0.09	-80 ± 2	0.45 ± 0.01	J06
	15.4	0.023 ± 0.002	6.80 ± 0.30	-75 ± 1	2.05 ± 0.09	J04
1995.95	15.4	0.009 ± 0.001	5.40 ± 0.35	102 ± 1	1.05 ± 0.12	C03
	15.4	0.012 ± 0.001	2.11 ± 0.15	107 ± 3	0.27 ± 0.02	C04
	15.4	0.055 ± 0.005	–	–	0.24 ± 0.01	N
	15.4	0.654 ± 0.065	0.84 ± 0.10	-75 ± 7	0.37 ± 0.01	J10
	15.4	0.463 ± 0.046	1.41 ± 0.10	-67 ± 4	0.38 ± 0.01	J09
	15.4	0.361 ± 0.036	1.92 ± 0.10	-78 ± 3	0.42 ± 0.01	J08
	15.4	0.065 ± 0.006	2.60 ± 0.08	-79 ± 2	0.46 ± 0.01	J07
	15.4	0.076 ± 0.008	3.42 ± 0.09	-78 ± 1	0.59 ± 0.01	J06
	15.4	0.023 ± 0.002	6.03 ± 0.26	-76 ± 1	1.52 ± 0.07	J05
	15.4	0.014 ± 0.001	18.80 ± 0.42	-75 ± 0	2.54 ± 0.18	X
1996.38	15.4	0.009 ± 0.001	6.41 ± 0.23	109 ± 1	0.50 ± 0.06	C03
	15.4	0.011 ± 0.001	2.68 ± 0.24	106 ± 2	0.67 ± 0.06	C04
	15.4	0.006 ± 0.001	1.50 ± 0.27	108 ± 4	0.40 ± 0.07	C05
	15.4	0.045 ± 0.004	–	–	0.36 ± 0.01	N
	15.4	0.242 ± 0.024	0.63 ± 0.10	-75 ± 10	0.37 ± 0.01	J11
	15.4	0.337 ± 0.034	0.95 ± 0.10	-75 ± 6	0.38 ± 0.01	J10
	15.4	0.388 ± 0.039	1.46 ± 0.11	-74 ± 4	0.49 ± 0.01	J09
	15.4	0.254 ± 0.025	1.99 ± 0.11	-79 ± 3	0.48 ± 0.01	J08
	15.4	0.047 ± 0.005	2.61 ± 0.09	-81 ± 2	0.40 ± 0.01	J07
	15.4	0.064 ± 0.006	3.39 ± 0.10	-77 ± 1	0.68 ± 0.01	J06
	15.4	0.031 ± 0.003	6.39 ± 0.24	-75 ± 1	1.76 ± 0.06	J05
1996.73	15.4	0.004 ± 0.001	5.27 ± 0.26	104 ± 1	0.30 ± 0.07	C03
	15.4	0.005 ± 0.001	2.87 ± 0.36	112 ± 2	0.72 ± 0.13	C04
	15.4	0.008 ± 0.001	2.04 ± 0.18	107 ± 3	0.25 ± 0.03	C05
	15.4	0.062 ± 0.006	–	–	0.41 ± 0.01	N
	15.4	0.438 ± 0.044	0.69 ± 0.08	-75 ± 9	0.26 ± 0.01	J11
	15.4	0.330 ± 0.033	1.02 ± 0.07	-170 ± 6	0.22 ± 0.01	J10
	15.4	0.377 ± 0.038	1.39 ± 0.09	-69 ± 4	0.30 ± 0.01	J09
	15.4	0.308 ± 0.031	1.90 ± 0.09	-78 ± 3	0.33 ± 0.01	J08
	15.4	0.086 ± 0.009	2.51 ± 0.10	-79 ± 2	0.43 ± 0.01	J07
	15.4	0.064 ± 0.006	3.35 ± 0.09	-78 ± 2	0.54 ± 0.01	J06
	15.4	0.012 ± 0.001	4.39 ± 0.28	-78 ± 1	0.93 ± 0.08	X
	15.4	0.020 ± 0.002	6.29 ± 0.20	-78 ± 1	0.83 ± 0.04	J05
	15.4	0.009 ± 0.001	17.89 ± 0.40	-74 ± 0	1.48 ± 0.16	J01
1996.73	22.2	0.005 ± 0.001	6.75 ± 0.38	106 ± 1	0.67 ± 0.14	C03
	22.2	0.010 ± 0.001	2.12 ± 0.19	108 ± 3	0.37 ± 0.04	C05
	22.2	0.008 ± 0.001	0.82 ± 0.10	102 ± 7	0.08 ± 0.01	C06

Table 6.9 – continued from previous page

Epoch	ν [GHz]	S [mJy]	r [mas]	ϕ [°]	θ [mas]	Id.[a]
	22.2	0.083 ± 0.008	–	–	0.34 ± 0.01	N
	22.2	0.400 ± 0.040	0.64 ± 0.06	-75 ± 10	0.14 ± 0.01	J11
	22.2	0.433 ± 0.043	0.96 ± 0.07	-89 ± 6	0.20 ± 0.01	J10
	22.2	0.236 ± 0.024	1.45 ± 0.08	-72 ± 4	0.23 ± 0.01	J09
	22.2	0.196 ± 0.020	1.96 ± 0.09	-78 ± 3	0.29 ± 0.01	J08
	22.2	0.057 ± 0.006	2.46 ± 0.07	-79 ± 2	0.31 ± 0.01	J07
	22.2	0.049 ± 0.005	3.38 ± 0.12	-77 ± 1	0.65 ± 0.01	J06
	22.2	0.012 ± 0.001	6.08 ± 0.24	-79 ± 1	0.71 ± 0.06	J05
1996.73	43.2	0.024 ± 0.002	0.71 ± 0.09	107 ± 9	0.19 ± 0.01	C06
	43.2	0.054 ± 0.005	–	–	0.19 ± 0.01	N
	43.2	0.206 ± 0.021	0.51 ± 0.04	-75 ± 12	0.08 ± 0.01	X
	43.2	0.283 ± 0.028	0.66 ± 0.02	-75 ± 9	0.02 ± 0.01	J11
	43.2	0.264 ± 0.026	0.94 ± 0.08	-76 ± 6	0.24 ± 0.01	J10
	43.2	0.097 ± 0.010	1.46 ± 0.09	-76 ± 4	0.33 ± 0.01	J09
	43.2	0.058 ± 0.006	2.03 ± 0.04	-78 ± 3	0.12 ± 0.01	J08
	43.2	0.030 ± 0.003	2.42 ± 0.12	-78 ± 2	0.41 ± 0.01	J07
1996.82	15.4	0.014 ± 0.001	2.05 ± 0.29	105 ± 3	1.18 ± 0.09	C05
	15.4	0.029 ± 0.003	–	–	0.35 ± 0.01	N
	15.4	0.225 ± 0.022	0.71 ± 0.08	-75 ± 9	0.25 ± 0.01	J11
	15.4	0.382 ± 0.038	1.06 ± 0.09	-75 ± 6	0.32 ± 0.01	J10
	15.4	0.273 ± 0.027	1.58 ± 0.10	-68 ± 4	0.37 ± 0.01	J09
	15.4	0.204 ± 0.020	2.07 ± 0.10	-78 ± 3	0.40 ± 0.01	J08
	15.4	0.036 ± 0.004	2.76 ± 0.10	-80 ± 2	0.39 ± 0.01	J07
	15.4	0.035 ± 0.004	3.58 ± 0.12	-76 ± 1	0.53 ± 0.01	J06
1997.66	15.4	0.010 ± 0.001	5.74 ± 0.43	105 ± 1	1.81 ± 0.19	C03
	15.4	0.015 ± 0.002	2.16 ± 0.21	107 ± 3	0.68 ± 0.05	C05
	15.4	0.042 ± 0.004	–	–	0.41 ± 0.01	N
	15.4	0.461 ± 0.046	0.76 ± 0.09	-75 ± 8	0.33 ± 0.01	J11
	15.4	0.515 ± 0.051	1.24 ± 0.09	-85 ± 5	0.35 ± 0.01	J10
	15.4	0.252 ± 0.025	1.77 ± 0.10	-73 ± 3	0.40 ± 0.01	J09
	15.4	0.149 ± 0.015	2.30 ± 0.10	-78 ± 2	0.38 ± 0.01	J08
	15.4	0.073 ± 0.007	2.98 ± 0.08	-79 ± 2	0.44 ± 0.01	J07
	15.4	0.048 ± 0.005	3.65 ± 0.10	-77 ± 1	0.51 ± 0.01	J06
	15.4	0.007 ± 0.001	4.97 ± 0.27	-78 ± 1	0.52 ± 0.07	X
	15.4	0.019 ± 0.002	6.54 ± 0.18	-79 ± 1	0.63 ± 0.03	J05
	15.4	0.004 ± 0.001	7.90 ± 0.39	-75 ± 0	0.57 ± 0.15	J04
	15.4	0.015 ± 0.002	18.20 ± 0.40	-75 ± 0	2.27 ± 0.16	J01
1998.21	15.4	0.009 ± 0.001	5.66 ± 0.39	108 ± 1	1.38 ± 0.15	C03
	15.4	0.010 ± 0.001	2.23 ± 0.11	110 ± 2	0.12 ± 0.01	C05
	15.4	0.003 ± 0.001	0.82 ± 0.29	109 ± 7	0.25 ± 0.09	C06
	15.4	0.043 ± 0.004	–	–	0.36 ± 0.01	N
	15.4	0.229 ± 0.023	0.56 ± 0.07	-75 ± 11	0.21 ± 0.01	J12
	15.4	0.454 ± 0.045	0.91 ± 0.09	-75 ± 7	0.32 ± 0.01	J11
	15.4	0.412 ± 0.041	1.37 ± 0.09	-82 ± 4	0.33 ± 0.01	J10
	15.4	0.182 ± 0.018	1.98 ± 0.09	-76 ± 3	0.34 ± 0.01	J09
	15.4	0.107 ± 0.011	2.57 ± 0.08	-78 ± 2	0.28 ± 0.01	J08
	15.4	0.053 ± 0.005	3.15 ± 0.05	-77 ± 2	0.16 ± 0.01	J07
	15.4	0.041 ± 0.004	3.70 ± 0.10	-77 ± 1	0.39 ± 0.01	J06
	15.4	0.022 ± 0.002	6.59 ± 0.20	-78 ± 1	0.90 ± 0.04	J05
1999.38	15.4	0.009 ± 0.001	5.60 ± 0.35	105 ± 1	1.09 ± 0.13	C03

Continued on next page

Table 6.9 – continued from previous page

Epoch	ν [GHz]	S [mJy]	r [mas]	ϕ [°]	θ [mas]	Id.[a]
	15.4	0.015 ± 0.002	2.21 ± 0.20	109 ± 3	0.57 ± 0.04	C05
	15.4	0.005 ± 0.001	1.19 ± 0.35	106 ± 5	0.62 ± 0.12	C06
	15.4	0.040 ± 0.004	–	–	0.23 ± 0.01	N
	15.4	0.407 ± 0.041	0.77 ± 0.09	-75 ± 8	0.33 ± 0.01	J12
	15.4	0.407 ± 0.041	1.12 ± 0.10	-77 ± 5	0.36 ± 0.01	J11
	15.4	0.449 ± 0.045	1.59 ± 0.10	-81 ± 4	0.39 ± 0.01	J10
	15.4	0.131 ± 0.013	2.27 ± 0.11	-78 ± 2	0.45 ± 0.01	J09
	15.4	0.047 ± 0.005	2.77 ± 0.07	-80 ± 2	0.26 ± 0.01	J08
	15.4	0.103 ± 0.010	3.17 ± 0.11	-79 ± 2	0.50 ± 0.01	J07
	15.4	0.042 ± 0.004	3.89 ± 0.13	-77 ± 1	0.69 ± 0.02	J06
	15.4	0.021 ± 0.002	6.77 ± 0.20	-78 ± 1	0.83 ± 0.04	J05
2001.17	15.4	0.011 ± 0.001	5.97 ± 0.45	107 ± 1	2.11 ± 0.20	C03
	15.4	0.007 ± 0.001	2.39 ± 0.26	109 ± 2	0.43 ± 0.07	C05
	15.4	0.011 ± 0.001	1.58 ± 0.25	107 ± 4	0.68 ± 0.06	C06
	15.4	0.046 ± 0.005	–	–	0.26 ± 0.01	N
	15.4	0.226 ± 0.023	0.72 ± 0.07	-75 ± 9	0.22 ± 0.01	J13
	15.4	0.293 ± 0.029	1.02 ± 0.09	-75 ± 6	0.31 ± 0.01	J12
	15.4	0.501 ± 0.050	1.39 ± 0.10	-81 ± 4	0.38 ± 0.01	J11
	15.4	0.221 ± 0.022	1.90 ± 0.10	-85 ± 3	0.43 ± 0.01	J10
	15.4	0.067 ± 0.007	2.59 ± 0.08	-80 ± 2	0.41 ± 0.01	J09
	15.4	0.095 ± 0.009	3.37 ± 0.12	-79 ± 1	0.57 ± 0.01	J08
	15.4	0.028 ± 0.003	3.99 ± 0.17	-79 ± 1	0.76 ± 0.03	J07
	15.4	0.021 ± 0.002	6.98 ± 0.25	-78 ± 0	1.36 ± 0.07	J05
2001.97	15.4	0.003 ± 0.001	5.65 ± 0.30	107 ± 1	0.23 ± 0.09	C03
	15.4	0.010 ± 0.001	2.29 ± 0.23	108 ± 2	0.50 ± 0.05	C05
	15.4	0.007 ± 0.001	1.64 ± 0.13	107 ± 4	0.12 ± 0.02	C06
	15.4	0.050 ± 0.005	–	–	0.33 ± 0.01	N
	15.4	0.327 ± 0.033	0.74 ± 0.08	-75 ± 8	0.28 ± 0.01	J14
	15.4	0.140 ± 0.014	0.99 ± 0.08	-75 ± 6	0.24 ± 0.01	J13
	15.4	0.445 ± 0.044	1.37 ± 0.10	-75 ± 4	0.41 ± 0.01	J12
	15.4	0.243 ± 0.024	1.77 ± 0.10	-82 ± 3	0.43 ± 0.01	J11
	15.4	0.073 ± 0.007	2.48 ± 0.08	-80 ± 2	0.47 ± 0.01	J10
	15.4	0.056 ± 0.006	3.24 ± 0.10	-79 ± 2	0.51 ± 0.01	J09
	15.4	0.057 ± 0.006	3.70 ± 0.09	-79 ± 1	0.46 ± 0.01	J08
	15.4	0.011 ± 0.001	4.70 ± 0.34	-79 ± 1	1.18 ± 0.11	J06
	15.4	0.020 ± 0.002	6.98 ± 0.21	-78 ± 0	0.88 ± 0.04	J05
	15.4	0.003 ± 0.001	13.62 ± 0.54	-82 ± 0	0.95 ± 0.29	J03
2002.03	4.9	0.013 ± 0.001	15.03 ± 0.65	106 ± 0	5.53 ± 0.42	C02
	4.9	0.014 ± 0.001	6.59 ± 0.41	106 ± 1	2.45 ± 0.17	C03
	4.9	0.348 ± 0.035	–	–	1.78 ± 0.01	N
	4.9	0.374 ± 0.037	3.31 ± 0.22	-80 ± 2	1.90 ± 0.01	J08
	4.9	0.045 ± 0.004	6.57 ± 0.19	-78 ± 1	1.68 ± 0.04	J05
	4.9	0.029 ± 0.003	8.67 ± 0.29	-73 ± 0	2.44 ± 0.09	J04
	4.9	0.015 ± 0.002	12.91 ± 0.47	-75 ± 0	3.25 ± 0.22	J03
	4.9	0.024 ± 0.002	17.58 ± 0.34	-74 ± 0	2.77 ± 0.12	J02
	4.9	0.011 ± 0.001	21.27 ± 0.54	-73 ± 0	3.09 ± 0.29	J01
	4.9	0.007 ± 0.001	47.12 ± 0.70	-75 ± 0	3.30 ± 0.48	J00
2002.03	15.4	0.011 ± 0.001	5.80 ± 0.37	105 ± 1	1.50 ± 0.14	C03
	15.4	0.007 ± 0.001	2.25 ± 0.22	108 ± 2	0.35 ± 0.05	C05
	15.4	0.012 ± 0.001	1.61 ± 0.19	108 ± 4	0.42 ± 0.04	C06

Continued on next page

Table 6.9 – continued from previous page

Epoch	ν [GHz]	S [mJy]	r [mas]	ϕ [°]	θ [mas]	Id.[a]
	15.4	0.049 ± 0.005	–	–	0.24 ± 0.01	N
	15.4	0.291 ± 0.029	0.73 ± 0.08	-75 ± 8	0.27 ± 0.01	J14
	15.4	0.180 ± 0.018	1.01 ± 0.07	-75 ± 6	0.21 ± 0.01	J13
	15.4	0.470 ± 0.047	1.41 ± 0.10	-63 ± 4	0.39 ± 0.01	J12
	15.4	0.237 ± 0.024	1.79 ± 0.10	-85 ± 3	0.42 ± 0.01	J11
	15.4	0.062 ± 0.006	2.36 ± 0.07	-81 ± 2	0.34 ± 0.01	J10
	15.4	0.045 ± 0.004	2.84 ± 0.10	-79 ± 2	0.41 ± 0.01	J09
	15.4	0.105 ± 0.011	3.57 ± 0.12	-79 ± 1	0.58 ± 0.01	J08
	15.4	0.007 ± 0.001	4.77 ± 0.22	-78 ± 1	0.32 ± 0.05	J06
	15.4	0.025 ± 0.003	7.03 ± 0.22	-78 ± 0	1.24 ± 0.05	J05
	15.4	0.012 ± 0.001	17.94 ± 0.49	-75 ± 0	2.94 ± 0.24	J02
2002.51	4.9	0.014 ± 0.001	14.92 ± 0.65	105 ± 0	5.87 ± 0.42	C02
	4.9	0.012 ± 0.001	6.64 ± 0.42	105 ± 1	2.11 ± 0.18	C03
	4.9	0.375 ± 0.037	–	–	1.59 ± 0.01	N
	4.9	0.400 ± 0.040	3.44 ± 0.21	-78 ± 1	1.84 ± 0.01	J08
	4.9	0.058 ± 0.006	6.87 ± 0.17	-78 ± 1	1.73 ± 0.03	J05
	4.9	0.028 ± 0.003	9.16 ± 0.31	-73 ± 0	2.65 ± 0.10	J04
	4.9	0.013 ± 0.001	14.18 ± 0.48	-74 ± 0	2.92 ± 0.23	J03
	4.9	0.029 ± 0.003	18.42 ± 0.33	-73 ± 0	3.09 ± 0.11	J02
	4.9	0.010 ± 0.001	47.80 ± 0.69	-74 ± 0	5.02 ± 0.48	J00
2002.51	15.4	0.006 ± 0.001	5.52 ± 0.39	106 ± 1	0.88 ± 0.15	C03
	15.4	0.007 ± 0.001	2.49 ± 0.28	109 ± 2	0.54 ± 0.08	C05
	15.4	0.013 ± 0.001	1.68 ± 0.18	108 ± 3	0.45 ± 0.03	C06
	15.4	0.052 ± 0.005	–	–	0.17 ± 0.01	N
	15.4	0.088 ± 0.009	0.61 ± 0.05	-75 ± 10	0.11 ± 0.01	X
	15.4	0.336 ± 0.034	0.87 ± 0.08	-75 ± 7	0.24 ± 0.01	J14
	15.4	0.194 ± 0.019	1.23 ± 0.08	-56 ± 5	0.28 ± 0.01	J13
	15.4	0.470 ± 0.047	1.62 ± 0.10	-79 ± 4	0.42 ± 0.01	J12
	15.4	0.118 ± 0.012	1.97 ± 0.09	-87 ± 3	0.29 ± 0.01	J11
	15.4	0.069 ± 0.007	2.55 ± 0.07	-81 ± 2	0.36 ± 0.01	J10
	15.4	0.050 ± 0.005	3.20 ± 0.10	-80 ± 2	0.46 ± 0.01	J09
	15.4	0.074 ± 0.007	3.77 ± 0.08	-79 ± 1	0.52 ± 0.01	J08
	15.4	0.009 ± 0.001	5.14 ± 0.30	-79 ± 1	0.80 ± 0.09	J06
	15.4	0.022 ± 0.002	7.15 ± 0.22	-78 ± 0	1.05 ± 0.05	J05
	15.4	0.013 ± 0.001	17.64 ± 0.59	-74 ± 0	4.43 ± 0.35	J02
2002.88	15.4	0.007 ± 0.001	5.51 ± 0.42	115 ± 1	1.29 ± 0.18	C03
	15.4	0.012 ± 0.001	2.26 ± 0.15	108 ± 2	0.27 ± 0.02	C05
	15.4	0.006 ± 0.001	1.58 ± 0.13	108 ± 4	0.11 ± 0.02	C06
	15.4	0.063 ± 0.006	–	–	0.04 ± 0.01	N
	15.4	0.443 ± 0.044	0.79 ± 0.07	-75 ± 8	0.21 ± 0.01	J14
	15.4	0.223 ± 0.022	1.21 ± 0.07	-54 ± 5	0.20 ± 0.01	J13
	15.4	0.484 ± 0.048	1.71 ± 0.10	-75 ± 3	0.40 ± 0.01	J12
	15.4	0.084 ± 0.008	2.02 ± 0.05	-87 ± 3	0.11 ± 0.01	J11
	15.4	0.047 ± 0.005	2.63 ± 0.06	-80 ± 2	0.19 ± 0.01	J10
	15.4	0.076 ± 0.008	3.33 ± 0.08	-79 ± 2	0.48 ± 0.01	J09
	15.4	0.045 ± 0.004	3.87 ± 0.09	-79 ± 1	0.39 ± 0.01	J08
	15.4	0.009 ± 0.001	5.29 ± 0.25	-79 ± 1	0.56 ± 0.06	J06
	15.4	0.019 ± 0.002	7.00 ± 0.18	-78 ± 0	0.63 ± 0.03	J05
2003.04	15.4	0.003 ± 0.001	5.38 ± 0.16	106 ± 1	0.07 ± 0.03	C03
	15.4	0.009 ± 0.001	2.53 ± 0.35	110 ± 2	1.05 ± 0.12	C05

Continued on next page

Table 6.9 – continued from previous page

Epoch	ν [GHz]	S [mJy]	r [mas]	ϕ [°]	θ [mas]	Id.[a]
	15.4	0.013 ± 0.001	1.84 ± 0.21	108 ± 3	0.54 ± 0.04	C06
	15.4	0.043 ± 0.004	–	–	0.23 ± 0.01	N
	15.4	0.315 ± 0.031	0.77 ± 0.08	-75 ± 8	0.26 ± 0.01	J14
	15.4	0.147 ± 0.015	1.09 ± 0.08	-98 ± 6	0.24 ± 0.01	J13
	15.4	0.226 ± 0.023	1.53 ± 0.10	-68 ± 4	0.38 ± 0.01	J12
	15.4	0.329 ± 0.033	1.85 ± 0.10	-83 ± 3	0.41 ± 0.01	J11
	15.4	0.066 ± 0.007	2.67 ± 0.08	-81 ± 2	0.44 ± 0.01	J10
	15.4	0.067 ± 0.007	3.47 ± 0.09	-80 ± 1	0.57 ± 0.01	J09
	15.4	0.036 ± 0.004	4.04 ± 0.13	-78 ± 1	0.63 ± 0.02	J08
	15.4	0.022 ± 0.002	6.97 ± 0.24	-78 ± 0	1.27 ± 0.06	J05
2003.04	22.2	0.004 ± 0.001	2.62 ± 0.23	112 ± 2	0.24 ± 0.05	C05
	22.2	0.017 ± 0.002	1.73 ± 0.15	109 ± 3	0.37 ± 0.02	C06
	22.2	0.096 ± 0.010	–	–	0.30 ± 0.01	N
	22.2	0.425 ± 0.043	0.73 ± 0.07	-75 ± 8	0.21 ± 0.01	J14
	22.2	0.171 ± 0.017	1.08 ± 0.07	-76 ± 6	0.21 ± 0.01	J13
	22.2	0.337 ± 0.034	1.70 ± 0.11	-73 ± 3	0.45 ± 0.01	J12
	22.2	0.084 ± 0.008	1.99 ± 0.08	-84 ± 3	0.25 ± 0.01	J11
	22.2	0.064 ± 0.006	2.74 ± 0.09	-79 ± 2	0.52 ± 0.01	J10
	22.2	0.051 ± 0.005	3.71 ± 0.10	-79 ± 1	0.48 ± 0.01	J09
	22.2	0.007 ± 0.001	4.59 ± 0.21	-78 ± 1	0.32 ± 0.04	X
	22.2	0.008 ± 0.001	7.08 ± 0.17	-76 ± 0	0.23 ± 0.03	J05
2003.24	4.9	0.006 ± 0.001	21.10 ± 0.87	106 ± 0	4.27 ± 0.75	C01
	4.9	0.010 ± 0.001	14.42 ± 0.62	106 ± 0	3.68 ± 0.38	C02
	4.9	0.015 ± 0.002	6.67 ± 0.41	105 ± 1	2.44 ± 0.17	C03
	4.9	0.431 ± 0.043	–	–	1.56 ± 0.01	N
	4.9	0.384 ± 0.038	3.56 ± 0.23	-74 ± 1	2.02 ± 0.01	J08
	4.9	0.074 ± 0.007	6.98 ± 0.16	-78 ± 0	1.96 ± 0.03	J05
	4.9	0.024 ± 0.002	9.17 ± 0.31	-74 ± 0	2.31 ± 0.10	J04
	4.9	0.015 ± 0.002	14.15 ± 0.45	-74 ± 0	3.11 ± 0.20	J03
	4.9	0.023 ± 0.002	18.11 ± 0.34	-74 ± 0	2.57 ± 0.11	J02
	4.9	0.009 ± 0.001	21.93 ± 0.61	-74 ± 0	3.37 ± 0.38	J01
	4.9	0.009 ± 0.001	48.17 ± 0.77	-74 ± 0	5.27 ± 0.59	J00
2003.24	15.4	0.004 ± 0.001	2.88 ± 0.25	109 ± 2	0.26 ± 0.06	C05
	15.4	0.019 ± 0.002	1.84 ± 0.17	108 ± 3	0.54 ± 0.03	C06
	15.4	0.073 ± 0.007	–	–	0.28 ± 0.01	N
	15.4	0.187 ± 0.019	0.67 ± 0.07	-75 ± 9	0.21 ± 0.01	X
	15.4	0.271 ± 0.027	0.91 ± 0.08	-75 ± 7	0.25 ± 0.01	J14
	15.4	0.174 ± 0.017	1.35 ± 0.09	-66 ± 4	0.31 ± 0.01	J13
	15.4	0.095 ± 0.009	1.73 ± 0.07	-63 ± 3	0.20 ± 0.01	J12
	15.4	0.353 ± 0.035	1.85 ± 0.10	-83 ± 3	0.40 ± 0.01	J11
	15.4	0.063 ± 0.006	2.64 ± 0.08	-81 ± 2	0.43 ± 0.01	J10
	15.4	0.058 ± 0.006	3.35 ± 0.09	-79 ± 2	0.47 ± 0.01	J09
	15.4	0.052 ± 0.005	3.87 ± 0.10	-79 ± 1	0.55 ± 0.01	J08
	15.4	0.009 ± 0.001	5.38 ± 0.31	-78 ± 1	0.87 ± 0.10	J06
	15.4	0.021 ± 0.002	7.10 ± 0.21	-78 ± 0	0.92 ± 0.04	J05
2003.27	15.4	0.008 ± 0.001	5.81 ± 0.41	104 ± 1	1.39 ± 0.17	C03
	15.4	0.003 ± 0.001	2.87 ± 0.28	104 ± 2	0.25 ± 0.08	C05
	15.4	0.020 ± 0.002	1.88 ± 0.17	106 ± 3	0.56 ± 0.03	C06
	15.4	0.050 ± 0.005	–	–	0.32 ± 0.01	N
	15.4	0.274 ± 0.027	0.71 ± 0.07	-75 ± 9	0.21 ± 0.01	J15

Continued on next page

Table 6.9 – continued from previous page

Epoch	ν [GHz]	S [mJy]	r [mas]	ϕ [°]	θ [mas]	Id.[a]
	15.4	0.232 ± 0.023	1.03 ± 0.07	-75 ± 6	0.21 ± 0.01	J14
	15.4	0.278 ± 0.028	1.49 ± 0.10	-75 ± 4	0.36 ± 0.01	X
	15.4	0.457 ± 0.046	1.85 ± 0.10	-75 ± 3	0.41 ± 0.01	J11
	15.4	0.096 ± 0.010	2.69 ± 0.11	-96 ± 2	0.45 ± 0.01	J10
	15.4	0.068 ± 0.007	3.40 ± 0.08	-84 ± 1	0.41 ± 0.01	J09
	15.4	0.062 ± 0.006	3.93 ± 0.09	-80 ± 1	0.55 ± 0.01	J08
	15.4	0.012 ± 0.001	5.32 ± 0.29	-78 ± 1	1.01 ± 0.08	J06
	15.4	0.027 ± 0.003	7.22 ± 0.20	-79 ± 0	1.04 ± 0.04	J05
	15.4	0.010 ± 0.001	18.19 ± 0.48	-74 ± 0	2.25 ± 0.23	J02
2003.27	43.2	0.063 ± 0.006	–	–	0.28 ± 0.01	N
	43.2	0.280 ± 0.028	0.60 ± 0.05	-75 ± 10	0.08 ± 0.01	X
	43.2	0.160 ± 0.016	0.78 ± 0.06	-105 ± 8	0.15 ± 0.01	J15
	43.2	0.085 ± 0.009	1.21 ± 0.10	-78 ± 5	0.39 ± 0.01	J14
	43.2	0.046 ± 0.005	1.77 ± 0.06	-71 ± 3	0.18 ± 0.01	J13
	43.2	0.082 ± 0.008	1.97 ± 0.09	-82 ± 3	0.35 ± 0.01	J11
	43.2	0.013 ± 0.001	2.83 ± 0.09	-80 ± 2	0.11 ± 0.01	J10
	43.2	0.015 ± 0.002	3.58 ± 0.13	-78 ± 1	0.26 ± 0.02	J09
2003.27	86.2	0.013 ± 0.001	–	–	0.04 ± 0.01	N
	86.2	0.294 ± 0.029	0.61 ± 0.03	-179 ± 10	0.04 ± 0.01	J15
	86.2	0.067 ± 0.007	0.88 ± 0.06	-81 ± 7	0.24 ± 0.01	J14
	86.2	0.008 ± 0.001	1.20 ± 0.09	-88 ± 5	0.01 ± 0.01	J13
	86.2	0.031 ± 0.003	1.80 ± 0.07	-77 ± 3	0.14 ± 0.01	J11
	86.2	0.011 ± 0.001	2.61 ± 0.11	-80 ± 2	0.15 ± 0.01	J10

[a] Identification of the individual components. If a component appeared only in a single epoch it is labelled with X.

Chapter 7

Summary

We analysed 51 epochs of VLBI data at frequencies between (5, 8, 15, 22, 43 and 86) GHz of the blazar S5 0716+714 (28 epochs) and Cygnus A (23 epochs). The kinematical properties of the jets were derived using Gaussian modelfit components and the multi-frequency data were used to calculate spectral index maps. Where single-dish measurements were available we used them to compare the results with the VLBI structure.

In the case of 0716+714 we measured speeds of $5\,c$ to $16\,c$ assuming a redshift of 0.3. These speeds are atypically fast for a BL Lac object. To match the observed range of apparent speeds without too much bending the most likely jet parameters are a Lorentz factor of > 16 and a viewing angle of $< 2°$. Under these circumstances Doppler factors between 16 and 32 are possible and can be used to explain apparent brightness temperatures of up to 10^{17} K derived from IDV. If the occasionally observed outbursts at cm wavelengths have an intrinsic origin, they suggest brightness temperatures of up to 10^{19} K and might be due to more local phenomena, but our data are not sufficiently frequent sampled to look for acceleration. Possible non-linear motion or a slightly different identification of modelfit components can also explain the higher motion found by Jorstad et al. (2001) over a three year time period. In this context it is also interesting that there are indications for a periodic variation of the ejection angle of $\sim 6°$ in about seven years that might be due to precession and/or a helical jet structure. We found a weak correlation between the ejection dates of new components and the spectral index between $5\,\mathrm{GHz}$ and $15\,\mathrm{GHz}$ suggesting that the components are indeed shocks that expand as they travel down the jet.

From polarimetric space VLBI observation at $5\,\mathrm{GHz}$ it was found that the jet magnetic field is perpendicular to the jet axis as is expected for optically thin emission. The different orientation of electric vectors in the core region can be explained by an optical depth effect or by jet bending in the inner core region. High-resolution images showing the jet at separation $< 1\,\mathrm{mas}$ reveal that the jet follows the rotation of the EVPA and therefore bending is most likely the cause for the different orientations. A misalignment between the parsec-scale and the

kiloparsec-scale structure is typical for BL Lacs (Pearson & Readhead 1988; Wehrle et al. 1992) and is also present in 0716+714 (Figure 3.1, p. 18). The new observations suggest that these structural changes continue even on sub-parsec-scales. Possible explanations for such a misalignment are a helical jet, which is oriented towards us (Conway & Murphy 1993), or interaction with the surrounding medium. A helical jet would also explain the variations of the P.A. in the inner jet of 0716+714. Dependent on the resolution of the observations the first jet component would appear closer or further away from the core and due to the helical structure would also appear at different position angles. Our actual data set is too inhomogeneous to test this hypothesis, but with larger data sets at a constant resolution, which will become available from surveys like the VLBA 2 cm Survey (Kellermann et al. 2004, 1998; Zensus et al. 2002) in some years, this will become possible.

Total intensity variations of about 5 % and extrem linear polarization variations of up to 40 % on time-scales as short as 10 h were observed in the VSOP maps and also with single-dish measurements in Effelsberg. Comparing the VLBI images from three closely separated epochs with the simultaneous flux-density variations measured at Effelsberg proved for the first time that the IDV is caused by the VLBI core components in 0716+714 and not further out as previously suggested (Gabuzda et al. 2000a). No rapid variability was found in the outer jet structure. The high resolution VSOP images showed that the VLBI-core is a composite of sub-components smaller than 0.1 mas. From this we derive a brightness temperature of 2×10^{12} K, which implies that the emission is enhanced by a Doppler factor of about 2. Assuming an intrinsic origin for the variability, brightness temperatures of up to 10^{16} K are calculated from the linear polarisation variations and Doppler factors of about 25 are required to bring these temperatures down to the inverse-Compton limit. But given that we measure such small source sizes inter stellar scattering has also to play a role.

Unfortunately, because of the unknown redshift, the derived speeds and brightness temperatures are only lower limits if the source is further away and will become smaller if 0716+714 is closer as $z = 0.3$. But, since it is more likely that 0716+714 has a higher redshift (Wagner priv. comm.), it seems to be, even for a blazar, an extreme source where we see nearly into the jet, and that exhibits very compact regions of high activity at the footpoint of the jet. Future high-resolution studies that are able to resolve the sub-components in the core will show if the components vary independently and how the variablity changes with frequency, which can be used to separate intrinsic and extrinsic variablity effects. Ongoing broad-band studies from radio wavelengths to γ-rays will help to further constrain the different models.

The analysis of VLBI data of Cygnus A dating back to 1995 revealed new insights to the kinematics of the jets and the spectral properties of the nuclear region. The analysis of the multi-frequency data revealed a complex spectrum around the core that is in some parts highly inverted, with $\alpha_{5/15} \approx 3$. Together with the frequency dependence of the jet to counter-jet ratio and further indications from radio wavelengths to X-rays, there is strong evidence that this is due to free-free absorption by an obscuring torus. Although, we do not directly see

the torus and can not precisely measure its geometry, the observations suggest that the absorber is oriented perpendicular to the jet axis has an half opening angle of about $60\,°$ and has an maximum extent of about $30\,\mathrm{pc}$. It seems to effectively block the $5\,\mathrm{GHz}$ emission in the inner $\sim 4\,\mathrm{pc}$ and the optical depth decreases further out.

Apparent speeds of $0.5\,c$ to $1\,c$ in the jet and $0.3\,c$ to $0.6\,c$ on the counter-jet side were measured. The apparent acceleration in the jet and the large differences in the measured motions on the counter-jet side might reflect a more complicated jet structure than that of the simple Königl jet with a well defined jet flow and questions the assumption that the jet and counter-jet have intrinsically the same properties. The differences of the jet and the counter-jet speeds might be caused by a stratification of the jet, where we observe different velocity sheaths depending on the optical depth and the orientation of the jet. The most likely jet parameters are a jet Lorentz factor of about 2 (corresponding to $\beta \approx 0.9\,c$) and an angle to the line of sight of $70°$ to $80°$. Jet Lorentz factors of 1.5 to 2 and Doppler factors of about 1 seem to be typical for radio galaxies and are significantly lower than those from radio-loud quasars with typical values of 10 (Lähteenmäki & Valtaoja 1999).

With regard to the unified scheme, Cygnus A seems to support the idea that type 2 AGN, which do not show broad emission lines, are indeed seen from large viewing angles and the BLR is shielded behind a circum nuclear absorber. From the jet speeds it seems that the appearance of an AGN as a FR II radio galaxy or a quasar (Barthel 1989) depends not only on the orientation but also on differences in the power of the jets that might be in turn dependent on the accretion rate and/or the spin of the black hole (e.g., Meier 2002). However, there are hints that the jets in radio galaxies exhibit a highly relativistic spine ($\gamma \geq 10$) in their centre and a surrounding slower but still relativistic layer (Giovannini et al. (1999); Laing et al. (1999); Swain et al. (1998)). In this case we are not able to detect the fast spine at large viewing angles due to the relativistic beaming, but observe the more moderate outer layers and the orientation dependent unification of FR II radio galaxies and quasars can be still valid.

Good progress has been made during the past decade with regard to the orientation dependent unification of radio-loud objects in general. The basic picture seems correct, but the distinction between various classes appears somewhat diffuse. The actual torus, and jet set-up, connected to source power and lifetime evolution, is not yet understood. To better constrain and test unification scenarios, statistical approaches with large and complete samples are required, but detailed high resolution studies of sources like Cygnus A are important to verify that the proposed structures like the torus really exist.

BIBLIOGRAPHY

Alef, W. & Graham, D. A. 2002, in Proceedings of the 6th EVN Symposium, ed. E. Ros, R. W. Porcas, A. P. Lobanov, & J. A. Zensus (Bonn, Germany: MPifR), 31

Aller, H. D., Aller, M. F., Latimer, G. E., & Hughes, P. A. 2003, American Astronomical Society Meeting, 202, 18.01

Antonucci, R. 1993, ARA&A, 31, 473

Antonucci, R., Hurt, T., & Kinney, A. 1994, Nature, 371, 313

Antonucci, R. R. J., Hickson, P., Olszewski, E. W., & Miller, J. S. 1986, AJ, 92, 1

Antonucci, R. R. J. & Miller, J. S. 1985, ApJ, 297, 621

Baade, W. & Minkowski, R. 1954, ApJ, 119, 206

Bach, U. 2001, Master's thesis, Rheinische Friedrich-Wilhelms-Universität Bonn

Bach, U., Kadler, M., Krichbaum, T., et al. 2004, in Future Directions in High Resolution Astronomy: The 10th Anniversary of the VLBA, ed. J. Romney & M. Reid (ASP), in press, astro-ph/0309403

Bach, U., Krichbaum, T. P., Alef, W., Witzel, A., & Zensus, J. A. 2002, in Proceedings of the 6th EVN Symposium, ed. E. Ros, R. W. Porcas, A. P. Lobanov, & J. A. Zensus (Bonn, Germany: MPifR), 155

Bahcall, J. N., Kirhakos, S., Saxe, D. H., & Schneider, D. P. 1997, ApJ, 479, 642

Barthel, P. D. 1989, ApJ, 336, 606

Begelman, M. C., Blandford, R. D., & Rees, M. J. 1984, Reviews of Modern Physics, 56, 255

Bennett, C. L., Halpern, M., Hinshaw, G., et al. 2003, ApJS, 148, 1

Biretta, J. A., Moore, R. L., & Cohen, M. H. 1986, ApJ, 308, 93

Blandford, R. D. & Königl, A. 1979, ApJ, 232, 34

Blandford, R. D., Netzer, H., Woltjer, L., Courvoisier, T. J.-L., & Mayor, M. 1990, Active Galactic Nuclei (Springer-Verlag Berlin Heidelberg New York)

Blandford, R. D. & Payne, D. G. 1982, MNRAS, 199, 883

Bolton, J. & Stanley, G. 1948, Nature, 161, 312

Britzen, S., Roland, J., Laskar, J., et al. 2001, A&A, 374, 784

Britzen, S., Vermeulen, R. C., Taylor, G. B., et al. 1999, in ASP Conf. Ser. 159: BL Lac Phenomenon, ed. L. Takalo & A. Sillanpää (San Francisco, CA: ASP), 431

Burbidge, G. R., Jones, T. W., & Odell, S. L. 1974, ApJ, 193, 43

Camenzind, M. & Krockenberger, M. 1992, A&A, 255, 59

Carilli, C. L., Bartel, N., & Diamond, P. 1994, AJ, 108, 64

Carilli, C. L., Bartel, N., & Linfield, R. P. 1991, AJ, 102, 1691

Carilli, C. L. & Barthel, P. D. 1996, A&A Rev., 7, 1

Carilli, C. L., Dreher, J. W., Conner, S., & Perley, R. A. 1989, AJ, 98, 513

Carrara, E. A., Abraham, Z., Unwin, S. C., & Zensus, J. A. 1993, A&A, 279, 83

Cawthorne, T. V. & Wardle, J. F. C. 1988, ApJ, 332, 696

Cohen, M. H., Linfield, R. P., Moffet, A. T., et al. 1977, Nature, 268, 405

Conway, J. E. & Blanco, P. R. 1995, ApJ, 449, L131+

Conway, J. E. & Murphy, D. W. 1993, ApJ, 411, 89

Cotton, W. D., Feretti, L., Giovannini, G., Lara, L., & Venturi, T. 1999, ApJ, 519, 108

Eckart, A., Witzel, A., Biermann, P., et al. 1986, A&A, 168, 17

—. 1987, A&AS, 67, 121

Fanaroff, B. L. & Riley, J. M. 1974, MNRAS, 167, 31

Fey, A. L. & Charlot, P. 2000, ApJS, 128, 17

Fomalont, E. B. 1989, in ASP Conf. Ser. 6: Synthesis Imaging in Radio Astronomy, ed. R. A. Perley, F. R. Schwab, & A. H. Bridle (San Francisco, CA: ASP), 213

Fomalont, E. B. 1999, in ASP Conf. Ser. 180: Synthesis Imaging in Radio Astronomy II, ed. G. B. Taylor, C. L. Carilli, & R. A. Perley (San Francisco, CA: ASP), 463

Fosbury, R. A. E., Vernet, J., Villar-Martín, M., et al. 1999, in The Most Distant Radio Galaxies, ed. H. Rttgering, P. Best, & M. Lehnert, 311

Gabuzda, D. C., Kochenov, P. Y., Cawthorne, T. V., & Kollgaard, R. I. 2000a, MNRAS, 313, 627

Gabuzda, D. C., Kovalev, Y. Y., Krichbaum, T. P., et al. 1998, A&A, 333, 445

Gabuzda, D. C., Pushkarev, A. B., & Cawthorne, T. V. 2000b, MNRAS, 319, 1109

Ghisellini, G., Padovani, P., Celotti, A., & Maraschi, L. 1993, ApJ, 407, 65

Ginzburg, V. L. & Syrovatskii, S. I. 1965, ARA&A, 3, 297

Giovannini, G., Taylor, G. B., Arbizzani, E., et al. 1999, ApJ, 522, 101

Gomez, J. L., Marti, J. M. A., Marscher, A. P., Ibanez, J. M. A., & Alberdi, A. 1997, ApJ, 482, L33+

Högbom, J. A. 1974, A&AS, 15, 417

Hargrave, P. J. & Ryle, M. 1974, MNRAS, 166, 305

Heeschen, D. S., Krichbaum, T., Schalinski, C. J., & Witzel, A. 1987, AJ, 94, 1493

Hirabayashi, H., Hirosawa, H., Kobayashi, H., et al. 2000, PASJ, 52, 955

Hughes, P. A., Aller, H. D., & Aller, M. F. 1985, ApJ, 298, 301

Hughes, P. A., Miller, M. A., & Duncan, G. C. 2002, ApJ, 572, 713

Hummel, C. A. 1987, Master's thesis, Rheinische Friedrich-Wilhelms-

Universität Bonn

Hummel, C. A., Schalinski, C. J., Krichbaum, T. P., et al. 1992, A&A, 257, 489

Jackson, N., Tadhunter, C., & Sparks, W. B. 1998, MNRAS, 301, 131

Jannuzi, B. T., Yanny, B., & Impey, C. 1997, ApJ, 491, 146

Jorstad, S. G., Marscher, A. P., Mattox, J. R., et al. 2001, ApJS, 134, 181

Kadler, M., Kerp, J., & Krichbaum, T. P. 2004, A&A, n.n., n.n.

Kedziora-Chudczer, L., Jauncey, D. L., Wieringa, M. A., Tzioumis, A. K., & Bignall, H. E. 2001, Ap&SS, 278, 113

Kellermann, K. I., Lister, M. L., Homan, D. C., et al. 2004, ApJ, subm.

Kellermann, K. I. & Pauliny-Toth, I. I. K. 1968, ApJ, 152, 639

—. 1969, ApJ, 155, L71

Kellermann, K. I., Vermeulen, R. C., Zensus, J. A., & Cohen, M. H. 1998, AJ, 115, 1295

Kemball, A., Flatters, C., Gabuzda, D., et al. 2000, PASJ, 52, 1055

Klare, J. 2003, PhD thesis, Rheinische Friedrich-Wilhelms-Universität Bonn

Königl, A. 1981, ApJ, 243, 700

Kraus, A. 1997, PhD thesis, Rheinische Friedrich-Wilhelms-Universität Bonn

Kraus, A., Krichbaum, T. P., Wegner, R., et al. 2003, A&A, 401, 161

Krichbaum, T., Graham, D., Witzel, A., Zensus, J., & et al. 2004, in Exploring the Cosmic Frotier: Astrophysical Instruments for the 21st Century, 18 - 21 May 2004, Berlin, Germany, ESO Astrophysics Symposia (Springer-Verlag), in press

Krichbaum, T. P., Alef, W., Witzel, A., et al. 1998, A&A, 329, 873

Krichbaum, T. P., Graham, D. A., Witzel, A., et al. 2001, in ASP Conf. Ser. 250: Particles and Fields in Radio Galaxies Conference, ed. R. A. Laing & K. M. Blundell (San Francisco, CA: ASP), 184

Krichbaum, T. P., Kraus, A., Fuhrmann, L., Cimò, G., & Witzel, A. 2002, Publications of the Astronomical Society of Australia, 19, 14

Krichbaum, T. P., Witzel, A., Graham, D. A., et al. 1993, A&A, 275, 375

Lähteenmäki, A. & Valtaoja, E. 1999, ApJ, 521, 493

Lai, D. 2003, ApJ, 591, L119

Laing, R. A. & Bridle, A. H. 2002, MNRAS, 336, 328

Laing, R. A., Parma, P., de Ruiter, H. R., & Fanti, R. 1999, MNRAS, 306, 513

Liu, B. F., Mineshige, S., & Ohsuga, K. 2003, ApJ, 587, 571

Lobanov, A. P. 1998, A&A, 330, 79

Ma, C., Arias, E. F., Eubanks, T. M., et al. 1998, AJ, 116, 516

Marscher, A. P. 1979, ApJ, 228, 27

—. 1983, ApJ, 264, 296

Marscher, A. P. & Gear, W. K. 1985, ApJ, 298, 114

Meier, D. L. 2002, New Astronomy Review, 46, 247

Melia, F., Liu, S., & Fatuzzo, M. 2002, ApJ, 567, 811

Middelberg, E. 2004, PhD thesis, Rheinische Friedrich-Wilhelms-Universität Bonn

Middelberg, E., Roy, A. L., Walker, R. C., Falcke, H., & Krichbaum, T. P. 2002, in Proceedings of the 6th EVN Symposium, ed. E. Ros, R. W. Porcas, A. P. Lobanov, & J. A. Zensus (Bonn, Germany: MPifR), 61

Mushotzky, R. F., Done, C., & Pounds, K. A. 1993, ARA&A, 31, 717

Ogle, P. M., Cohen, M. H., Miller, J. S., et al. 1997, ApJ, 482, L37

Osterbrock, D. E. 1989, Astrophysics of gaseous nebulae and active galactic nuclei (Mill Valley, CA: University Science Books)

Pacholczyk, A. G. 1970, Radio astrophysics (San Francisco: Freeman), 97

Peacock, J. A. 1999, Cosmological physics (Cosmological physics. Publisher: Cambridge, UK: Cambridge University Press, 1999. ISBN: 0521422701)

Pearson, T. J. & Readhead, A. C. S. 1984, ARA&A, 22, 97

—. 1988, ApJ, 328, 114

Pearson, T. J. & Zensus, J. A. 1987, in Superluminal Radio Sources, ed. J. A. Zensus & T. J. Pearson (San Francisco, CA: ASP), 1

Pelletier, G. & Roland, J. 1989, A&A, 224, 24

Pen, U. 1999, ApJS, 120, 49

Peng, B., Kraus, A., Krichbaum, T. P., & Witzel, A. 2000, A&AS, 145, 1

Perley, R. A., Dreher, J. W., & Cowan, J. J. 1984, ApJ, 285, L35

Qian, S., Li, X., Wegner, R., Witzel, A., & Krichbaum, T. P. 1996, Chinese Astronomy and Astrophysics, 20, 15

Qian, S. J., Witzel, A., Kraus, A., Krichbaum, T. P., & Zensus, J. A. 2001, A&A, 367, 770

Quirrenbach, A., Witzel, A., Wagner, S., et al. 1991, ApJ, 372, L71

Raiteri, C. M., Villata, M., Tosti, G., et al. 2003, A&A, 402, 151

Readhead, A. C. S. 1994, ApJ, 426, 51

Rees, M. J. 1967, MNRAS, 135, 345

Reynolds, C. S. & Fabian, A. C. 1996, MNRAS, 278, 479

Rickett, B. J. 1990, ARA&A, 28, 561

—. 2001a, Ap&SS, 278, 129

—. 2001b, Ap&SS, 278, 5

Roland, J., Teyssier, R., & Roos, N. 1994, A&A, 290, 357

Ros, E., Kellermann, K. I., Lister, M. L., et al. 2002, in Proceedings of the 6th EVN Symposium, ed. E. Ros, R. W. Porcas, A. P. Lobanov, & J. A. Zensus (Bonn, Germany: MPifR), 105

Ros, E., Marcaide, J. M., Guirado, J. C., & Pérez-Torres, M. A. 2001, A&A, 376, 1090

Rybicki, G. B. & Lightman, A. P. 1979, Radiative processes in astrophysics (New York, Wiley-Interscience)

Ryle, M. & Hewish, A. 1960, MNRAS, 120, 220

Saikia, D. J., Salter, C. J., Neff, S. G., et al. 1987, MNRAS, 228, 203

Schalinski, C. J., Witzel, A., Krichbaum, T. P., et al. 1992, in Variability of Blazars, ed. E. Valtaoja & M. Valtonen (Cambridge: CUP), 225

Scheuer, P. A. G. & Readhead, A. C. S. 1979, Nature, 277, 182

Schmidt, M. 1963, Nature, 197, 1040

Shepherd, M. C. 1994, BAAS, 26, 987

Sol, H., Pelletier, G., & Asseo, E. 1989, MNRAS, 237, 411

Stern, D., Moran, E. C., Coil, A. L., et al. 2002, ApJ, 568, 71

Stirling, A. M., Cawthorne, T. V., Stevens, J. A., et al. 2003, MNRAS, 341, 405

Sudou, H., Taniguchi, Y., Ohyama, Y., et al. 2000, PASJ, 52, 989

Swain, M. R., Bridle, A. H., & Baum, S. A. 1998, ApJ, 507, L29

Tadhunter, C., Marconi, A., Axon, D., et al. 2003, MNRAS, 342, 861

Tadhunter, C. N., Packham, C., Axon, D. J., et al. 1999, ApJ, 512, L91

Thompson, A. R., Moran, J. M., & Swenson, G. W. 1986, Interferometry and synthesis in radio astronomy (New York, Wiley-Interscience)

Tian, W. W., Krichbaum, T. P., Witzel, A., et al. 2001, in IAU Symp. 205, Galaxies and their Constituents at the Highest Angular Resolutions, Manchester, ed. R. Schilizzi, S. Vogel, F. Paresce, & M. Elvis (San Francisco, CA: ASP), 96

Tingay, S. J., Preston, R. A., Lister, M. L., et al. 2001, ApJ, 549, L55

Turlo, Z., Forkert, T., Sieber, W., & Wilson, W. 1985, A&A, 142, 181

Ueno, S., Koyama, K., Nishida, M., Yamauchi, S., & Ward, M. J. 1994, ApJ, 431, 1

Ulrich, M., Maraschi, L., & Urry, C. M. 1997, ARA&A, 35, 445

Urry, C. M. 2004, in ASP Conf. Ser. :Princeton meeting on AGN Physics with the Sloan Digital Sky Survey, ed. G. T. Richards & P. B. Hall (San Francisco, CA: ASP), in press

Urry, C. M. & Padovani, P. 1995, PASP, 107, 803

van Bemmel, I. M. & Dullemond, C. P. 2003, A&A, 404, 1

van der Laan, H. & Perola, G. C. 1969, A&A, 3, 468

Vermeulen, R. C. & Cohen, M. H. 1994, ApJ, 430, 467

Wagner, S., Sanchez-Pons, F., Quirrenbach, A., & Witzel, A. 1990, A&A, 235, L1

Wagner, S. J. & Witzel, A. 1995, ARA&A, 33, 163

Wagner, S. J., Witzel, A., Heidt, J., et al. 1996, AJ, 111, 2187

Wagner, S. J., Witzel, A., Krichbaum, T. P., et al. 1993, A&A, 271, 344

Wehrle, A. E., Cohen, M. H., Unwin, S. C., et al. 1992, ApJ, 391, 589

Wilson, A. S. & Colbert, E. J. M. 1995, ApJ, 438, 62

Witzel, A., Heeschen, D. S., Schalinski, C., & Krichbaum, T. 1986, Mitteilungen der Astronomischen Gesellschaft Hamburg, 65, 239

Witzel, A., Schalinski, C. J., Johnston, K. J., et al. 1988, A&A, 206, 245

Young, A. J., Wilson, A. S., Terashima, Y., Arnaud, K. A., & Smith, D. A. 2002, ApJ, 564, 176

Zensus, J. A. 1997, ARA&A, 35, 607

Zensus, J. A., Ros, E., Kellermann, K. I., et al. 2002, AJ, 124, 662

Chapter 8

Acknowledgements

The last lines of this text should be words of gratitude to all those who contributed in various manners to this thesis and to whom I am indebted.

First of all, I have to thank the referees Prof. Dr. Ulrich Klein and Priv.-Doz. Dr. Walter Huchtmeier, who agreed to review the thesis and furthermore provided much advice, which led to the thesis in its the present form.

I would like to thank the directors of the Max-Planck-Institut für Radioastronomie who gave me the opportunity to address myself exclusively to my current research and the preparation of my thesis. Special thanks go to Dr. Anton Zensus for giving me the possibility to prepare this work in his VLBI group and and for his useful advice in planning this thesis and my future work.

I am greatly indebted to Dr. Arno Witzel and Dr. Thomas Krichbaum for the supervision of my thesis and the tireless help and numerous suggestions that made this work possible. I hope that we will continue this close and fruitful collaboration in the future.

Certainly, I have to thank all members of the VLBI group for the pleasant time in this institute and for the willingly share of their knowledge. Especially I appreciate Dr. Eduardo Ros and Dr. Alan Roy, for many useful discussions and for the careful review of numerous texts, Dr. Andrei Lobanov and Dr. Thomas Beckert, who provided me many insights in theoretical aspects that would have been hard to understand without them, Dr Alex Kraus for the prompt help on any question or problem concerning the Effelsberg telescope data and for reading my thesis, Dr Richard Porcas who always asked the "right" questions, and Dr. Walter Alef for the help on any hardware and software problem.

The time in the institute was exceptionally enjoyable also due to the many students in the VLBI group and to whom I am grateful too. Particularly I am thankful for the great time with my room mates, Matthias, Violetta, and Enno. Especially the nine years that Enno and I spent together at the university and in the institute will be nice to remember and I wish Enno all the best in Australia now.

Some of the observations used were provided by other researchers from inside

117

Lebenslauf

Uwe Bach
Lotharstr. 113
53115 Bonn

Geboren am 11. Juni 1975 in Köln

1981 – 1985	Peter-Petersen Grundschule Köln Höhenhaus
1985 – 1994	Abitur an der Gesamtschule Köln Holweide
1994 – 1995	Zivildienst bei der AWO in Köln
1995 – 2001	Studium der Physik und Astronomie an der Rheinischen Friedrich-Wilhelms-Universität Bonn
Mai 2000	Diplomand am Max-Planck-Institut für Radioastronomie in Bonn mit dem Thema: "Hochauflösende radiointerferometrische Beobachtung der Radio-Galaxie Cygnus A"
9. Mai 2001	Abschluss des Studiums mit dem Diplom in Physik
seit Juli 2001	Doktorand am Max-Planck-Institut für Radioastronomie in Bonn und in der International Max-Planck Research School for Radio and Infrared Astronomy der Universität Bonn